KINETIC AND SPECTROSCOPIC STUDY OF PEPTIDYLGLYCINE MONOOXYGENASE

A Dissertation

Submitted to the Faculty

of

Institute of Environmental Health

Oregon Health and Science University

by

Shefali Chauhan

In Partial Fulfillment of the

Requirements for the Degree

of

Doctor of Philosophy

June 2016

Oregon Health and Science University

ACKNOWLEDGEMENTS

I am very grateful to Dr Ninian J. Blackburn for being an ever supportive mentor. His immense knowledge and experience were instrumental during many phases of my research. It was both a pleasure and a privilege to have worked under his guidance.

My sincere thanks also go to Dr Pierre Moenne-Loccoz for always being willing to lend a helping hand with the instruments and experiments. This research is also indebted to him for many critical analyses and important feedbacks throughout its course.

Heartfelt thanks also go to my lab-mates for their cooperation and help. You boosted my morale numerous times and helped keep my life in balance.

Finally, I would like to thank my parents and my husband Amit, the greatest blessings of my life, for always being my support system. Mere words cannot express my feelings and gratitude.

TABLE OF CONTENTS

Page

LIST OF TABLES

Table Page

LIST OF FIGURES

ABSTRACT

This dissertation aims to shed light on some of the key questions and lesser known aspects of the mechanism of peptidylglycine alpha-hydroxylating monooxygenase (PHM). PHM, a dicopper containing enzyme, comes under the category of the type II family of monooxygenases and participates in activation of the peptides and neuro hormones by amidating their C-terminus. PHM catalyzes the first of the two-step amidating reaction by production of a hydroxylated intermediate, which undergoes dismutation to yield an amidated product.

Structurally PHM is made up of two domains, each of which houses a copper center, separated by 11Å solvent-filled cleft. The copper centers, CuH and CuM, serve different and distinct functions in the course of the catalytic cycle. The CuM-site serves as the oxygen binding and catalytic center whereas; the CuH-site serves as electron storing and transferring site. Chapter 3 in the thesis is a study of characterization of PHM mutants which possess only one of the copper sites. The H242A mutant (CuH-site only) and H107AH108A (CuM-site only) were produced, purified and reconstituted in the lab and used for studying the copper sites individually in order to analyze their roles in detail. The EXAFS and EPR studies on the Cu(II) forms of the copper sites were consistent with the previously determined ligand set of Cu(II)His_3O and Cu(II)His_2O_2 for

CuH-site and CuM-site respectively. The Cu(I) form of the copper sites unearthed interesting changes. While the H107AH108A (CuM-site only) mutant corroborated with the previously reported results of coordinating two histidines and a methionine at all pHs, the CuH-site was two coordinate at neutral pH and on lowering the pH was able to coordinate to a methionine S ligand and become three coordinate. FTIR studies on the single-site mutants were able to confirm that the 2092 cm^{-1} could be assigned with confidence to the CuM-CO adduct. Hetero-bimetallic PHM was also created using silver and copper. It was established by EXAFS studies on the H107AH108A and M109I mutant that the silver bound only to the M-site, allowing a new opportunity to study the CuH-site without disruption of the CuM site.

Chapter 4 deals with the interesting aspect of the long distance electron transfer (ET) from CuH-site to CuM-site and the key players which facilitate this process. Two electrons are transferred in the course of the catalytic cycle. The formation of the CuM-superoxo intermediate is preceded by transfer of the first electron (reductive phase) whereas the second electron transfer follows the formation of the CuM-OOH intermediate (catalytic phase). Kinetic studies using stopped-flow and a novel chromophoric agent, N,N-dimethyl amino-p-phenylenediamine. (DMPD), were employed on the WT PHM and its various mutants (H107A, H108A and H172A). H108 was found to play a vital role in the reductive phase electron transfer pathway. The results strongly indicate that the reductive phase and catalytic phase ET pathways are different and suggest a bifurcated ET pathway in PHM. It is proposed that the reductive phase ET is made up of H108, water molecule and substrate while the H172 and Y79 form the catalytic phase ET pathway.

The final chapter of the thesis consists of the various preliminary studies done in a bid to trap the CuM-oxygen intermediate. Stopped-flow studies were performed with the WT PHM at 4^{o} C in the presence of high concentrations of oxygen. Azide, a structural analog of oxygen, was used as the reporter agent. Different experimental conditions were tested, including use of the mechanism based inhibitor of PHM, 4-phenyl-3-butanoic acid (PBA). An absorbing species at 350 nm was consistently detected. Various control reactions performed pointed to the absorbing species being a PHM oxygen adduct. Previous studies on copper-oxygen model complexes support the notion that the absorbing species at 350 nm could be a CuM-peroxo complex. However, further studies are required in order to study and characterize the PHM-oxygen complex.

CHAPTER 1. INTRODUCTION

Biologically active peptides rival hormones for their role as signaling agents in the body, and as neurotransmitters to nearby cells [1]. Many bioactive peptides are synthesized from their inactive precursor forms by a set of posttranslational modifications. Among the many types of posttranslational modifications, amidation is considered to be the most important [2]. The amidation reaction is catalyzed by peptidylglycine α-amidating monooxygenase (PAM; EC 1.14.17.3), a bifunctional enzyme. The following section describes in detail, the importance of amidation, and the early discoveries which helped in characterizing PAM's vital role.

1.1 Discovery of PAM and Early Findings

As already mentioned, amidation is an important post translational modification required by many proteins to attain full biological activity [1][2][3][4]. Amidated peptides regulate growth, appetite, digestion, bone mass, blood volume, stress response, pain, circadian rhythms and many other endocrine functions [5][6][7][8][9][10]. Although they were discovered in the early fifties [11], their significance was only unearthed two decades later [12]. It has been speculated that the key role of amidation is to prevent ionization of the COOH terminus of the peptide, rendering the peptide hydrophobic, which in turn results in tighter binding of the peptide to its receptor [13]. Amidation also increases the half-life of the peptides by making them resistant to ubiquitination [14]. The process of amidation takes place in the presence of copper [15], oxygen and a strong reductant, which is usually ascorbate [16]. Once the importance of this post translational modification was established, amidating enzymes were purified from many sources such as bovine neurointermediate pituitary, frog skin, rat medullary thyroid carcinoma and brain [17][18][19][20][21]. The properties of the purified enzyme, catalyzing amidation, resembled that of a monooxygenase, this led to categorization of the amidating enzyme as petidylglycine α-amidating monooxygenase (PAM) (EC 1.14.17.3) [17]. PAM was capable of amidating peptides possessing neutral amino acids at the C-terminus, but it acted preferentially on peptides which had either glycine or alanine at the C-terminus [22][23][24]. It was discovered by Merkler et al. that the ratio of the product (amidated peptide) and the ascorbate consumed was 1:1 [25]. The amide moiety was found to be derived from the terminal glycine of the peptide [12].

Amidation was indicated to be a two-step process when a reactionary intermediate was trapped by Bradbury et al [26]. The reaction took place in two steps. The first step, which is stereospecific in nature [27], leads to the formation of a hydroxylated intermediate. This occurs due to the addition of the hydroxyl group on the α-carbon of the COOH of the terminal glycine [28], with the oxygen in hydroxylated group derived from O_2 [25]. This hydroxylated intermediate undergoes dealkylation to yield an α-amidated peptide and glyoxalate as a byproduct [29], as seen in Figure 1-1

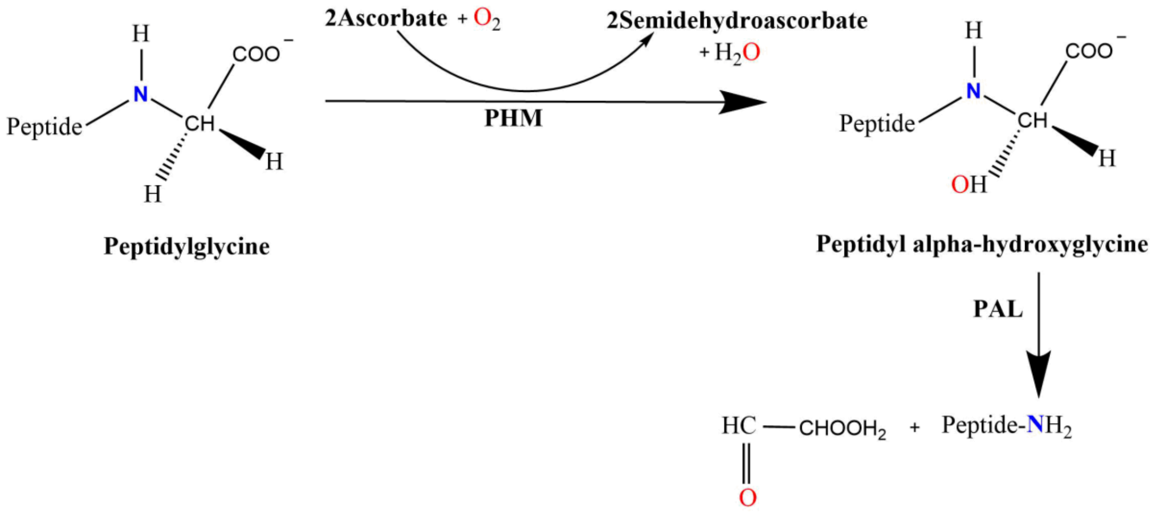

Figure 1-1 *Schematic representation of the mechanism of amidation.*

Initially the hydroxylated intermediate was thought to be short-lived but subsequent experiments were successful in trapping this intermediate, dispelling its transient status [29][30].

In 1990, a hydroxy glycine amidating alkylase (HGAD) was isolated by Katapodis et al., which was capable of catalyzing the conversion of α-hydroxybenzoylglycine to benzamide [20]. When HGAD and PAM were purified separately, each fraction exhibited low amidation activity. However, combining these two protein fractions led to the restoration of full PAM activity. This result, along with the presence of a stable hydroxyglycine intermediate, indicated participation of a second protein factor in the enzymatic pathway.

Eipper et al. were able to demonstrate the conversion of α-N-acetyl-Tyr-Val-Gly to its amidated form by addition of a protein factor present in the secretory granules of the anterior pituitary of rat. They called this factor stimulator of PAM or SPAM [31]. A strong correlation between the high PAM activity and high levels of SPAM was observed [32]. The SPAM enzyme is now referred to as PAL (Peptidyl Amidating Lyase). It was proposed that the monooxygenase domain and the dealkylating domain were produced in form of a single enzyme which underwent tissue specific endoproteolytic cleavage to form two separate soluble enzymes [20]. This theory was further supported by the observation that the dealkylating enzyme was able to amidate a hydroxylated peptide, produced by the moonooxygenase enzyme [20][30]. The first enzyme was named peptidylglycine α-hydroxylating monooxygenase (PHM) after the substrate hydroxylation reaction catalyzed by it, while the second enzyme is named peptidylhydroxyglycine α-amidating lyase (PAL) due to its ability to cleave the N-C peptide bond.

In bovine neurointermediate pituitary, these enzymes are generated by the endoproteolytic cleavage of a 108 kDa precursor [33]. The bifunctional enzyme is also found as a single, 75 kDa protein in rat medullary thyroid carcinoma and adult rat atrium cells, suggesting that the need for one enzyme with two functions or two separate enzymes may be tissue specific [34][25]. Additionally, no bifunctional PAM enzyme has been identified in D. *melanogaster* or in sea anemone, although separate genes encoding PHM and PAL have been found [35][36]. This suggested that the two proteins were originally separate enzymes which became joint entities with evolution. The next two sections describe the function and structure of PAL and PHM, respectively.

1.1.1 PAL

1.1.1.1 Reaction Mechanism

Amidation of the hydroxylated intermediate occurs via the N-C bond cleavage of the terminal glycine residue by the PAL (EC 4.3.2.5). The optimum pH for PAL with substrate α-acetyl-tyr-val-gly α hydroxyglycine was around 5, and the K_m about 38 μM [37].The activity of PAL was inhibited by the metal chelator EDTA, suggesting involvement of a metal [29][37][[39]. Reconstituting the apo protein with zinc metal restored some of its activity, which indicated that PAL is a zinc dependent metalloenzyme [40].

It is now known that zinc binds in the active site of PAL by three histidines (H585, H690 and H786) and an acetate ion bound as a monodentate ligand [40][41]. Since its removal causes total elimination of the lyase activity of PAL, it was proposed that Zn(II) might play a catalytic role or a structural role in PAL activity. However, since addition of zinc is only able to restore some of the activity, it might play an important structural role as well [40].

1.1.1.2 PAL Structure

The crystal structure of the catalytic core of PAL folds as a six-bladed β propeller. The blades are positioned around a central cavity. Each blade consists of four antiparallel β-strands, with the first strand at the center of the propeller and the last at the edge (Figure 1-2 a). The “cup” of the β propeller encompasses the active site and is made by the loops connecting strands 4 of one blade to strand 1 of the next blade and loops connecting strands 2 and 3 of each blade.

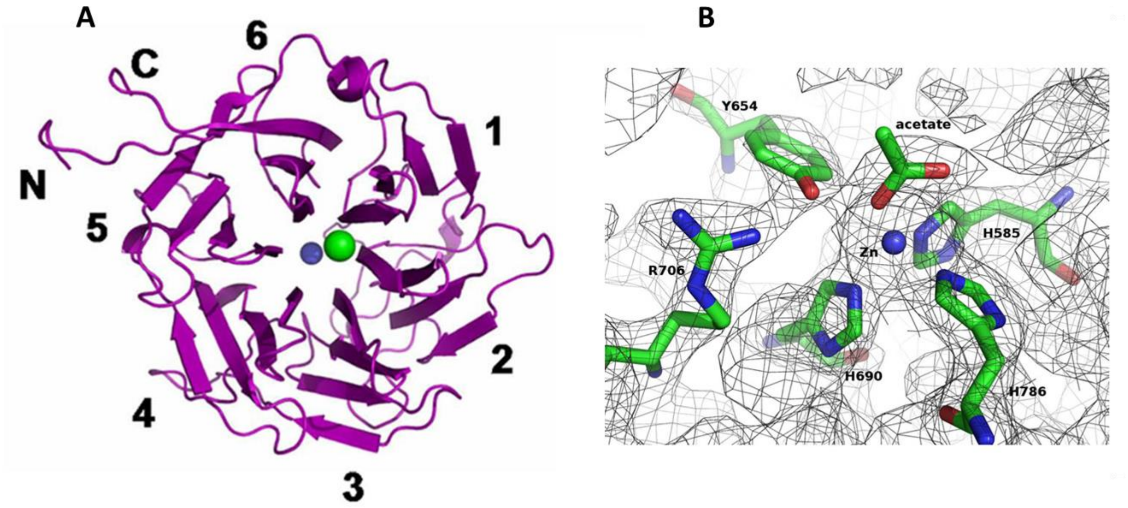

Figure 1-2 *Crystal structure of PALcc. Reprinted with permission from Chufán et al. (Structure, 2009, 17(7)). Copyright (2009) Elsevier Ltd. PDB identifier: 3FVZ, resolution: 2.35 Å.*
A) The PAL enzyme folds as a six-bladed propeller. The Zn(II) and the Ca(II) ions are indicated as blue, and green balls, respectively.
B) The zinc(II) ion is in close proximity to the essential tyrosine, Y654, and a key arginine, R706, and is coordinated in a very distorted tetrahedral polyhedron liganded by three histidines and one acetate bound in a monodentate fashion. The gray mesh represents the $2F_o$-F_c *electron density contoured at 1σ.*

The first blade provides a tryptophan (Trp538) that not only creates a hydrophobic pocket for the substrate, but may also provide the surface for interaction with the PHM domain. The central cavity houses a calcium ion required for structural integrity and a zinc ion for catalytic activity. The PAL substrate binds close to the zinc, which is coordinated by three histidines, a conserved tyrosine (Tyr654) and arginine (Arg706) (Figure 1-2 b). The disulfide linkages play an important role in the structural integrity of PAL. The N- and the C-termini are positioned close to each other with the C-terminus tethered to the membrane.

1.1.2 PHM

1.1.2.1 Reaction Mechanism

The first step of amidation begins with the hydroxylation of the α-carbon of the C-terminal glycine. The enzyme catalyzing this step is PHM (EC 1.4.17.3), containing two coppers as cofactors. The hydroxyl group was found to be derived from molecular oxygen by a study which involved isotopic labelling of the molecular oxygen by ^{18}O [42][38][43]. The catalytic cycle starts with the binding of the two molecules of ascorbate, which reduces the copper centers to the cuprous state and releases two molecules of semidehydroascorbate as a byproduct [38]. This is followed by the equilibrium ordered binding of the peptidylglycine substrate and oxygen [44]. Eventually, a $CuO_2^{\cdot-}$(copper-superoxo intermediate) is proposed to be formed [57][46][47][48]. This superoxo intermediate is speculated to be responsible for abstraction of the H-atom by a hydrogen tunneling mechanism from the α-C position on the peptidylglycine substrate, forming a copper-peroxo intermediate (Cu-O-OH) and a substrate radical [49][50]. Hydroxylation is believed to be accomplished by peroxide O-O bond cleavage and radical rebound to the substrate radical, which also includes the transfer of a second electron from one of the copper center to the other [49][50]. The rate limiting step for the PHM-catalyzed hydroxylation of the peptide precursors was found to be the cleavage of the αC-H bond by kinetic isotopic studies [51].

The enzyme bound copper plays a central role in the PHM chemistry. It is not only responsible for activation of oxygen but also for the formation of the hydroxylated intermediate [39]. The enzyme works at its maximum activity only when both the coppers are bound to the enzyme [52]. PHM shares 30% homology as well as an identical active site structure with dopamineβ-monooxygenase (DβM) [53][54][55]. Both the enzymes possess type 2 copper centers which undergo redox cycling during the course of one catalytic cycle, with the concomitant production of product [56][38][57]. Binding studies with carbon monoxide CO, an O_2 analog, showed that the CO bound only to one of the copper of the two, providing evidence that the two coppers were inequivalent [55]. Based on the results by various studies, an activity model was developed for DβM in which the two inequivalent centers served different functions. One of the copper centers, termed CuM, was involved in the oxygen binding and catalysis, while the second, CuH, was associated with electron transfer. This model was also found to be true for PHM [58][59].

1.1.2.2 PHM Structure

Structurally, the WT PHM is a prolate ellipsoid (55 Å by 45 Å by 25 Å) and is composed of two nine-stranded β-sandwich domains. Each domain is 150 residues in length and binds a copper atom [35](Figure 1-3). The two domains possess similar topologies with each domain composed of a common eight-stranded anti parallel motif. The interior of the domains is composed of hydrophobic residues and lacks any charged residues. The two domains are closely associated through a hydrophobic surface interface that buries $500\ \text{Å}^2$ of surface area from each domain. The rest of the interface consists of an inter-domain space (~10 Å), fully accessible to solvent.

Figure 1-3 *A representation of the PHMcc fold. Adapted with permission from Prigge et al. (Science, 1997, 278 (5341)). Copyright (1997) The American Association for the Advancement of Science. PDB identifier:1PHM, resolution: 1.90 Å.*
The backbone is shown in grey with the copper atoms in green spheres. The strands are numbered arrows and the cylinder is a 3_{10} helix. The side chains of the ligands to the two copper atoms are colored by atom type (carbon is gray, nitrogen is blue and sulfur is yellow)

Domain I is a β sandwich, composed of two anti-parallel sheets, one containing four strands and the other containing five strands. The three disulfide bridges (shown in yellow in Figure 1-3) help in anchoring the loops to the domain without linking the two β sheets together. Domain I binds one copper, CuH, at its active site. The CuH is ligated to three histidines (H107, H108 and H172). H107 and H108 are located at the beginning of the strand 5, whereas the H172 is at the end of strand 9 [55]. The geometry of the CuH site can be described as square pyramidal [63].

Domain II consists of one four-stranded antiparallel β sheet and one five-stranded mixed β sheet. The two disulfide bridges connect strands from one sheet to the strands of another sheet. The domain II also contains two small anti-parallel strands (14, 18 and 12, 20) and binds the second catalytic copper, CuM, which is ligated to two histidines (H242& H244) and a methionine (M314) (Figure 1-4). The histidines are found at the end of strand 14 while the methionine is found at the beginning of strand 21. The coordination of the CuM site is tetrahedral [61]. All of the six copper ligands are conserved among PHM and the DβM sequences and mutagenesis of any of the ligands leads to loss of the activity of PHM [62][63][64]. The copper centers are 11 Å apart from each other.

It is important to note that although the CuH is the electron transfer site and CuM is the oxygen binding site [62][55], structurally the CuH site resembles the oxygen binding site and the CuM site is most similar to the electron transfer site of other copper containing proteins [65]. These distinctive features highlight the unusual case of PHM. EXAFS data have shown large changes in coordination on reduction of the copper centers. The CuH changes from 4 or 5-coordination site of tetragonal geometry to a 2-coordinate one, with one of the histidines becoming undetectable by EXAFS. The CuM changes from a 4 or 5-coordinate trigonal site to a trigonal or tetrahedral one with an estimated ~0.4 Å movement of the M314 ligand [66][67][68].

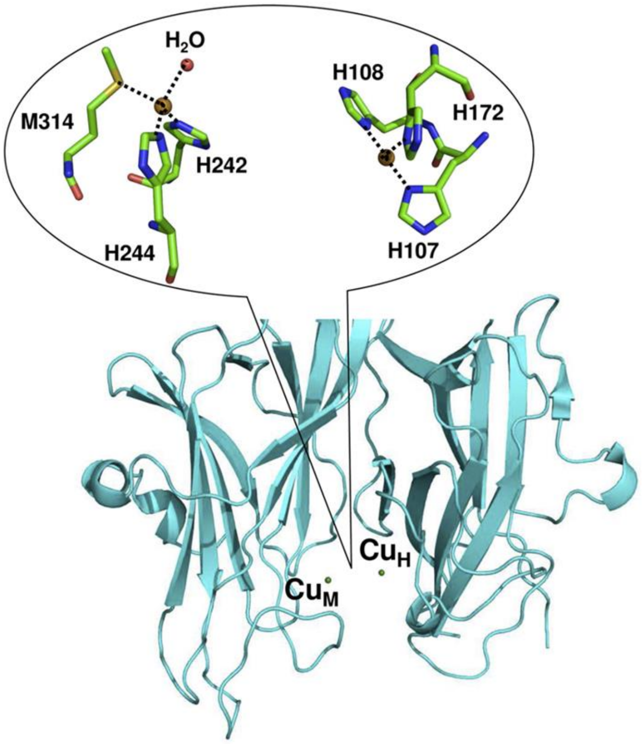

Figure 1-4 *Structure of CuM and CuH sites of PHMcc. Reprinted with permission from Chufán et al. (J. Am. Chem. Soc, 2010, 132(44)). Copyright (2010) American Chemical Society. PDB identifier:1PHM, resolution:1.90 Å.*

An important aspect of the PHM structural chemistry was determining how the substrate bound near the CuM-site. Amzel et al. reported the three-dimensional structure of oxidized PHM catalytic core with the substrate N-α-acetyl-3,5-diiodotyrosine (K_m = 3 µM) [35]. Several conserved active site residues (R240, Y318, and N316) and one water molecule form hydrogen bonds with the peptide backbone of the bound substrate, anchoring it in the inter-domain cleft (Figure 1-5). It was found that the binding of the substrate did not perturb the geometry or decrease the distance between the copper sites. However, N316 rotates ($\Delta_{\chi 2} \approx 30^0$) and forms a new hydrogen bond with the peptide backbone after breaking a hydrogen bond with Y318 [35].

The binding-site is tailored to bind the peptide substrates. Several conserved amino acids of the active site, R240, Y318, N316 and a water molecule form hydrogen bonds with the backbone of the peptide substrate and anchor it in the inter-domain cleft (Figure 1-5) [35]. Besides these, several other residues, including M314 [55], were found to have extensive contact with the substrate.

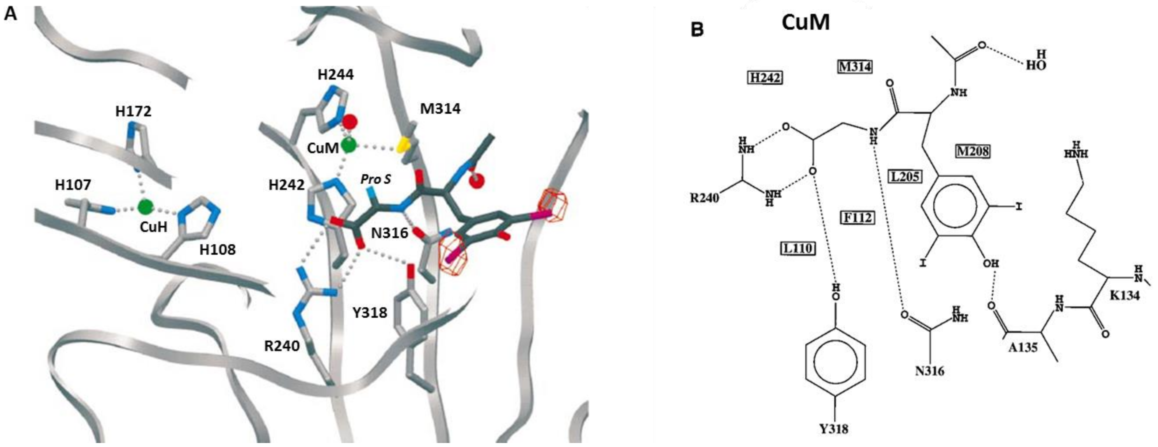

Figure 1-5 *PHMcc-substrate complex. Adapted with permission from Prigge et al. (Science, 1997, 278 (5341)). Copyright (1997) The American Association for the Advancement of Science. PDB:1PHM, resolution:1.90 Å.*
(A) Representation of N-α-acetyl-3,5-diiodotyrosylglycine bound in PHMcc active site. PHMcc backbone is shown in grey, the coppers represented by green spheres, and other atoms colored by atom type. The electron density of a difference map contoured at 7σ is shown as red mesh, indicating the positions of the electron-dense iodine atoms.
(B) Contact map depicting residues that interact with bound peptide. The H-bond interactions are indicated by dotted lines.

1.1.2.3 Pre-Catalytic Enzyme Complex

The study of the pre-catalytic complex was undertaken to shed light on the mechanism of hydroxylation. This required determining the structure of PHM in presence of substrate, ascorbate and molecular oxygen. This complex was stabilized by using N-acetyl-diiodo-tyrosyl-D-threonine (IYT) as a substrate. Calculations indicated that due to lower stability of the slow substrate radical, the hydrogen abstraction step is considerably slowed down, making it possible to trap the pre-catalytic enzyme complex [69].

As seen in Figure 1-6 and Figure 1-7 the O_2 molecule binds to the CuM with an end-on η^1 geometry in the pre-catalytic complex. The Cu-O-O bond angle is 110^o and the O-O distance was refined to a value of 1.23 Å (Figure 1-7). The hydrogen abstraction has been proposed to take place once the pre catalytic complex has formed. The structure suggests that the thermal rotation of the bound O_2 by about 110^0 could place it in proximity of the glycine pro-S hydrogen. This would facilitate both the electron transfer and hydrogen abstraction step.

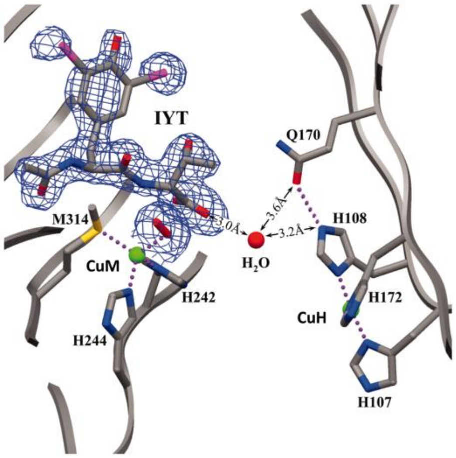

Figure 1-6 *The pre-catalytic complex of PHM with bound peptide and dioxygen. Adapted with permission from Prigge et al. (Science, 2004, 304 (5672)). Copyright (2004) The American Association for the Advancement of Science. PDB identifier:1SDW, resolution:1.85 Å.*
The 2F_0-F_c electron density (contoured at 1.5σ) is shown for dioxygen and the IYT peptide. Substrate and protein atoms are colored by atom type. The water molecule is represented by a red sphere and molecular oxygen by a red rod. Dotted lines indicate hydrogen bonds and bonds to the copper atoms (green).

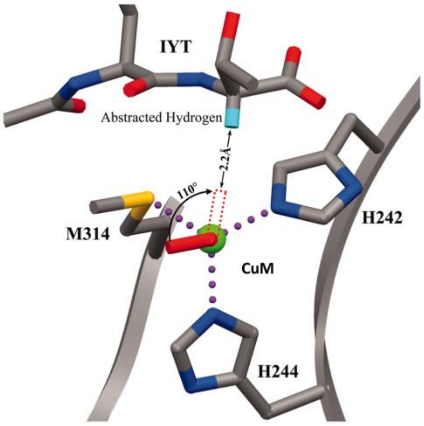

Figure 1-7 *A structure-based model of substrate dioxygen interaction. Adapted with permission from Prigge et al. (Science, 2004, 304 (5672)). Copyright (2004) The American Association for the Advancement of Science. PDB identifier:1SDW, resolution:1.85 Å.*
The molecular oxygen is represented by a red rod. Dotted lines indicate hydrogen bonds and bonds to the copper atoms (green).

Two of the most important, but least understood, aspects of PHM chemistry are the nature of the copper-oxygen intermediate and the long-distance electron transfer (ET) from CuH to the CuM-site. The next section provides a background and summary of developments in the field of copper-oxygen complexes.

1.1.1 Copper-Oxygen Complexes

The study of the copper complexes with activated oxygen is an important field not only for biological reactions catalyzed by copper enzymes, but also for reactions in synthetic chemistry and catalytic oxidation chemistry. Two basic copper sites activate oxygen for insertion into the substrate: mononuclear and dinuclear [70] and four principal binding modes are established for the interaction of copper complexes with dioxygen [71]. The mononuclear Cu(I) complex with oxygen forms adducts such as superoxide and peroxide which are either η^1/end-on or η^2/side-on complex as seen in Figure 1-8.

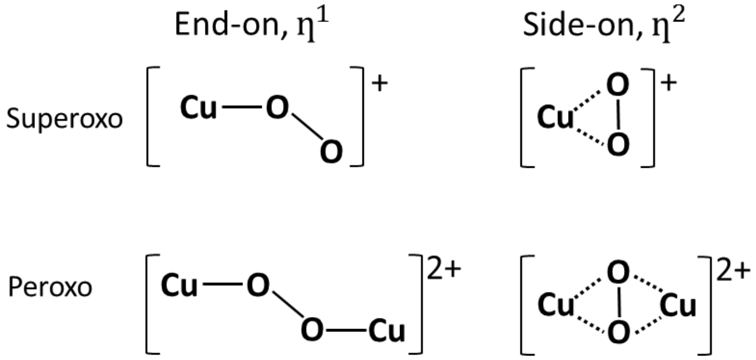

Figure 1-8 *Copper superoxo and peroxo complexes.*

The dinuclear copper oxygen complexes bind the oxygen between the two copper atoms. This has the benefit of avoiding formation of the free superoxide radical. The binding is either end-on/μ-1, 2 peroxo dicopper (II) complex or side-on/μ-$\eta^2:\eta^2$ peroxo dicopper(II) complex [72].

Figure 1-9 shows the possible reaction pathways for generating the series of the copper-active complexes. The S and P in CuS and CuP stand for the superoxo and peroxo complex. The superscripts in CuS^E and CuS^S stand for oxygen bound in an end-on and side-on fashions, respectively. In many cases the mononuclear copper-dioxygen adducts are easily trapped by the another copper(I) molecule, giving rise to μ-peroxide dicopper(II) complexes [72][73]. The μ-peroxide dicopper(II) complex can be further converted to a bis (μ-oxido) dicopper(III) complex, Cu_2O_2. However, this is possible only when the supporting ligands can stabilize the higher oxidation state, Cu(III), of copper. In this particular case, two electrons are injected into the peroxide moiety from each copper (II) ion to induce homolysis of the O-O bond [72]. The Cu_2O_2, supported by a less sterically hindered bidentate ligand, is able to further react with a Cu(I) to give a mixed-valent trinuclear copper (II, II, III) complex, Cu_3O_2 [72].

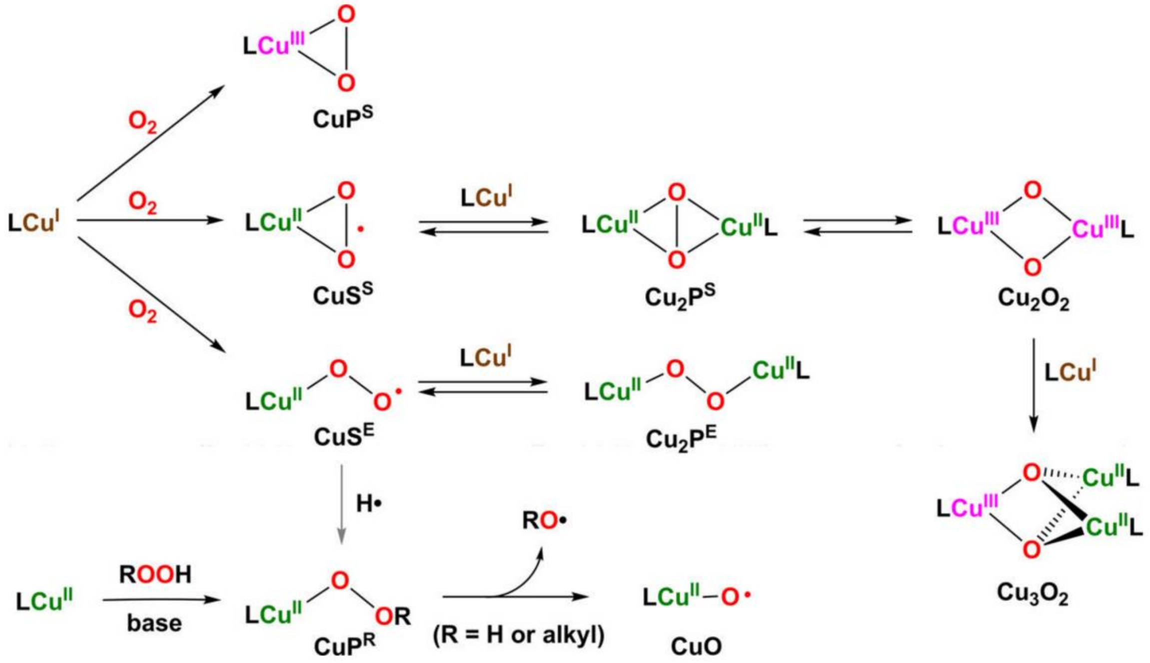

Figure 1-9 *The possible pathways for generation of copper-active oxygen complexes. Reprinted with permission from Itoh. S (Accounts of Chemical Research, 2015, 48(7)). Copyright (2015) American Chemical Society.*

1.1.1.1 L8-CuS^E Complexes

Mononuclear copper (II) superoxide complexes are the key reaction intermediates in monooxygenases enzymes such as dopamine β-monooxygenases (DβM), tyramine β-monooxygenases (TβM), peptidylglycine α-hydroxylating monooxygenase(PHM) [72][74][75] and recently in the polysaccharide monooxygenases [76]. The copper (II) superoxide intermediates wield enough energy to cleave an aliphatic C-H bond, eventually leading to hydroxylation [49][50]. Despite the importance of these reactionary intermediates, very little is known about their physiochemical properties and reactivity. Hence the study of mononuclear Cu(II)-superoxide model complexes has received much attention. The Cu(II)-superoxide complex is stabilized by supporting ligands having bulky or electron donating substituents which prevent dimerization reactions [73][77][78]. Kitajima et al. succeeded in obtaining the first crystals of a side-on Cu(II)-superoxide complex (CuS^S) by using a tridentate ligand Tp (hydrotrispyrazolylborate), which has a bulky alkyl substituent like tert-butyl or adamantyl [79][80]. Tolman et al. reported formation of copper-peroxide (CuP^S) of a copper-dioxygen adduct, in a side-on fashion, prepared by a β-diketiminate bidentate ligand (Dk) [81][82]. This was followed by Schindler et al. reporting the first crystal structure of an end-on superoxide-copper(II) complex (CuS^E), generated by using a tripodal tetradentate and strong electron donating substituent, tetramethylguanidine $(TMG)_3$tren [83]. After Schindler et al. managed to generate the first CuS^E complex, many such compounds were reported [84][85][86][87]. However, the CuS^E model complexes were penta-coordinate and possessed either trigonal bipyrimidal or a square planar geometry, whereas the ones found in enzymatic systems were distorted tetrahedral four-coordinate structures [76].

Itoh et al. were the first to develop a mononuclear copper (II) complex which closely resembled the proposed reactive intermediate of copper monooxygenases. This was achieved by using a simple tridentate ligand, 1,5 diazacycyclooctane (a rigid eight-membered cyclic diamine), with a 2-(pyridyn-2-yl)ethyl donor group ($L8^R$) [88] (Figure 1-10). Since the $L8^R$ does not have either bulky side groups or electron donating groups, the stabilizing mechanism of $L8^RCuS^E$ is different from the earlier CuS^E complexes. The $L8^RCuS^E$ complex exhibited an LMCT around 400 nm with a broad absorption in the visible-to-near IR region [89]. Resonance Raman studies determined the O-O and Cu-O stretching frequencies to be 969 cm^{-1} and 442 cm^{-1} [90]. EPR studies using parallel excitation mode have pointed towards a spin triplet ground state [91].

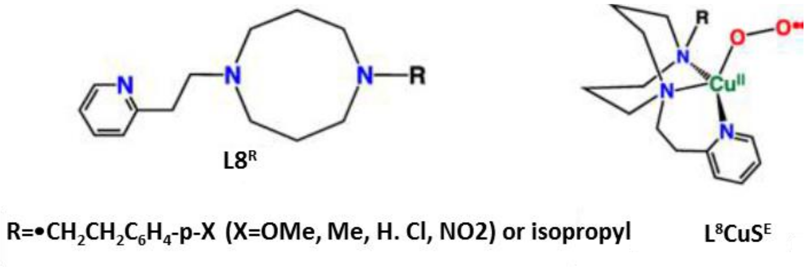

Figure 1-10 *Ligand L8^R and copper (II)-superoxide complex (L8^R) CuS^E. Reprinted with permission from Itoh. S (Accounts of Chemical Research, 2015, 48(7)). Copyright (2015) American Chemical Society.*

A notable feature of this complex is that it is capable of hydroxylating aliphatic compounds, making it a unique example of a functional model complex. Efforts to generate a biologically relevant copper-active oxygen complex by using N_2S donor set by using L8^R proved to be futile [77].

1.1.1.2 Biologically Active Cu(II)-Superoxide Model Complex DMA(N_3S)Cu(II)O_2^-

The thioether bond plays a very important role in the catalytic site of PHM. Mutation of the M314 residue leads to inactivation of PHM [62][63]. This ligand is also thought to play a critical role in the function of the CuM superoxide intermediate which leads to the C-H bond activation [46]. Although many model complexes, possessing a thioether donor, have been generated, all of them formed end-on dicopper (II) peroxo complexes instead of a superoxide complexes [92][93][94]. Kim et al. were able to report the first mononuclear end-on copper-superoxide complex which had the N_3S ligand set as well as enhanced activity towards O-H and C-H bonds [95]. The new ligand N_3S differs from previously reported ligands in having a highly electron rich dimethylamino (DMA) group [96] at the para positon of two pyridyl donors, which stabilizes the complex, and a bulky moiety (o-methyl benzyl) to prevent dimerization (Figure 1-11). The superoxide with the DMA (N_3S) ligand was found to exhibit enhanced activity towards O-H and C-H bonds compared to the corresponding complexes possessing N_4 ligand set [95]. This result strongly supports the idea that the role of the methionine ligand in PHM and DβM is to activate the superoxide species by increasing its electrophilicity by being a weak donor in comparison to the N_4 set. The copper oxygen intermediate in PHM and DβM has eluded detection so far.

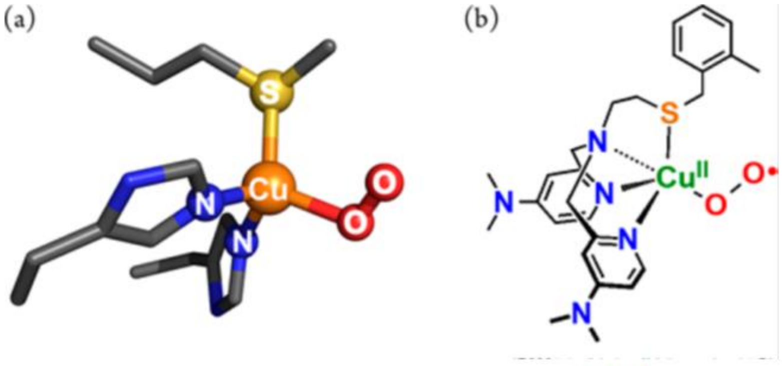

O_2-Adduct of Cu_M in PHM

($^{DMA}N_3S$)Cu^{II}($O_2^{\bullet-}$) (2^S)

Figure 1-11 *Synthetic copper oxygen complexes. Reprinted with permission from Kim et al. (J. Am. Chem. Soc., 2015, 137(8)). Copyright (2015) American Chemical Society. (a) The oxygen adduct of CuM in PHM (b) Ligand (DMAN$_3$S)CuII(O$_2^{\cdot -}$)(2S)*

1.1.2 Electron Transfer

Long range electron transfer (ET) is an important component of many processes that are essential for biological functions; such is the case for PHM chemistry as well. The following section aims to cover a brief summary of early ET theories in general and outlines the challenges in solving the ET pathway in PHM.

1.1.3 Electron Transfer Theories

The earliest theory proposed to understand the ET in proteins was put forward by Szent Gyorgyi in 1941 [97]. Popular models included electron “packets” travelling through the semiconductive medium of the protein [97], as well as the dynamical models which proposed that conformational changes bring the electron donors and acceptors in close contact for the reaction to occur [98]. The dynamical models also predicted that the ET rates would slow down dramatically at lower temperatures. However, it was found, in the case of cytochrome from *Chromatium vinosum*, that the rates of ET were the same at 100 K as well as 4.5 K [99][100]. This led Hopfield et al in 1974 to propose that electrons tunneled through protein medium [101][102]. In order to understand the factors that account for an efficient ET, the Franck-Condon principle and Marcus theory are described in the next section.

1.1.3.1 Franck-Condon Principle and Marcus Theory

The Franck-Condon principle states that because the electrons move much faster than the nuclei, the nuclei remain fixed during the actual reaction. Therefore, the transition state of the reaction must be in a nuclear-configuration space where the reactants and product states are degenerate.

According to the Marcus theory, it is possible to represent the energy changes in an electron transfer event ($\boldsymbol{R^{-1}} + \boldsymbol{P} \overset{\boldsymbol{e^-}}{\Leftrightarrow} \boldsymbol{R} + \boldsymbol{P^{-1}}$) by the graph shown in Figure 1-12. The parabolas represent the potential energy surfaces of the reactant and product as the nuclei move around.

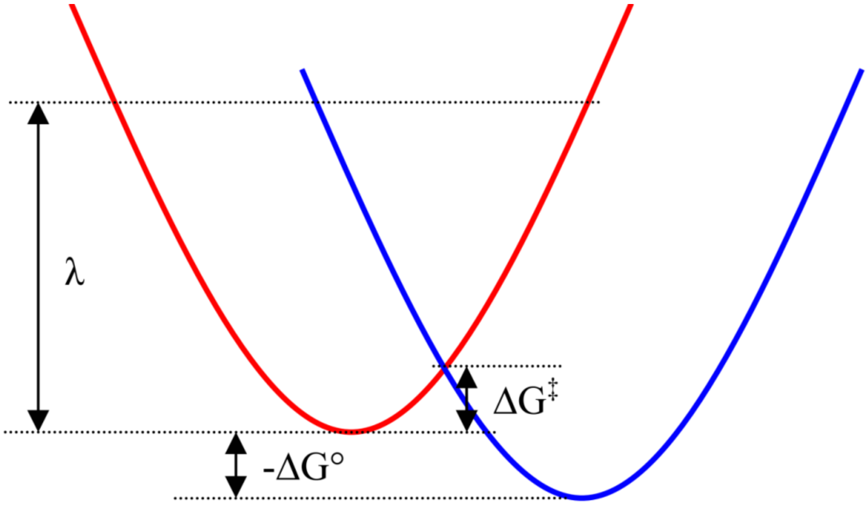

Figure 1-12 *The parabolas of outer-sphere reorganization energy of the system of two spheres in a solvent.*
The potential energy surface of the reactant is in blue and that of the product is in red. The y-coordinate represents the energy and the x-coordinate represents the reaction coordinate which accounts for all the changes in the position of the nuclei from the reactants to the products.

The theory proposed that the kinetics of the reaction is determined by the activation barrier ($\Delta G^{\ddagger}$), which in turn depends on the driving force (-ΔG^{o}) and reorganizational energy (λ). The driving force is the difference between the reduction potential of the electron donor (D) and acceptor (A). The reorganizational energy comprises of inner-sphere (ligand) and outer sphere (solvent) nuclear arrangements that accompany the electron transfer. In Figure 1-12, it is the energy of the reactants at equilibrium nuclear configuration of the products. The rate of electron transfer is given by,

$$k_{ET} = \sqrt{\frac{4\pi^3}{h^2\lambda RT}}\ {H_{AB}}^2 \exp[-\frac{(\Delta G^0 + \lambda)^2}{4\lambda RT}] \tag{1-1}$$

where, λ is the reorganizational energy, ΔG^0 is the driving force, $\mathrm{H_{AB}}$ is the electronic coupling term, *R* is the gas constant and *h* is the Planck's constant. It can be seen from the exponential part of the equation that the rate of electron transfer is highest when the values of the driving force and the reorganization energy are equal ($-\Delta G^0 = \lambda$), there will be a decrease in the electron transfer rate as ΔG^0 continues to rise. This is also known as the inverted effect. An important inference from Marcus theory is that the nuclear rearrangements that accompany the ET must be powered by the reaction driving force.

The electronic coupling matrix element is a description of the overlap between the localized donor and acceptor wave functions. More overlap leads to better electronic interaction. In proteins, the value of H_{AB} is quite small and depends on the distance between the donor and acceptor [101]. The distance dependence of the H_{AB} is expressed by

$$H_{AB}(r) = H_{AB}(r_0)exp\left(-\frac{\beta(r - r_0)}{2}\right) \tag{1-2}$$

where, *r* is the distance between the donor and acceptor and β is the decay factor. It is seen from equation (1-2) that the coupling is exponentially dependent on the distance between the redox centers, which, in turn, translates to distance dependence in the rate of ET. The value of β depends on the bridging medium between the redox centers [103]. Mathematically, the medium can be broken into n identical repeat units. The electronic coupling matrix element can now be described as the coupling between electron donor (D), electron acceptor (A) and their bridge, $(h_{Db}h_{bA})$, the coupling between the bridging unit themselves (h_{bb}) and the energy required to place the electron on the bridge [104].

$$H_{AB} = \frac{h_{Db}}{\Delta\varepsilon}\left(\frac{h_{bb}^{n-1}}{\Delta\varepsilon^{n-1}}\right)h_{bA} \tag{1-3}$$

However, the bridging medium itself is composed of a complex array of bonded and non-bonded contacts. The tunneling pathway model breaks the bridging medium into components linked by covalent bonds, hydrogen bonds, and through-space jumps [105][106], where each component is assigned its own decay constant $(\varepsilon_c, \varepsilon_H, \varepsilon_s \text{ respectively})$. The total electronic coupling can be represented as a repeated product of the couplings of the individual components.

$$H_{AB} = \pi\varepsilon_c\pi\varepsilon_H\pi\varepsilon_s \tag{1-4}$$

To summarize, the ET in biological systems is made efficient by protein folds which create a fine balance between the driving force and reorganizational energy. It also accounts for adequate electronic coupling between the donor and acceptor by a well-engineered system of covalent bonds, hydrogen bonds and through-space jumps through which the electron can tunnel.

1.1.3.2 Long Distance Electron Transfer and “Hopping”

Experiments have shown that the value of the β is lower for proteins than for water or space [107]. Also, the protein fold is able to exclude water molecules and utilize the vast network of hydrogen bonds to minimize the reorganization of ligands about the metal during electron transfer [103]. However experiments have shown efficient ETs only up to 15 Å [108][109]. For longer distances the ET is expected to be in order of ms and yet the ET has been found to be very fast over longer distances as well $(k_{obs}(s^{-1}) = (10^2 - 10^6)$. It is speculated that faster kinetics can be achieved through a multistep tunneling mechanism [110][111][112]. By this mechanism, the bridging protein medium not only electronically couples the electron donor and acceptor, but is also oxidized and reduced. The participation of the amino acids in the protein fold makes this ET a multistep tunneling process, also known as “hopping”. The long distance ET transfer can now be broken into multiple tunneling steps, separated by redox active intermediates. Since the ET rates are exponentially dependent on distance, the kinetics of multiple short ETs will be orders of magnitude faster compared to long single-step ET between the donor and acceptor. Radicals of amino acids such as tryptophan, tyrosine, cysteine and glycine play an important role in biology and can be important intermediates in multistep channeling [113][114]. Study of the electrode potential of the amino acids indicate that tryptophan and tyrosine are easiest to oxidize and are likely candidates through which multistep tunneling can occur[115].

1.1.3.3 Rate of ET and Significance of Protein Secondary Structure

The electron tunneling pathway model predicts a dependence of the ET rate upon the secondary structure of the protein through the following relation [116]:

$$k_{ET} = (0.6)^{2N_c}.(0.36)^{2N_H}(0.6)^{2N_S} exp\left[-3.4\text{Å}^{-1}\left(R_{space}\right)\right](FC) \qquad (1\text{-}5)$$

where, k_{ET} is the ET rate, N_c, the number of covalent bonds, N_H, is the number of hydrogen bonds, N_S, is the number of through-space contacts, and R_{space}, is the sum of all through-space contact distances (measured against a reference of 1.4 Å covalent bond) that lie in the dominant coupling pathway, and *FC* is the Franck-Condon factor. This dominant coupling pathway is the sequence of covalent bonds, hydrogen bonds and through-space contacts the electron is most likely to traverse as it tunnels from donor to acceptor. At a fixed donor and acceptor distance, the N_H and N_c are smaller for a β-strand pathway than for an α-helical pathway. It has been shown that β-strand results in a stronger, more direct pathway since tunneling through it only requires covalent bonds. The α-helix on the other hand necessarily includes the hydrogen bond jumps and a more circuitous bonded path [117][118][119].

1.1.3.4 ET through Solvent

A study conducted by Beratan et al, shows that water molecules positioned in the nearly infinitesimal gap between two docking proteins create unexpectedly favorable conditions for the electron to tunnel from one protein to another[120]. It is already known that “proteins folding” into the complex three-dimensional space makes it easy for the electrons to tunnel quantum mechanically as opposed to moving through empty space [107]. Solvent molecules have been shown to mediate electron tunneling when the distance between the donor and acceptor is within a certain range (~9-12 Å) [121]. Calculations show that solvent molecules can form an organized cluster between the donor and acceptor, providing the electron multiple pathways through these water molecules.

ET in PHM has been an intensely debated topic. Many theories have been put forward to explain the ET in PHM, some of the important ones are;

A) Superoxide channeling: this theory proposed that the electron was transferred over 11 Å to the M-site by the diffusion of a superoxide radical intermediate, formed at the H-site. This proposal stemmed from FTIR studies which showed that substrate binding near the M-site turned on binding of carbon monoxide at the H-site [122]. This result has been recently reinterpreted, and superoxide channeling is no longer considered a viable mechanism.

B) Domain movement: according to this theory, the ET occurs due to the direct interaction of the H-site with the carboxylate of the substrate, bound near the M-site. It was proposed that since the copper at the H-site is weakly bound to the three histidines (as shown by the K_d values), it is capable of exhibiting swinging motion, allowing interaction with the substrate [123]. Support for this mechanism has unexpectedly come from a recent crystal structure of DβM which shows a conformation with a much reduced distance (~4 Å) between the copper atoms [124].

C) Substrate-mediated: the ET was proposed to take place via a pathway involving H108, Q170, a water molecule and the peptide substrate. Evidence from crystallographic studies which showed hydrogen bonds between the key residues (H108 &Q170 , and Q170, water & substrate) provided support to this theory [125].

D) Ordered solvent : proposed that the ET takes place via a raft of ordered solvent molecules across the intersite cavity along with Y79 residue [126][127][128].

Although various theories exist, none of them account for all the available data, making long distance ET an intensely debated topic. The structural changes on reduction of the copper centers and the fixed distance of 11 Å between the copper sites pose challenges to an efficient ET. Despite this, the ET from CuH to the CuM-site has been found to be fast (K_{ET} ~40 s^{-1}). Chapter 4 deals in detail with the ET in PHM.

Despite different studies, which have revealed a lot about the reaction mechanism and unique structural features of PHM, a number of questions remain unanswered. So far, the nature of the PHM intermediate has also been speculative. Besides a crystal structure of PHM with oxygen [69], it has not been possible to detect the copper-oxygen intermediate biologically in any other way. This research is aimed to shed light on the above two questions. Chapter 3 is a spectroscopic study of the copper sites in order to study their unique and distinct roles. Chapter 4 is based on reduction kinetic studies on PHM which led us to propose a theory of bifurcated ET pathway, while chapter 5 is based on our efforts to generate and characterize the PHM superoxo/peroxo intermediate.

CHAPTER 2. TECHNIQUES AND METHODS

In a bid to understand the results, a brief outline of the principles behind the various spectroscopic techniques is being provided in this chapter. The generation, production of PHM and its various mutants, as well as protein purification is also discussed.

2.1 Ultraviolet-visible Spectroscopy

Absorption measurements based on ultraviolet and visible radiation are one of the most common methods used for quantitative analysis. This technique was applied during the stopped-flow kinetics and to quantify the protein and copper azido complex in the azide binding studies during the course of the research.

Ultraviolet-visible (UV/vis) spectroscopy is the study of the transitions involved in the rearrangements of valence electrons. The electronic transitions can be classified under three categories, based on the type of electrons involved:

1. σ, π (which participate directly in bond formation) and n electrons (localized and non-participating)
2. *d* and *f* electrons
3. Charge transfer electrons

Figure 2-1 depicts the electronic molecular orbitals and the electronic transitions.

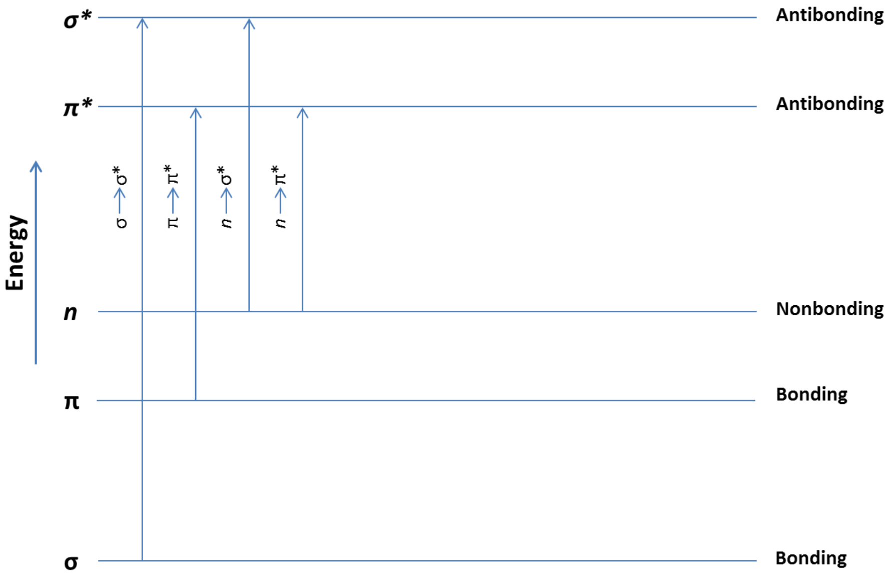

Figure 2-1 *Electronic molecular energy levels*

The Cu(II) form of copper has a d^9 configuration, leading to an unpaired electron in a half-filled orbital and electrons in lower lying d-orbitals can be excited so as to populate this half-filled orbital. These d-d transitions can be observed as weak absorption bands.

Another important phenomenon observed by this technique is the ligand to metal charge transfer (LMCT) transitions. These transitions arise from the interaction of high valent metal ions with an electron rich ligand, causing large energy absorption. For analytical purpose, species that exhibit charge transfer bands are important due to their large molar absorptivities ($\varepsilon > 10000\ M^{-1}cm^{-1}$). In order to observe charge transfer bands, transfer of an electron from donor to the orbital associated with the electron acceptor must occur. Usually in the charge transfer complexes involving the metal ion, the metal serves as an electron acceptor. Copper forms a copper azido complex during reaction with azide during the binding studies. The azide serves as an electron donor and a charge transfer band at 390 nm is observed due to the electron transition that takes place from the molecular orbitals on the azide, to a nonbonding or antibonding orbital located on the copper. Besides the azide binding assay, UV/vis spectroscopy was also used for kinetic experiments of PHM and its mutants on a ms time scale, using high sensitivity photodiode array detectors.

2.2 Electron Paramagnetic Resonance

EPR spectroscopy is based on the absorption of electromagnetic radiation in the microwave region by a paramagnetic sample placed in a magnetic field. Fundamentally, this technique can be applied to any species containing one or more unpaired electrons. This includes inorganic and organic free radicals, triplet states (e.g., O_2) and systems that contain transition metals. Since this technique is exclusive for paramagnetic substances, it is limited to investigating the Cu(II) d^9 or the cupric form of copper.

2.2.1 Theory

To understand EPR consider an isolated electron, which behaves as magnet/magnetic dipole of magnetic moment ‘μ’ due to its intrinsic angular momentum. Based on the orientation with the magnetic field, the magnetic moment acquires two states when subjected to a magnetic field. The energy of the two states of the magnetic moment is given by:

$$E = \mu B_0 \tag{2-1}$$

$$\mu = g_e \beta \boldsymbol{S} \tag{2-2}$$

where, μ is magnetic moment and B_0 is the external magnetic field. Equation (2-2) relates the magnetic moment of an electron to the electron spin, ***S***, via quantities g_e and β. The quantity β is the Bohr magneton. The numerical value of β is 9.274-10^{-28} J.G^{-1}. The second quantity, g_e, is the spectroscopic *g*-factor of the free electron. The spectroscopic *g*-factor depends on the size of the nucleus and also contains chemical information about the interaction between the electron and the electronic structure of the molecule. The numerical value of *g* for the free electron is 2.002319, which is very near 2. When an electron is placed in a molecule, it experiences magnetic moment due to the intrinsic spin, as well as, the orbital angular momentum. The quantum mechanical equivalent of equation (2-2) can be decribed by some simplification as

$$\boldsymbol{H} = g_e\beta\boldsymbol{S}.B_0 \tag{2-3}$$

where, ***H*** is the Hamiltonian and ***S*** is the symbol of the total spin associated with the electron or the spin quantum number. The dot product of ***S***.B_0 can be replaced by m_s, the projection of ***S*** onto B_0, multiplied by the magnitude of B_0 to give equation (2-4).

$$E = g_e\beta m_s B_0 \tag{2-4}$$

For S=1/2, the m_s can have only two values: ½ if the direction of the component of the spin on the z axis is parallel to the magnetic field and -½ if antiparallel. As seen in Figure 2-2, the energy difference between the two states thus becomes,

$$\Delta E = g_e\beta B_0 \text{ or } h\upsilon = g_e\beta B_0 \tag{2-5}$$

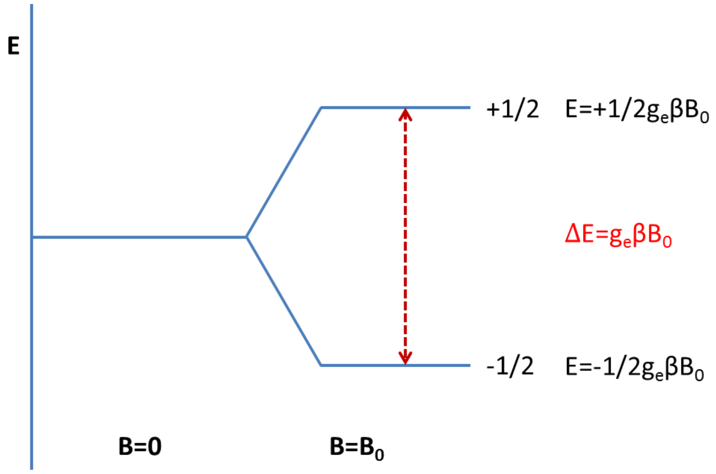

Figure 2-2 *Splitting of the electron energy levels in an applied magnetic field.*

When an unpaired electron pair is subjected to an increasing magnetic field with constant frequency, absorption occurs when the resonance condition is met. The frequencies required for the EPR experiment are generally in the microwave region of the spectrum (2-36 GHz), and are provided by stable oscillators such as klystrons. Most spectrophotometers operate at 9 GHz (called X band), a frequency which provides a balance between sensitivity and ease of sample handling. Since the frequency of the instrument is known, the magnetic field required for the resonance condition can be used to calculate *g.* In practice, a typical EPR spectrum is the first derivative of the conventional absorption curve.

2.2.2 *g* Anisotropy

It is seldom that an isolated unpaired elctron is studied. Usually it is under the influence of not only the nucleus, but also the surrounding ligands. The magnetic moment of an unpaired elctron in a molecule comprises both the spin and orbital magnetic moments.

Low symmetry molecules have very little or no orbital magnetic moment contribution. The phenomenan of spin-orbit coupling is able to restore some of the orbital contribution and leads to deviation of the *g*-value of the free electron.

$$\Delta g = g - g_e \tag{2-6}$$

The equation (2-5) can be now written as:

$$\Delta E = g\beta B_0 \tag{2-7}$$

The *g*-factor reveals a lot of information about the electronic nature as well as chemical nature of the molecule under study. Hence, the *g*-factor is aptly called the *fingerprint* of the molecule. For every paramagnetic substance there is a unique axis system known as the principal axis system. The *g*-factors measured along these axis are called g_x, g_y and g_z. Based on their values the following cases of anisotropy are recognized:

(a) Isotropic ($g_x = g_y = g_z$)
(b) Axial ($g_x = g_y > g_z$) or $g_x = g_y < g_z$ The g_x and g_y are also refered to as $g_{||}$ and $g_{\perp}$ respectively.
(c) Rhombic ($g_x \neq g_y \neq g_z$)

Hyperfine splitting and super-hyperfine splitting are additional contributions to the EPR envelope.The interaction of the unpaired electron with the nuclear magnetic moment is termed as nuclear hyperfine interaction, if it results from the nucleus where the unpaired electron originates, and superfine if it is due to a neighbouring nucleus. The resonance is split into a multiple line pattern with the number of lines given by 2nI+1, where n is the number of nuclei with nuclear spin I. The following Figure 2-3 shows a typical axial spectrum for a powder Cu(II) compound.

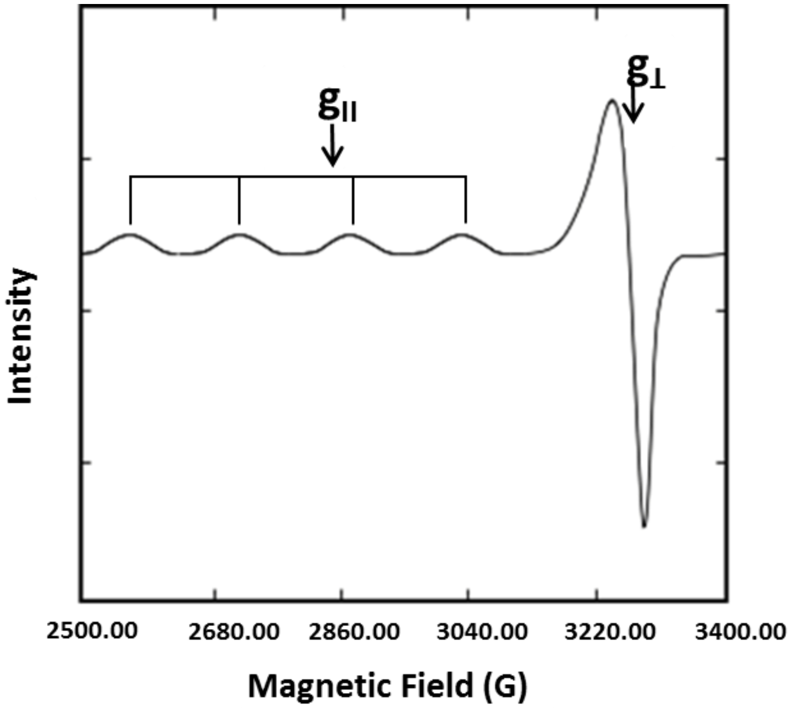

Figure 2-3 *Typical axial spectrum of a powder Cu(II) compound.*

Cu(II) centers typically have tetrahedral, or axially elongated octahedral geometry. Their spectra are anisotropic and generally give signals of the axial or orthorhombic type. As seen in Figure 2-3, the overall spectral envelope is axial with $g_{\parallel}$ smaller than $g_{\perp}$. The hyperfine interactions can be observed for the peak at $g_{\parallel}$, which has been split into four lines of equal intensity. This implies the presence of a nuclear spin of $\frac{3}{2}$ which is characteristic of Cu(II) metal. Coordination geometry of the Cu(II) compounds can also be determined from the EPR spectra, making this a very useful technique.

2.3 X-ray Absorption Spectroscopy

X-ray absorption spectroscopy (XAS) is a powerful tool for studying the structure of enzymes containing metals. The x-rays are high energy (~500 eV-500 keV) photons and have wavelength the order of atomic dimensions, a feature which makes them useful for studying and probing molecular structure.

2.3.1 Theory

X-ray absorption spectroscopy is basically the measurement of the energy dependent absorption coefficient, μ, which is the probability that x-rays will be absorbed by the sample according to Beer's law:

$$I = I_0 e^{-\mu t} \tag{2-8}$$

Where I_0 is the intensity of the incident radiation, t is the sample thickness, and I is the intensity of the transmitted radiation. A typical X-ray absorption spectrum (Figure 2-4) is obtained by plotting absorption on the y-axis versus the energy of the incident radiation on the x-axis, for a range of energies.

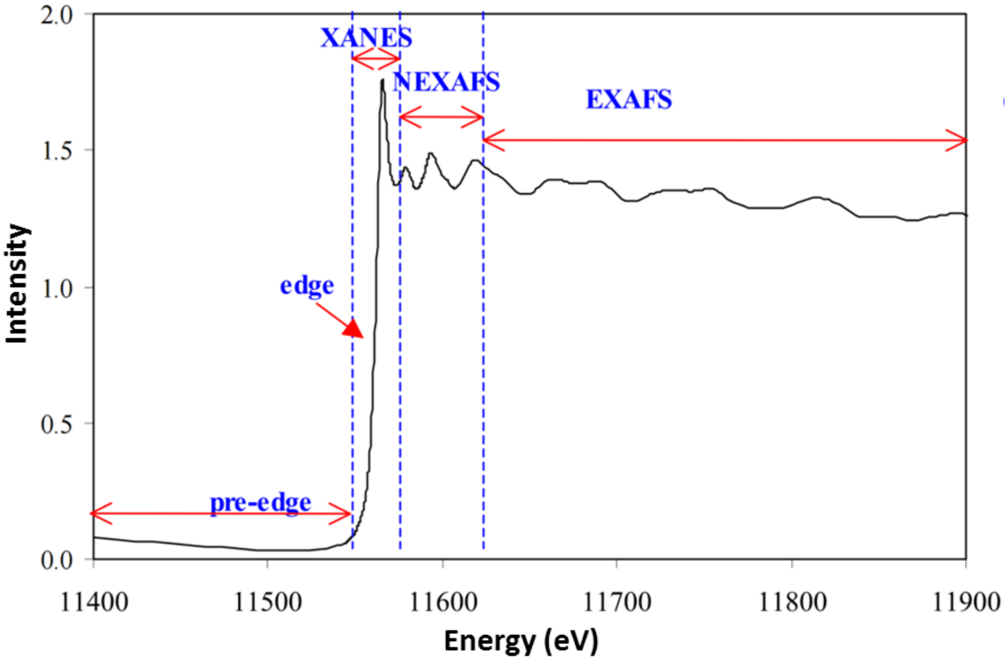

Figure 2-4 *Representative x-ray absorption spectrum*

The sample is bombarded with X-rays; some of the X-rays absorbed by the metal center carry enough energy to eject a core electron. The absorption is quantified by comparing the intensity of the incident radiation to the intensity of the transmitted radiation. The sharp rise in the absorbance is known as the edge. It represents the energy of the incident radiation required to eject an electron from the 1s orbital of the metal. For copper this energy is 8980 eV and is referred to as the copper K-edge. The peaks and other features on or near the edge are known as the x-ray absorption near-edge structure (XANES). They provide valuable information about the metal oxidation and coordination number. This region is sensitive to the oxidation state and the coordination number of the metal center. The quasiperiodic modulations in the x-ray absorption coefficient above the edge are referred to as the EXAFS (Extended X-ray Absorption Fine Structure). They arise due to the superposition of outgoing photoelectron wave with the backscattered waves from the surrounding ligands. This gives rise to the EXAFS modulations. As the modulations are the results of the photoelectron scattering from the surrounding ligands of the metal center, they carry information about the local environment, namely the number, type and the distance from the metal center. The quasiperiodic modulations of EXAFS can be represented by the equation:

$$\chi(k) = \sum_j \frac{N_j f_j(\Pi, k)}{kR^2} exp^{\frac{-R}{\lambda_f}} exp^{(-2\sigma^2 k^2)} \sin[2kR + \alpha(k)] \tag{2-9}$$

Where $\chi(k)$ is the oscillations as a function of photo-electron wave number, N_j is the number of scattering atoms in a shell, $f_j(\pi, k)$ is the inherent backscattering amplitude for this type of scattering atom, R is the interatomic distance between the absorbing atom and the scattering atoms, λ_f is the mean free path, σ^2 is the rms deviation in the R, also known as the Debye-Waller factor and $\alpha(k)$ is the inherent backscattering phase shift for the absorbing atom.

2.3.2 Instrumentation

Figure 2-5 shows the experimental setup for an XAS experiment.

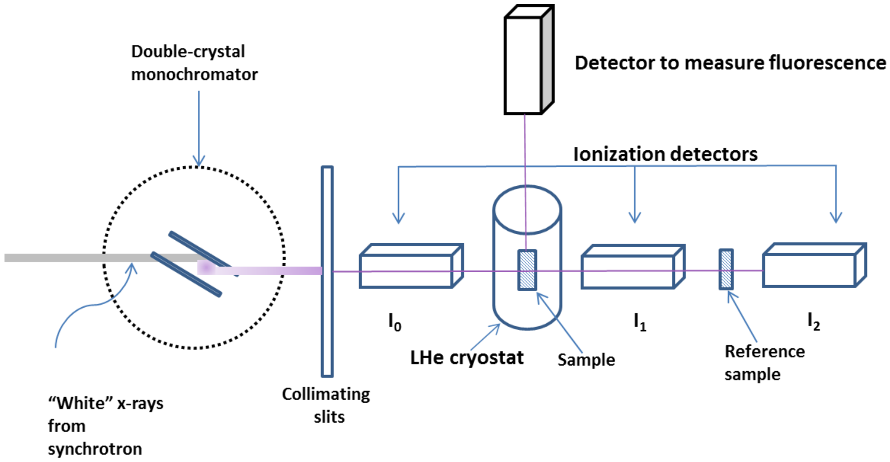

Figure 2-5 *Schematic representation of experimental set up for an XAS experiment*

The double crystal monochromator (DCM) is used to select and transmit x-ray radiation of the desired photon energy from incident white synchrotron radiation. The DCM uses two parallel crystals which can be rotated to select the desired energy x-rays by varying the bragg's angle ($n\lambda = 2dsin\theta$). All of the XAS measurements require determination of fraction of x-rays absorbed as a function of energy. There are two common ways to do this: Transmission and fluorescence. Transmission makes use of the ion chambers filled with inert gases. The x-rays passing through them ionize the gas resulting in a cascade of charge particles which are amplified and collected to form a measurable current. The fluorescence provides a better signal to noise ratio compared to that of the transmission measurement. When the core electron is ejected the hole is filled by an electron from n=2 level to the 1s level. This results in emission of an intense x-ray emission photon. This is the Kα fluorescence and the fluorescence method is based on monitoring this strong emission. The Kα emission energy is fixed for a particular metal. This is a very useful feature which is applied to get rid of the background noise. The fluorescence detectors are made of silicon or germanium chips. The sensitivity is related to the number of detector channels available.

2.3.3 Data Analysis and Information

The pre-edge provides information about the ligand field and the oxidation state of the metal. The small peaks in the pre-edge region are due to specific electronic transitions which depend on the molecular symmetry. High centrosymmetric molecules exhibit low pre-edge intensity compared to the low centrosymmetric molecules. The edge is the most informative about the oxidation state, coordination number and covalency of the metal.

The EXAFS spectra obtained is processed and the FT function is applied to it to generate a Fourier transform. The Fourier transformation does a frequency analysis of the EXAFS yielding a peak at the frequency of each sine wave component in EXAFS (Figure 2-6). The sine wave frequency is directly proportional to the metal-ligand separation distance; the FT generates a set of peaks in radial distance space with each peak representing a particular shell of atoms.

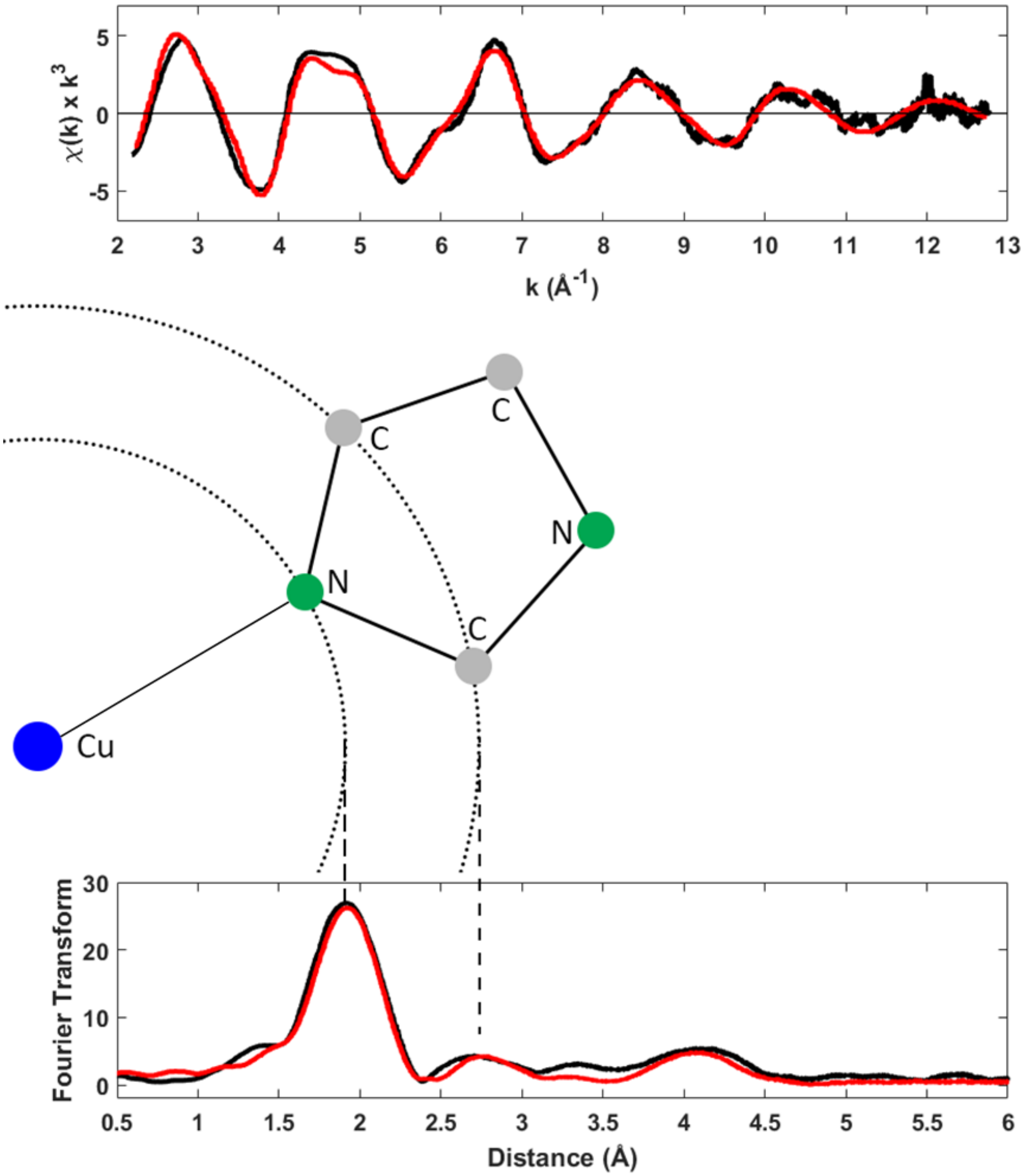

Figure 2-6 *Representation EXAFS (top panel) and FT (bottom panel). The experimental and simulated traces are in black and red, respectively.*

To gain further information simulations and EXAFS of model compounds are used to determine the identity of the ligands and distance from the metal center. XAS was used extensively to study the structural changes accompanying the single-site mutants of PHM under various conditions.

2.4 Fourier Transform Infrared Spectroscopy

FTIR is based on the interaction of the matter with electromagnetic radiation in the infra-red (IR) region. Infra-red radiation is not energetic enough to cause electronic transitions as in the case of UV-vis and x-rays, but can couple with the molecular vibrations of the molecule and excite them to a higher vibrational level. The absorption of infra-red radiation is thus confined largely to molecular species that have a small difference between their vibrational and rotational states.

2.4.1 Theory

A molecule which undergoes a net change in its dipole moment, as a consequence of its vibrational and rotational motion, produces an alternating field which is able to interact with the IR, leading to transfer of energy and change of amplitude of the molecular vibration. This phenomenon results in absorption of the IR radiation.

2.4.2 Instrumentation

The FTIR spectrophotometer works on the principle of Fourier transform. The mathematical expression of Fourier transform can be expressed as

$$F(\omega) = \int_{-\infty}^{+\infty} f(x) e^{i\omega x} dx \qquad (2\text{-}10)$$

The inverse Fourier transform is

$$f(x) = \frac{1}{2\pi} \int_{-\infty}^{+\infty} F(\omega) e^{-i\omega x}\, d\omega \qquad (2\text{-}11)$$

where ω is the angular frequency and x is the optical path difference. $F(\omega)$ is called the Fourier transform and $f(x)$ is called the interferogram. The typical set up of the instrument used for recording an interferogram is given in Figure 2-7.

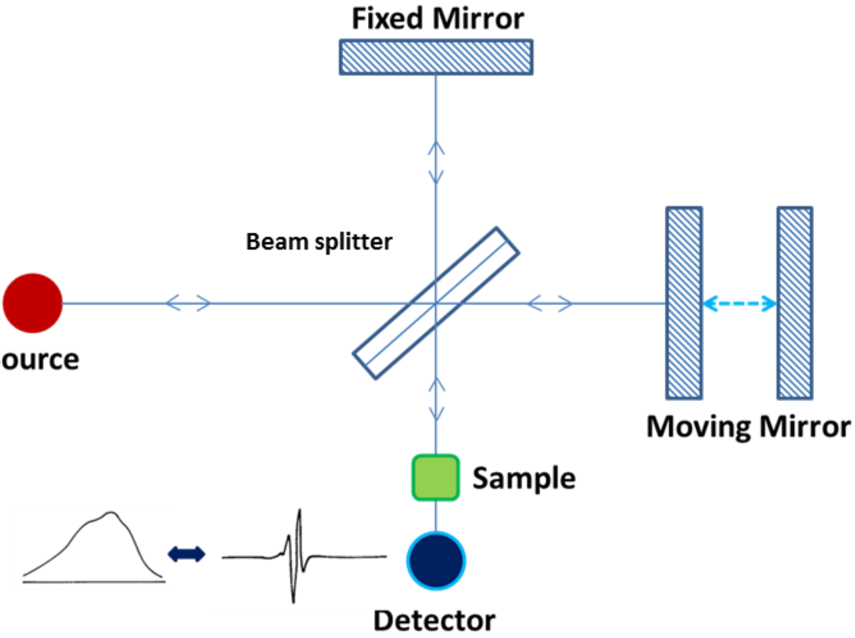

Figure 2-7 *Typical setup of an FTIR experiment*

The light from the source is directed towards the beam splitter, which reflects half of the light to the fixed mirror and the other half is transmitted to the moving mirror (Figure 2-7). The reflected beams from both the mirrors pass through the beamsplitter to the detector. The signal recorded is sinusoidal and is called an interferogram. A background spectrum is taken first, followed by the sample. The sample spectrum is the ratio of the spectrum containing sample against that of the background.

FTIR was used to probe the copper centers in PHM by studying their carbon monoxide complexes. Carbon monoxide is a dative ligand which increases the electron count of the copper center by two units without affecting the oxidation state. There are two bonding interactions between the copper and the carbon monoxide: a two electron donation from CO to the vacant copper d-orbital and interaction of the filled metal d-orbital with the empty π^* orbital of the carbon monoxide ligand. The π back bonding causes the bond order to decrease on the carbon monoxide molecule. As a consequence the C-O stretching frequency also decreases. It is important to note that the C-O stretching frequency also depends on the number and type of ligands surrounding the copper atom. FTIR has proven to be a technique which is sensitive to changes in the geometry and coordination of the copper center.

2.5 Production of PHM and its Mutants

Figure 2-8 depicts the arrangement of PAM, a bifunctional enzyme, which is subjected to alternative splicing in a tissue specific manner to give two separate enzymatic domains of PHM and PAL.

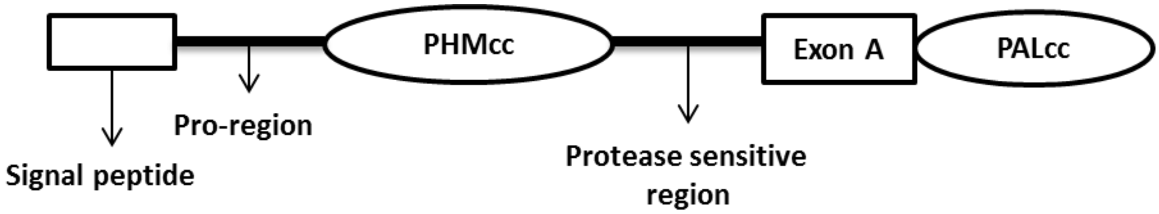

Figure 2-8 *Schematic representation of the PAM bifunctional enzyme*

It was discovered that just the signal peptide and the PHMcc core sequence was enough to catalyze hydroxylation of the substrate [129]. Hence a truncated form consisting of the signal peptide and PHMcc core sequence (ΔPro 382s) was selected for further studies. The sequence of PHMcc (ΔPro 382s) is provided Figure 2-9.

```
AGCAGAGCTCGTTTAGTGACCGTCAGATCGCCTGGAGACGCCATCCACGCTGTTTTGACCTCCATAGAAGACACCGGGACCGATCCAGCCTCCGCGGCCGGGAACGGTGCATTGGAAC
GCGGATTCCCCGTGCCAAGAGTGACGTAAGTACCGCCTATAGAGTCTATAGGCCCACCCCCTTGGCTTCTTATGCGACGGATCCCGTAATAAGCTTGAGGTGTGGCAGGCTTGAGATCT
GGCCATACACTTGAGTGACAATGACATCCACTTTGCCTTTCTCTCCACAGGTGTCCACTCCCAGGTCCAACTGCAGCTCGGTTCTATCGATAAGCTTGCCGCCACCATGGCCGGACGCGC
CCGCAGCGGTCTGCTACTGCTGCTGCTGGGGCTGCTCGCCCTGCAGAGCAGCTGCCTGGCCTCATTTTCCAATGAATGCCTTGGTACCATTGGACCAGTCACCCCTCTTGATGCATCAG
ATTTTGCGCTGGAT
ATTCGCATGCCTGGGGTTACACCTAAAGAGTCTGACACATACTTCTGCATGTCCATGCGTCTGCCTGTGGATGAGGAAGCCTTCGTGATTGACTTCAAGCCTCGTGCCAGCATGGATAC
TGTCCACCATATGCTGCTGTTTGGATGCAATATGCCCTCGTCCACTGGAAGTTACTGGTTTTGTGATGAAGGAACCTGTACAGATAAAGCCAATATTCTATATGCCTGGGCAAGGAATG
CTCCCCCCACCCGGCTCCCGAAAGGTGTTGGATTCAGAGTTGGAGGAGAAACTGGAAGCAAATACTTCGTCCTTCAAGTTCACTATGGCGATATCAGTGCTTTTCGAGATAATCACAAA
GACTGCTCTGGCGTGTCCGTA
```

Figure 2-9 *Sequence of PHMcc (ΔPro 382s)*

This sequence was introduced into the multiple cloning site of the expression vector pbluesript (pBS ΔPro 382s). PHM mutants were created by introducing mutations in the ΔPro 382s by using Splicing by Overlap Extension (SOEing) [130]. The PCR products were purified, digested and ligated to the expression vector pbluescript. The clones were selected after sequence analysis and the cDNA was then inserted into pCIS2CXXNH, a mammalian expression vector [131].

2.5.1 Cell Growth and Bioreactor Inoculation

The chinese hamster ovary cells (CHO DG44), stably transfected with ΔPro 382s and recombinant PHMcc were allowed to grow in the Dulbecco's Modified Eagle Medium (DMEM/F12) medium, a standard mammalian cell culture medium, containing 10% fetal clone for nutrition in triple nunc flasks. When the cells reached 70-80% confluency, they were trypsinized and reuspended in the DMEM/F12 medium containing 10% serum prior to bioreactor innoculation in the bioreactor. The cells were allowed to settle on the hollow fibers in the bioreactor. Once the cells had grown and expanded in the bioreactor, the bioreactor spent media was harvested on a regular basis and stored in a refrigerator maintained at 4° C. A brief description of the structure and functioning of bioreactor is presented in the next section.

2.6 Hollow Fiber Bioreactors

The hollow fiber bioreactor is a mammalian culturing system made of hollow, semipermeable capillary membranes arranged in a parallel array, which is housed inside a cylindrical polycarbonate shell. The cylindrical shell has two pairs of ports (inlet and outlet) as well two compartments, the intracapillary compartment space (ICS) within the hollow fibers, and the extracapillary space (ECS) surrounding the hollow fibers, as seen the Figure 2-10. The hollow fibers are permeable and act as filters with a MWCO range of 10-30 kDa.

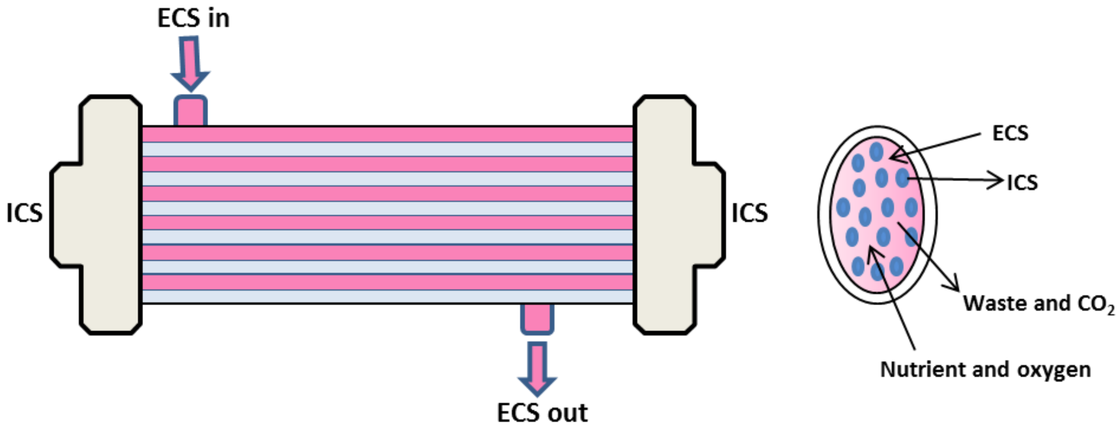

Figure 2-10 *The schematic representation of a typical hollow-cell bioreactor.*

The cells are allowed to grow and expand in the ECS, while the ICS is used for pumping the cell culture medium and for delivering the oxygen and the nutrients. Two ports are used to carry and exit the cell culture medium into the ICS. Similarly, another two are used for the cell culture medium to enter and exit the ECS. The ICS culture medium enters through a lower port and flows through the length of the ICS before exiting through an upper port. As the mammalian cells grow and expand the waste products and CO_2 are also released inside the ICS medium through the porous fiber cells, allowing the cells to grow without any adverse effects due to toxicity. The waste products and carbon dioxide are removed by the action of the pumped medium. As the ECS culture medium enters through a lower port and flows through the dense cell culture it carries with it the product of interest, in our case the secreted protein PHM, which exits through the other port and is collected in a bottle maintained at 4^{o} C. The ICS and ECS are both connected to an expansion chamber which is sequentially placed under positive pressure to circulate the medium back and forth among the growing cell mass [132]. Since the fibers function as filters, two types of medium flow provide the low and high molecular weight nutrients. ICS is basal medium like the DMEM/F12 without any growth supplements. The ECS medium is the basal medium plus growth supplement added to it, such as the FBS (Fetal Bovine Serum). The expensive supplement is only added to the ECS medium and since the rate of consumption is 1/50-1/100th that of ICS medium, separating the two mediums is very cost effective. The rate of harvesting the ECS media is also low making it possible to obtain the PHM in highly concentrated amount. The maximum production of PHM obtained is up to 25 mg/day. The bioreactor remains productive for up to a year [132]. The bioreactor pathway also has other components like the gas exchange cartridge and the pH probe used to monitor and feedback control of the pH, temperature and circulation rates.

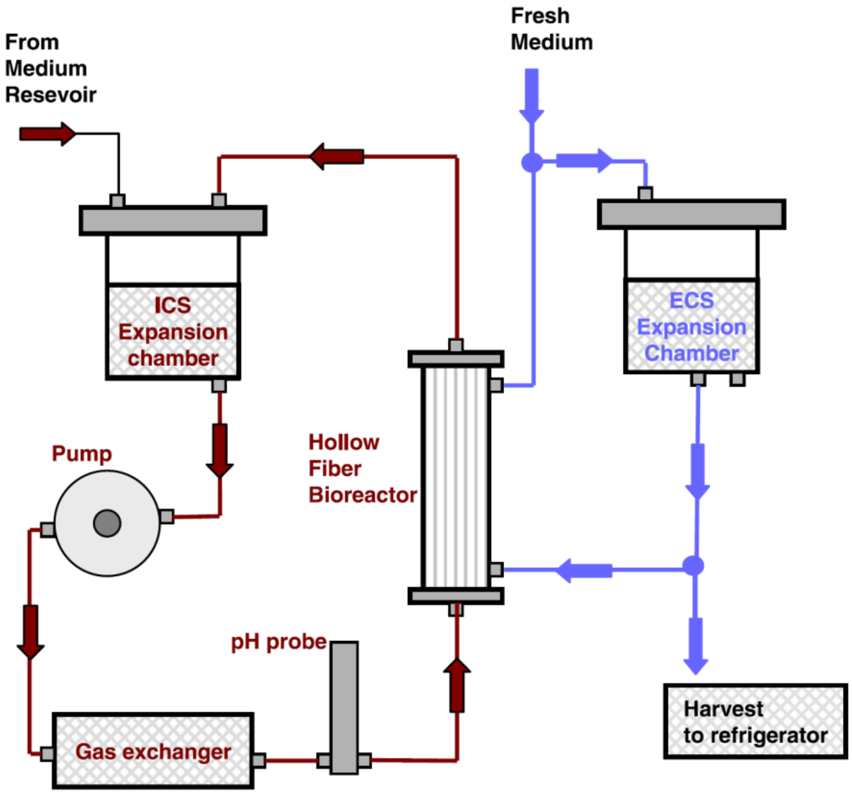

Figure 2-11 *Schematic of the flow paths in the bioreactor B2. Reprinted with permission from (Bauman et al, ScienceDirect, 2007, 51(1)). Copyright (2007) Elsevier Ltd.*
The red lines indicate the ICS circuit and the blue lines indicate the ECS circuit. Fluid exchange between the two circuits can only occur by diffusion across the semipermeable hollow fibers of the bioreactor cartridge.

The Accusyst-Mini Max (Biovest International Minneapolis, MN) hollow –fiber Bioreactors were used to grow the CHO DG44 cells which were stably transfected with the WT PHM and the PHM mutants (H107A, H108A, H172A, H242A and H107AH108A).

2.6.1 Purifying PHMcc Protein

The bioreactor harvest (spent media) was collected for a month. This amounted to approximately 300 mL, for WT PHM as well as the mutants. To precipitate the protein, ammonium sulfate was added to the spent media and left to stir for 45 minutes at 4^{o} C.

The precipitated protein was pelleted by use of centrifugation and suspended in 24 mL of 50 mM potassium phosphate buffer (pH 7.5), containing 0.01 % triton X-100. The sample was subjected to centrifugation to remove the cell debris and filtered through a 0.45 µm sterile filter. The filtered sample was applied to a 26/60 Hiload/Superdex 75 prep gel filtration column (Pharmacia) at a flow rate of 3.5 mL/min. To ensure good resolution, only 12 mL of sample was injected once, with no more than two injections a day. The main protein fractions were pooled, concentrated and dialyzed against tris-acetate buffer (20 mM, pH 8.3) overnight at 4^{o} C.

The next step in purification process involved passing the dialyzed protein over an ion-exchange column on the Biocad 700E work station for Perfusion Chromatography (Applied Biosystems). The anion exchange column was primed, calibrated and equilibrated with tris-acetate buffer (20 mM, pH 8.3). About 5-7 mL protein was loaded at 2 mL/min on the ion-exchange column. The protein peak was monitored using a UV/vis dual wavelength detector set to 214 nm and 280 nm. The PHM protein was eluted using a NaCl salt gradient (0-300 mM). The PHM protein eluted around 120 mM-150 mM. The fractions were run on an SDS PAGE and those found to be more than 95% pure were pooled, concentrated and dialyzed against 20 mM sodium phosphate buffer (pH 8.0), overnight at 4^{o} C prior to reconstitution with cupric sulfate.

CHAPTER 3. THE STUDY OF SINGLE-SITE PEPTIDYLGLYCINE MONOOXYGENASE (PHM) MUTANTS BY BINDING OF THE COPPER AND SILVER TO REVEAL THE STRUCTURE AND CHEMISTRY OF THE INDIVIDUAL COPPER CENTERS[1]

3.1 Introduction

Peptidylglycine monooxygenase catalyzes the final step in the biosynthesis of amidated peptides that serve as important signaling molecules in numerous endocrine pathways[133]. Specifically, the enzyme hydroxylates the α-C atom of the glycine-extended C-terminus of the propeptide in a reaction involving the transfer of four electrons to O_2, two from the C−H bond and two from an external reductant. To conduct this conversion, the enzyme stores the external electrons on a pair of copper atoms that are termed CuH and CuM [also denoted H-site and M-site, respectively (Figure 3-1)] that are reduced to the Cu(I) state by an external reductant, which is ascorbate under physiological conditions. During turnover, oxygen is believed to bind to Cu(I) at the M-center where it forms a Cu(II)-superoxo species. This activated intermediate then abstracts a H-atom from the α-CH entity of the nearby substrate to form peroxide and a substrate radical. O-O bond cleavage coupled to radical rebound generates a hydroxylated product and a high-valent [Cu(III)-oxo or Cu(II)-$O^{\bullet-}$] that is reduced to the resting enzyme by a second electron transfer from H to M.

---

[1] This chapter has been published in a similar form in *Biochemistry,* 2014, 53, 1069-1080.

This mechanism has attracted much attention because of a number of unique attributes, many of which have been revealed by crystallography (Figure 3-1) [134][69][35][125][135]. First, the copper centers are 11 Å apart, separated by a solvent-filled cleft in the protein that imposes restrictions on intrasite electron transfer [136][137][122][127].

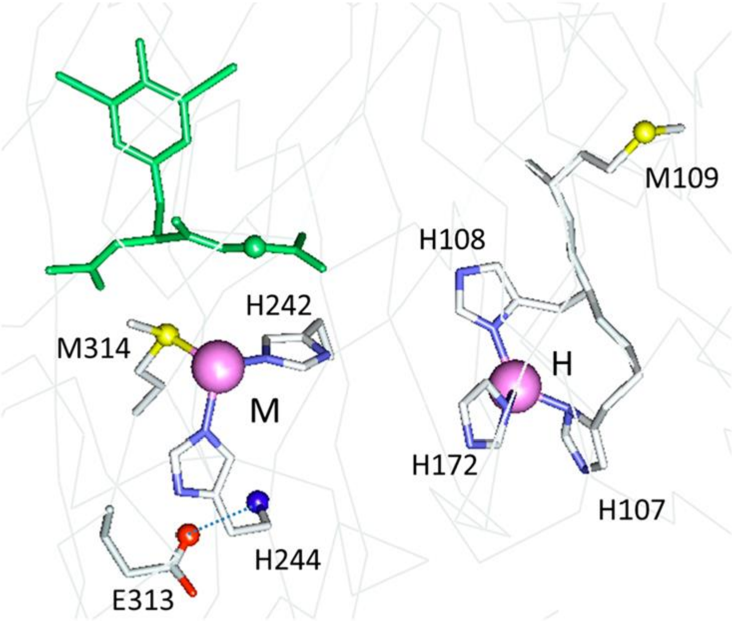

Figure 3-1 *Structure of the PHM active site taken from Protein Data Bank entry 10PM. The figure shows the H-site coordinated to the Nδ-atom of H107, H108 and Nε of H172, and the oxygen binding CuM-site (catalytic) to Nε of the H242 and H244 and the thioether S of the M314. The side chain of the conserved E313 is shown forming an H-bond to the main chain amide nitrogen of H244. The bound substrate (diiodotyrosylglycine) is colored in green.*

It has been proposed that the physical separation prevents the second electron from being transferred until after the enzyme has committed to catalysis, thereby harnessing the strong electrophilic reactivity of the Cu(II)−superoxo entity [45][138]. Second, the coordination chemistry at each copper is unusual. The M-site is coordinated by H242, H244, and a weak interaction with the thioether of M314 [66][55][46], which nevertheless plays a critical role in catalysis, because mutation to histidine, cysteine, or aspartate results in an ∼95% loss of activity [139][140]. The H-site is bound by three coordinating histidine residues, H107, H108, and H172 [66][141], mutation of any one of which also eliminates >95% of the catalytic activity. The H-site undergoes an unusual conformational change at low pH in which a methionine residue (part of a $H^{107}H^{108}M^{109}$ triad) coordinates to the copper and shuts off activity [67]. Furthermore, unlike similar sites in other copper proteins, H does not appear to bind exogenous ligands [134].

Understanding the individual roles of the electron transfer site (H) and the oxygen-activating site (M) centers is key to unraveling the overall catalytic mechanism. Much of the relevant chemistry, including the template for the binding of oxygen at CuM and the state of CuH immediately prior to ET, occurs in the Cu(I) state that is opaque to many traditional spectroscopic methods because of its d^{10} configuration. Available insight into the structure and reactivity of the Cu(I) forms of PHM and its variants has been derived from X-ray absorption spectroscopy, the one spectroscopic technique that can inform on the Cu(I) state [66][55][139][140][141][67][62], but the analysis gives only a structural perspective averaged over both copper centers. It is clearly important to obtain site-specific structure−reactivity data for the H- and M-centers individually, to assess the detailed role of each in the overall catalytic processes.

We have constructed and characterized two PHM variants that when metalated bind copper and silver at only a single center. The H242A variant is an M-site deletion mutant that removes one of the two histidines necessary for tight binding of copper to the M-site. In previous work [67], we showed that a similar deletion of one of three histidines at the H-site was insufficient to abrogate copper binding at this site. Accordingly, we constructed double mutant H107AH108A in which removal of two of three histidines now prevents metal binding at the CuH-center. Here we present a detailed study of each of these single site variants, in which we show that they do indeed report the individual chemistry and spectroscopy of each site.

3.1.1 Materials and Methods

Buffers and ascorbate were obtained from Sigma-Aldrich at a minimal purity of 99%. Beef liver catalase was acquired from Roche. Substrates Ac-Tyr-Val-Gly (Ac-YVG) and dansyl-Tyr-Val-Gly (dansyl-YVG) were purchased from Peptide International and American Peptide Co., respectively.

3.1.1.1 Construction of Mutants

All variants were constructed using the PHM catalytic core sequence (PHMcc) comprised of residues 42−356. The H107AH108A variant was constructed as previously reported [62][63]. H107AH108A was individually introduced into pBS.ΔProPHM382s (obtained as a gift from B. A. Eipper and R. E. Mains) using splicing by overlap extension (SOEing) [130]. Sense and antisense oligonucleotide primers (Table 3-1) encoding ∼20 bases downstream and upstream of the mutation were used for site-directed mutagenesis and paired with primers upstream and downstream of two restriction enzyme sites, ClaI and XbaI. Polymerase chain reaction (PCR) products were purified on agarose gels. Final PCR products were extracted with phenol and chloroform, digested using restriction enzymes (NEB), fractionated on agarose gels, purified via a Qiagen PCR kit, and then ligated into the pCIS.2CXXNH expression vector (also a gift from B. A. Eipper and R. E. Mains). Sequence analysis was performed on mutant clones, and Qiagen midi prep was used to ensure 20 µg/20 µL of recombinant DNA for transfection.

Oligo Name	Length	MW	Tm^0	GC%	Sequence
H107A108APHMCLAF	39	12021	85.3	53.8	AGCATGGATACTGTCGCCGCTATGCTGCTGTTTGGATGC
H107A108APHMXBAR	39	11955	85.3	53.8	GCATCCAAACAGCAGCATAGCGGCGACAGTATCCATGCT

Table 3-1 *Forward and reverse oligos used in construction of the H-site PHM single variant.*

3.1.1.2 Screening PHMcc Single-Site Mutants

CHO DG44 cells were transfected with the recombinant DNA using Lipofectamine 2000 (Invitrogen). The transfected cells were subsequently selected for *Dhfr* cell lines in α-minimum Eagle’s medium containing 10% dialyzed fetal bovine serum [63][142]. Only those cells that retained the *Dhfr* gene (colocated with PHM on the plasmid) were capable of growth under these conditions. Monoclonal cell lines were created by serial dilution into 96-well plates, to select for wells that contained single-cell colonies. These were passed individually into a fresh 96-well plate, grown to confluence, and screened via Western blotting for PHMcc production under similar conditions. The strongest producers were inoculated into a Hollow Fiber Bioreactor with a MWCO of 5000 (Fibercell Systems, Inc.).

3.1.1.3 Western Blot Analysis

CHO DG44 cells were incubated in DMEM/F12 medium containing 0.5% Fetal Clone II (FCII, Fisher) for at least 24 h before a sample was collected. It was then mixed with SDS and heated for 5 minutes at 100° C. Each sample was separated by 8 to 25% SDS−PAGE and then transferred to an Immobilon P membrane (Millipore) using the PhastSystem (Applied Biosciences). PHM proteins were visualized using rabbit antibody 246 [rPAM(116−131)][37] diluted 1:1500 and secondary antibody anti-rabbit IgG (Sigma) diluted 1:1000, followed by an AP Conjugate Substrate kit (Bio-Rad Laboratories).

3.1.1.4 PHMcc Expression and Purification

Variant cell lines H242A (kindly provided to us by R. E. Mains and B. A. Eipper) and H107AH108A (constructed in house) were grown as described previously [122][66]. Briefly, the stably transfected cell lines were thawed from a freezer stock in a T75 flask with 20 mL of DMEM/F12 medium containing 10% FCII serum (Fisher). At 80% confluence, the cells were passed into five NUNC triple flasks (500 cm^2 per flask) that were also grown to confluence. Cells were trypsinized and resuspended in 50 mL of medium with 10% FCII serum prior to being inoculated into the extracapillary space (ECS) of a Hollow Fiber Bioreactor (Fibercell Systems 4300-C2008, MWCO of 5000, 3000 cm^2 surface area) precultured first with 2 L of 50 mM PBS (pH 7.35) and then with 2 L of

DMEM/F12 10% FCII serum [122][66][67][143]. Individual bioreactors containing each of the variants were fed with DMEM/F12/10% FCII serum for a month, after which the serum level was reduced to 0.5% FCII serum [132]. At this point, the bioreactors were fed with 0.5% serum-containing medium every other day, and spent medium (20 mL) from the ECS was collected and frozen at −20^{o} C for later purification. After being harvested in the bioreactor for a month (300 mL), each variant was purified as previously described [132].

3.1.1.5 Reconstitution with Copper

Initially, the single-site variants were dialyzed against 20 mM sodium phosphate buffer(pH 8.0) overnight and then reconstituted with up to 2 equivalent of cupric sulfate by slow addition (60 μL/h) followed by exhaustive dialysis. This procedure led to copper:protein ratios close to 1. Thereafter, the single-site mutants were reconstituted with 1.3 equivalent of cupric sulfate, dialyzed overnight against 20 mM sodium phosphate buffer, concentrated using ultrafiltration, and passed through a desalting spin column to remove any remaining unbound cupric ions. The protein concentration was determined by OD_{280} on a Cary 50 UV−vis spectrophotometer at room temperature using an absorbance at 280 nm for a 0.1% solution (1 mg/mL in a 1 cm path length cell) of 0.980 [122]. The copper concentrations were determined using a Perkin-Elmer Optima 2000 DV inductively coupled plasma optical emission spectrometer (ICPOES).

3.1.1.6 Reconstitution with Silver

All silver reconstitutions were conducted in a dark room, with the sample and the silver nitrate stock solutions (100 mM) covered by aluminum foil. Variants were exhaustively dialyzed against MES buffer (50 mM, pH 6.0) overnight, to exchange residual phosphate and chloride ion present in the buffer used for enzyme isolation. The protein was then reconstituted with 1.3 equivalent of a freshly prepared $AgNO_3$ solution, using a syringe pump at a rate of 30 µL/h. The reconstituted protein was gently stirred for 1 h and then passed through two MES buffer-equilibrated desalting columns. The M109I variant was reconstituted with 2.5 equivalent of freshly prepared $AgNO_3$ at a pump rate of 30 µL/h followed by stirring for 1 h, and two cycles of desalting on MES buffer equilibrated spin columns. Protein concentrations were determined as described for copper above. Silver concentrations were determined by ICPOES.

3.1.1.7 Activity Measurements

The enzymatic activities of H107AH108A and H242A were measured by monitoring oxygen consumption in a Rank Brothers oxygen electrode at 37^o C as previously reported [139]. The reaction was performed in a water-jacketed cell at 37^o C. The mixture (2 mL) contained 100 mM MES (pH 5.5), 200 µL of a 6 mg/mL catalase solution (∼50000 units), a 5 µM copper sulfate solution, 10 mM ascorbate, and 80 µM dansyl-YVG substrate. The reaction mixture was allowed to equilibrate for several minutes, after which it was capped and a baseline was measured for 50 s. The reaction was then initiated by adding 10−30 µL of enzyme, through the cap of the reaction vessel with a 50 µL Hamilton syringe. The enzyme concentration for mutants was varied from 100 to 350 µM. Oxygen consumption was monitored and analyzed as previously reported [139][67].

3.1.1.8 Collection and Analysis of EPR Spectra

Quantitative X-band (9.4 GHz) EPR spectra were recorded on a Bruker Elexsys E500 spectrometer equipped with a Bruker ER049X SuperX microwave bridge, and an E27H lock-in detector. Temperature control was provided by a continuous nitrogen flow cryostat system, in which the temperature was monitored with a Bruker W1100321 thermocouple probe. Frozen Cu(II) protein samples at concentrations between 100 and 500 µM in 50 mM MES buffer (pH 5.8, with no cryoprotectant) were measured in 4 mm silica tubes at 90−110 K under non saturating power conditions. EPR spectra were simulated using SIMPIP, developed at the University of Illinois (Urbana,IL) and described in detail elsewhere [144].

3.1.1.9 Sample Preparation for XAS

The oxidized protein samples were prepared in a single step by 5-fold dilution of enzyme at a concentration of 4 mM in Cu(II) with either 50 mM sodium phosphate buffer (pH 7.5) or 50 mM MES and 50mM formic acid (pH 5.5 or 3.5), as necessary. Ethylene glycol was added to a concentration of 20% of the total volume. Reduced protein samples were prepared under anaerobic conditions by 5-fold dilution with pH-adjusted anaerobic buffers to which 5 mM ascorbate had been added along with 20% ethylene glycol. Samples were transferred to XAS cuvettes and flash-frozen in liquid nitrogen. The final concentration of copper or silver varied from 600 to 1200 µM.

3.1.1.10 Collection and Analysis of XAS Data

Samples were measured as aqueous glasses in 20% ethylene glycol at 10 K. Copper K-edge (8.9 keV) and Ag K-edge (25.5 keV) extended X-ray absorption fine structure (EXAFS) and X-ray absorption near edge structure (XANES) data were collected at the Stanford Synchrotron Radiation Lightsource operating at 3 GeV with currents close to 500 mA maintained by continuous top-off.

Cu K-edges were measured on beamline 9-3 using a Si[220] monochromator and a Rh-coated mirror upstream with a 12.5 keV energy cutoff to reject harmonics. Data were collected in fluorescence mode using a high-count rate Canberra 100-element Ge array detector with maximal count rates per array element of <120 kHz. A nickel oxide filter and Soller slit assembly inserted in front of the detector was used to reduce elastic scattering relative to the Cu Kα fluorescence. Four to six scans of a sample containing only buffer were averaged and subtracted from the averaged data for each protein sample to remove the Ni Kβ fluorescence and produce a flat pre-edge baseline.

Ag K-edge data (25.5 keV) were measured on beamline 7.3 using nitrogen-filled ion chambers operating at 1.5 kV. The energy cutoff mirror (used for harmonic rejection) was removed to achieve the high energy, and the Si(220) monochromator was fully tuned to optimize incident counts. While the setup did not provide for harmonic rejection, the level of harmonic contamination at this energy was expected to be low. Energy calibration was achieved with a Ag foil placed between the second and third ionization chambers. The EXAFS was detected by Ag Kα fluorescence using a Canberra 30-element detector with count rates kept below 120 Hz per channel to avoid saturation.

Soller slits and a Pd foil were used to attenuate the elastic scatter peak. Four to six scans of a sample containing only buffer were averaged and subtracted from the averaged data for each protein sample to remove the Pd Kβ fluorescence and produce a flat pre-edge baseline.

Data reduction and background subtractions were performed using the program modules of EXAFSPAK [145]. Output from each detector channel was inspected for glitches and dropouts before inclusion in the final average. Spectral simulation was conducted using EXCURVE version 9.2 [146][147][148] as described previously [66]. Simulations of the EXAFS data used a mixed-shell model consisting of imidazole from histidine residues and S from methionine coordination. The threshold energy, E_0, was set at 8985 eV for Cu and 25520 eV for Ag. Refinement of structural parameters included distances (R), coordination numbers (N), and Debye−Waller factors ($2\sigma^2$) and included multiple scattering contributions from outer-shell atoms of imidazole rings and from linear CO groups.

3.1.1.11 CO Binding

Purified WT PHMcc, H107AH108A, and H242A were concentrated to approximately 4 mM Cu in 20 mM phosphate (pH 8.0). The pH was then adjusted by diluting the concentrated enzyme four times with 50 mM MES/HEPES/CHES/formate mixed buffer at pH 3.5 or 7.5 in a septum-sealed conical vial. Samples were purged under a gentle stream of CO gas for 5 min before the addition of a 5-fold excess (5 mM) of anaerobic buffered ascorbate and then incubated under an atmosphere of pure CO for an additional 5 minutes.

3.1.1.12 Fourier Transform Infrared Spectroscopy

After reaction with CO, protein solutions were loaded into the IR cell (50 µm path length) at a final concentration of 1 mM in copper. After the protein data had been collected, the cell was flushed with buffer and a baseline was recorded. FTIR data were recorded on a Bruker Tensor 27 FTIR spectrometer at room temperature with a sample chamber that was continuously purged with dry CO_2-free air. Samples were equilibrated inside the instrument sample chamber for 15 minutes to allow purging of water vapor and CO_2 prior to data collection. One thousand scans were collected for each sample and buffer spectrum from 2200 to 1950 cm^{-1} at a nominal resolution of 2 cm^{-1}. Baseline subtraction and spectral analysis were performed using the GRAMS AI Spectroscopy Software (Thermo).

3.2 Results

3.2.1 Copper Binding Stoichiometry and Catalytic Activity

Each of the two single-site variants was tested for its capacity to bind copper. Apoproteins were incubated with up to 2 equivalent of cupric sulfate added slowly by syringe pump, followed by exhaustive dialysis or desalting on at least two spin columns. For H242A, the stoichiometry of Cu(II) binding was 1.11 ± 0.03 (average of five measurements), while for H107AH108A, the stoichiometry was 1.09 ± 0.15 (average of six measurements). The catalytic activity of each variant was measured using the standard assay of oxygen uptake on an oxygen sensitive electrode where the slope of the O_2 concentration versus time plot is a direct measure of enzyme activity. Reactants (excluding the enzyme) were incubated together for several minutes prior to initiation by the enzyme. The slope of the oxygen concentration versus time curve did not change after initiation, even at high protein concentrations (up to 350 μM). This is in marked contrast to the case for the WT enzyme, which gives slopes approaching the diffusion limit of oxygen across the electrode membrane at enzyme concentrations of ≤30 μM. We conclude that neither variant has measurable catalytic activity, consistent with the hypothesis that each represents a single-site mutant, where the absence of the second copper atom completely abrogates catalytic activity.

3.2.2 Structural Properties of the Cu(II) Proteins

XAS and EPR spectra were recorded on the oxidized forms of H107AH108A and H242A variants to provide spectroscopic evidence of their formulation as single-site derivatives. Previous EXAFS data for the cupric form of the WT protein were consistent with ligand sets of $(His)_3(OH_2)$ and $(His)_2(OH_2)_2$ for H and M, respectively, where the S(Met) interaction at M is undetectable [55][66]. Also, EXAFS spectra of the oxidized forms of metal site His to Ala mutants such as H107A, H108A,[67] and M314H [139] were found to be extremely similar to those of WT and to each other, because the ligand sets differ by an average of 0.5 His ligand per copper. In the present case, the expectation is that single-site H and M spectra should likewise be similar, a prediction borne out by the nearly identical X-ray absorption near edge structure (XANES) (Figure 3-2 (a)) of the two variants.

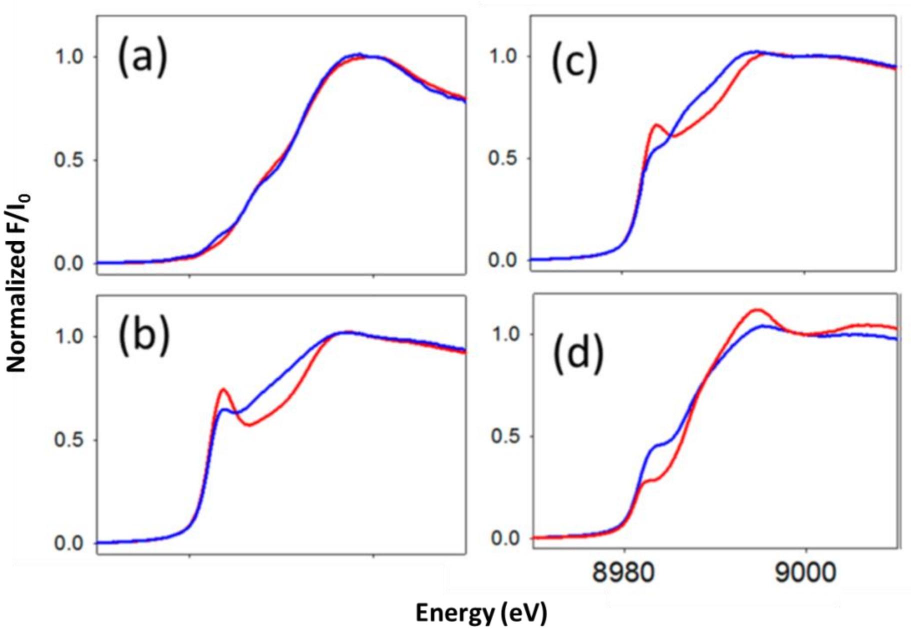

Figure 3-2 *X-ray absorption edge spectra for PHM single-site variants.*
(a) Cu(II) spectra H107AH108A (red), H242A (blue). (b) Cu(I) spectrum of H-site variant H242A at pH 7 (red) and pH 3.5 (blue). (c) Cu(I) spectrum of M-site variant H107AH108A at pH 7 (red) and pH 3.5 (blue). (d) Spectra of Cu(I)−CO complexes of the M-site variant at pH 7 (red) and the H-site variant at pH 3.5 (blue). All edge spectra were normalized at 9000 eV.

Although the H-center should have one more histidine per Cu(II), the overall two-site equatorial coordination is consistently 4N/O. Any EXAFS difference should then be manifest only in the outer-shell signatures of imidazole ligation in the Fourier transforms (FT) around 3 and 4 Å, respectively. Figure 3-3 a compares the FTs of H242A and H107AH108A variants.

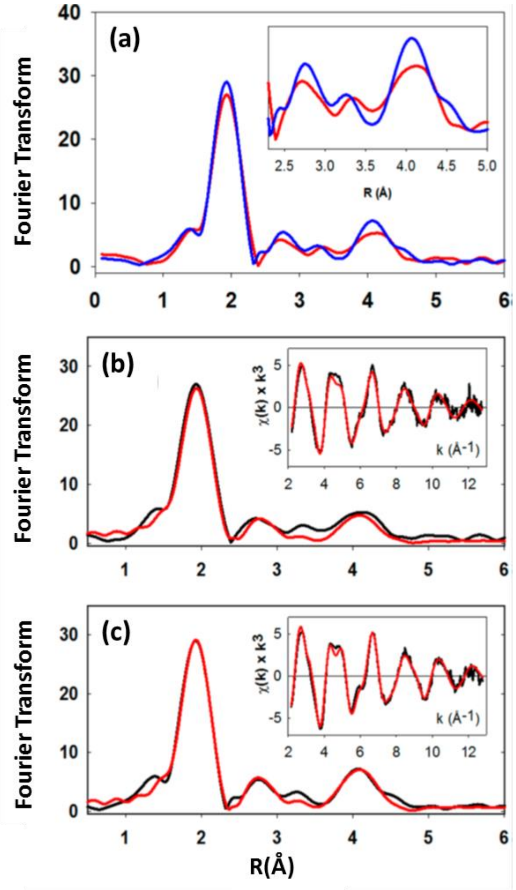

Figure 3-3 *EXAFS spectroscopy of oxidized forms of PHM single-site variants. (a) Comparison of the experimental Fourier transforms of the M-site (H107AH108A, red) and H-site (H242A, blue). The inset shows an expanded view of the 2.5−5 Å region of the FT to indicate the difference in intensity between the M-site (red, two coordinated imidazoles) and the H-site (blue, three coordinated imidazoles). (b and c) Experimental (black) and simulated (red) FTs and EXAFS (insets) for the M-site (H107AH108A) and the H-site (H242A) single-site variants, respectively. Parameters used in these fits are listed in* Table 3-2*.*

In line with prediction, the intensity of the first shell is very similar, while a significant increase in the outer-shell amplitude is observed for the H242A H single site. Panels b and c of Figure 3-3 show simulations of the M-site [2N(His) + 2O(solvent)] and H-site [3N(His) + 1O(solvent)], respectively, with their metrical parameters listed in Table 3-2

		Cu-N(His)[d]			Cu-O/N[e]			Cu-S			
	F[a]	No[b]	R(Å)[c]	DW(Å^2)	No[b]	R(Å)[c]	DW(Å^2)	No[b]	R(Å)[c]	DW(Å^2)	-E0
WT Protein[f]											
oxidized, pH 5.5	0.318	2.5	1.97	0.0123	1.5	1.97	0.0123				4.69
reduced, pH 7.5	0.373	2.5	1.92	0.0175				0.5	2.24	0.0123	0.34
reduced, pH 3.5	0.327	2.5	1.95	0.0182				1.0	2.26	0.0102	-0.66
M-site (H107AH108A)											
oxidized, pH 5.5	0.324	2.0	1.98	0.012	1	1.98	0.012				4.59
reduced, pH 7.5	0.262	2.0	1.91	0.020				1	2.18	0.019	-0.36
reduced, pH 5.5	0.310	2.0	1.94	0.015				1	2.20	0.008	-0.36
reduced, pH 3.5	0.469	2.0	1.99	0.015				1	2.23	0.005	0.62
H-site (H242A)											
oxidized, pH 7.0	0.223	3.0	1.97	0.010	1	1.97	0.10				4.85
reduced, pH 7.5	0.481	2.0	1.89	0.012							2.29
reduced, pH 3.5	0.454	2.0	1.92	0.026				1	2.25	0.007	-0.36

Table 3-2 *Parameters used to Fit the EXAFS Data for Oxidized and Reduced Forms of the M-site (H107AH108A) and H-site (H242A) Single-Site Variants of PHM*

[a] *F is a least-squares fitting parameter defined as* $F^2 = (1/N)\sum_{i=1}^{N} k^6\,(data - model)^2$. [b] *Coordination numbers are generally considered to be accurate to* $\pm 25\%$. [c] *In any one fit, the statistical error in bond lengths is* ± 0.005 Å. *However, when errors due to imperfect background subtraction, phase shift calculations, and noise in the data are compounded, the actual error is close to* ± 0.02 Å. [d] *Fits modeled histidine coordination by an imidazole ring, which included single and multiple scattering contributions from the second-shell (C2/C5) and third shell (C3/C4) atoms, respectively. The Cu-N-C$_x$ angles were as follows: Cu-N-C2, 126^o; Cu-N-C3, -126^o; Cu-N-N4, 163^o; Cu-N-C5, -163^o.* [e] *Distances of the Cu-N(His) and Cu-N/O (non-His) shells were constrained to be equal in fits to the oxidized proteins.* [f] *Data from ref* [67].

The fits were obtained by constraining the Debye−Waller (DW) factors for the outer-shell imidazole atoms to be the same in each fit, while allowing the imidazole occupation number to increase from 2 (M-site) to 3 (H-site). The excellent agreement between theory and experiment for the outer-shell features is convincing evidence of the predicted ligand sets of H and M sites, respectively.

Figure 3-4 compares EPR spectra for the H242A and H107AH108A variants. The spectra show significant differences in the parallel region Figure 3-4 a, while simulations (Table 3-3 and Figure 3-4 b, c) show that the origin of these differences is largely the difference in the value of $g_{\|}$ with the H-site single variant (H242A) having a lower value than the M-site single variant (H107AH108A). This is expected on the basis of Peisach−Blumberg correlations that predict that sites with more N donors have lower values of $g_{\|}$ [149]. The effect of adding together the spectra of the two variants in equal (0.5) proportions and comparing the sum with the spectrum of the WT protein is shown in Figure 3-4 d. The composite spectrum is a reasonable match to that of the WT protein as predicted if the EPR spectra of the individual sites are additive and the sites do not interact.

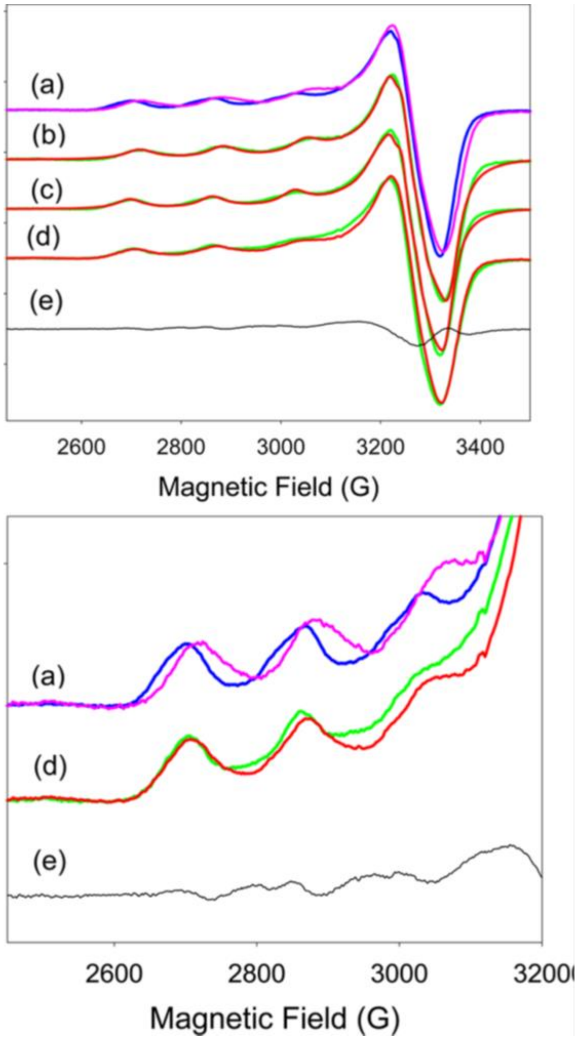

Figure 3-4 *EPR spectra of M-site and H-site single-site variants.*
The top panel shows (a) a comparison of X-band spectra for the M-site (blue) and H-site (pink), (b and c) experimental (green) vs simulated (red) H-site (b) and M-site (c) spectra, (d) a comparison of composite spectra (50% H and 50% M, red) with the WT protein spectrum (green), and (e) the residual after subtracting the composite spectrum from the WT spectrum. EPR collection parameters were as follows: microwave frequency of 9.396 GHz, modulation amplitude of 4 G, microwave power of 2 mW, and temperature of 170 K. The g and A values are listed in Table 3-3. *The bottom panel shows an expanded view of the parallel hyperfine region for spectra a, d, and e.*

	g_x	g_y	g_z	A(x,y)	A(z)	W(x,y)	W(z)
WT, site 1	2.051	2.069	2.300	18	533	49	106
WT, site 2	2.042	2.083	2.279	25	510	49	94
H107AH108A	2.045	2.071	2.280	17	526	53	103
H242A	2.043	2.070	2.263	24	527	55	118

Table 3-3 *Spin Hamiltonian Parameters Deduced from the Simulation of the EPR Spectra of M-site (H107AH108A) and H-site (H242A) Single-Site Variants of PHM*[a]
[a] *Hyperfine values are in MHz.*

The residual after subtraction of the composite spectrum from the WT is shown in Figure 3-4 e, where the lack of any broad underlying signal again suggests that the two sites do not interact or that any interaction cannot be detected at the temperature of the measurement (170 K). On the other hand, the g and A values of the single-site variants correlate less well with the two-site simulation of the WT spectrum reported earlier and included in Table 3-3 for comparison [67]. It is unclear whether this discrepancy relates to inadequacies in the two-site fitting model or to perturbations in the single-site variants relative to the WT protein, but the good correspondence between WT and the 50:50 composite spectrum suggests the former. The bottom panel of Figure 3-4 shows expanded views of the parallel region for the spectra shown in parts a, d, and e of Figure 3-4.

3.2.2.1 Structural Properties of the Cu(I) Centers

The Cu(I) forms of the single-site variants were prepared by ascorbate reduction of their cupric forms. The structures and chemistry of the reduced sites are distinct and offer a more sensitive basis for assessing the fidelity of the single-site variants with respect to the native protein. Previous studies of WT PHM and a variety of H- and M-site variants have provided working assignments for spectral signatures characteristic of the H- and M-site Cu(I) centers. For example, on the basis of EXAFS and FTIR of unligated variants and their CO complexes conducted as a function of pH, Cu_H(I) was predicted to be coordinated to two or three His residues at pH >6 in a configuration that did not bind CO, whereas a conformational switch to a His + S(Met) form was observed at pH <6, which now bound CO with a ν(C≡O) of 2110 cm^{-1}. Cu_M(I) was coordinated by two His residues and a weakly bound S(Met) and bound CO at all pH values with a ν(C≡O) of 2092 cm^{-1}. All of these systems bound copper at both sites [122][67]. Therefore, while the spectral assignments were generally consistent with the available data, the uncertainties introduced by the presence of two chemically inequivalent Cu(I) centers led to ambiguity.

Figure 3-2 b shows X-ray absorption edge data for the reduced H242A (H-site) variant at pH 7.5 (red) and pH 3.5 (blue). The absorption edges show significant differences. At pH 7.5, a relatively intense feature is observed at 8983.7 eV indicative of low-coordinate Cu(I)−bis-imidazole complexes [150][151][152] and suggesting that at neutral pH the H-center binds only two of the three available histidine ligands. Analysis of the EXAFS (Figure 3-5, top panel) confirms this conclusion where the metrical environment simulates to two imidazole ligands with a characteristically short Cu−N (imid) distance of 1.89 Å Table 3-2 [151][150]. These data present the intriguing result that one of the three His ligands is dissociated at neutral pH and imply that a significant conformational change occurs upon reduction. At a low pH (3.5), a different coordination is observed, depicted by a decrease in the 8983 eV intensity (Figure 3-2b, blue trace), and the attenuation of the Cu−N peak and the appearance of a new Cu−S interaction at ∼2.3 Å in the Fourier transform (Figure 3-5, bottom panel). These changes are similar to those reported earlier for the WT enzyme, absent in the M109A variant, and interpreted as a conformational switch induced by a protonation event that allows the non-coordinating M109 to flip into a coordinating position.[67]. The Cu−S and Cu−N distances (Table 3-2) are now typical of three coordination, implying that the Cu(I) retains two His residues, but the Cu−N DW factor has increased, suggesting more disorder in the Cu(I)−histidine diad. The data do not indicate whether the protonating species is a H107 as previously suggested [67], but the following scenario could account for the data. At neutral pH, the WT CuH binds H107 and H108 in a linear configuration with H172 dissociated; when the pH is lowered, H107 is protonated and induces a conformational change to a form involving a triad of H108, H172, and M109.

The DW value derived via simulation of the low-pH data using an N_2S ligand set requires comment. The DW is nearly twice that observed for the low-pH form of the WT protein, where contributions from both the H- and M-centers are averaged. As discussed above, our model for the low-pH transition at the H-center in WT PHM [67] involves protonation of one of the coordinating His residues, and replacement with the S ligand of the nearby M109 residue. Because the H-center single-site variant appears to coordinate only two His residues at neutral pH, it is reasonable to ask whether the high DW reflects the fact that the low-pH form of the H242A variant is two- rather than three-coordinate, resulting from the protonation and replacement of one of these with M109. However, from simulations, neither the goodness of fit nor the values of the bond lengths support a two-coordinate structure, with the Cu−S distance well-defined at its three-coordinate value of 2.25 Å. We may conclude that the high DW must arise from an increased level of disorder in the site, perhaps as a result of multiple species present at equilibrium. One possibility is that the pK_a for the protonation event in the variant may be lower than its WT value (4.6) [139], leading to only partial conversion between the Met-off and Met-on forms. Alternatively, more than one His residue may be protonated, resulting in more complex speciation with fluxional Cu−His coordination. Thus, the ligand dynamics of the low-pH Cu(I)− N_2S site of the H-center [strong Cu−S(Met) with disordered Cu−His coordination] appear to be different from those of the M-center (*vide infra*) where the reverse appears to be true.

XAS data were also collected on the H107AH108A (M-site) variant and are shown in Figure 3-2c (edge data at pH 7.5 and 3.5) and Figure 3-6 (EXAFS data at pH 7.5, 5.5 and 3.5). Absorption edges are generally typical of three-coordinate species. EXAFS analysis (Table 3-2) indicates the presence of two imidazole ligands and one methionine ligand as expected for the His_2Met ligand set with distances typical of this coordination environment. The surprising feature of these spectra is the variation in the intensity of the Cu−S(Met) interaction as the pH is lowered, where the simulations show a significant increase in DW factor with an increase in pH. One explanation of this behavior is that the M-center is comprised of two different conformers, a Met-on form (low pH) and a Met-off for (neutral pH) interconverting via a deprotonation event. The observed distances appear to validate this hypothesis. At neutral pH, both the Cu−N and Cu−S distances are short and suggestive of two-coordination; therefore, it is reasonable to posit that the site is fluxional and interconverts between His-His and His-Met ligand pairs. At low pH, the distances become longer and become more characteristic of three coordination, with a marked decrease in the DW factor of the Cu−S(Met) interaction. We hypothesize that protonation of a non-coordinating residue removes some constraint on the configuration of the three copper-binding residues, allowing them to relax to a more stable conformational state.

The fluxional model predicts that an equivalent fit should be obtained using parameters that represent the average of the two interconverting conformers. We tested this prediction for both neutral and low-pH states using a model that allowed Cu−N and Cu−S shell occupancies to vary while keeping the overall coordination number fixed at 2. At pH 7, an adequate fit (F = 0.38 vs 0.26) could be obtained with 1.45 Cu−N(His) and 0.55 Cu−S(Met) at the same distances but with lower DW factors (Figure 3-7, top panel). At low pH, however, simple averaging resulted in poorer simulations, but introduction of a sub stoichiometric Cu−N interaction at 1.87 Å led to a much improved fit (0.28 vs 0.47), particularly with respect to the low-*R* shoulder in Figure 3-6 (bottom panel) and with more reasonable DW factors of the Cu−N shells (Figure 3-7, bottom panel). This may suggest the presence of both two-coordinate and three-coordinate conformers existing in equilibrium at low pH arising from more complex ligand dynamics.

Examination of the crystal structure suggests a plausible explanation for this behavior. The distance between the main chain amide N of the M-coordinating H244 and one of the carboxylate oxygens of E313 is 2.78 Å, which is in the range expected for a H-bond between these residues. E313 is part of the fully conserved $E^{313}M^{314}C^{315}$ triad. We note that protonation of the carboxylate side chain of E313 would sever this H-bond and remove the constraint on the position and conformation of H244 as well any constraint on E313's neighbor, the M314 copper ligand. The pH dependence of M site S(met) coordination was not detected in our previous pH dependent study of the WT protein [139], largely because it was obscured by or averaged into the pH-dependent conformational switch at the H-center, and it is therefore unclear whether the M-site undergoes the same pH dependent change in the WT protein.

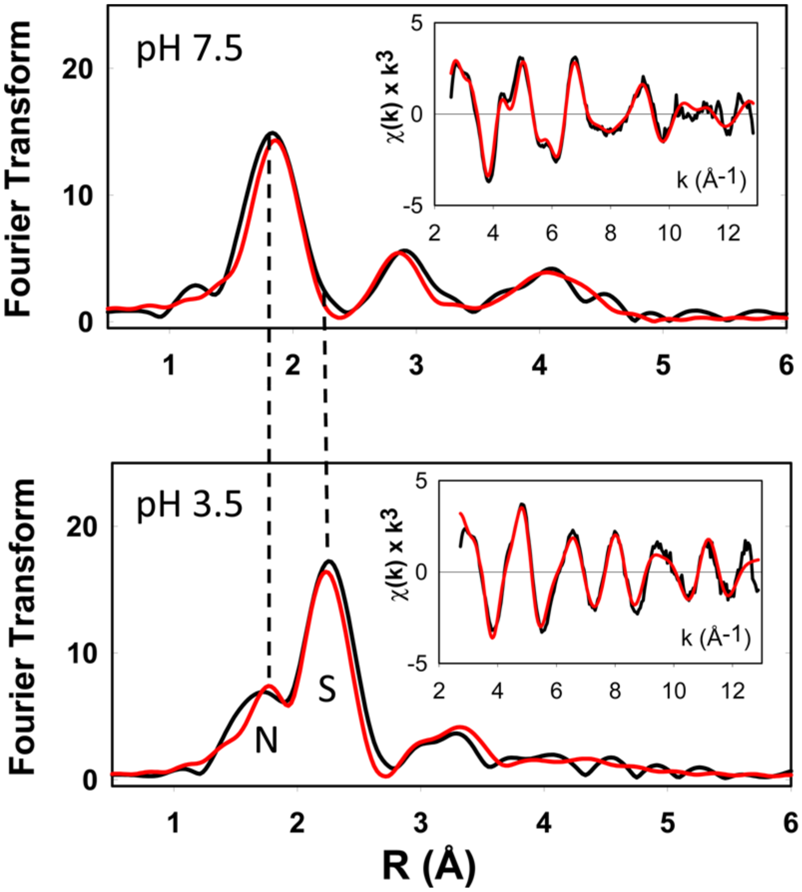

Figure 3-5 *Experimental and simulated Fourier transforms and EXAFS for Cu(I) form of single-site mutants.*

The (inset) graph is the EXAFS for reduced Cu(I) forms of the H-site variant (H242A) at pH 7.5 (top) and pH 3.5 (bottom). Parameters used in fits are listed in Table 3-2.

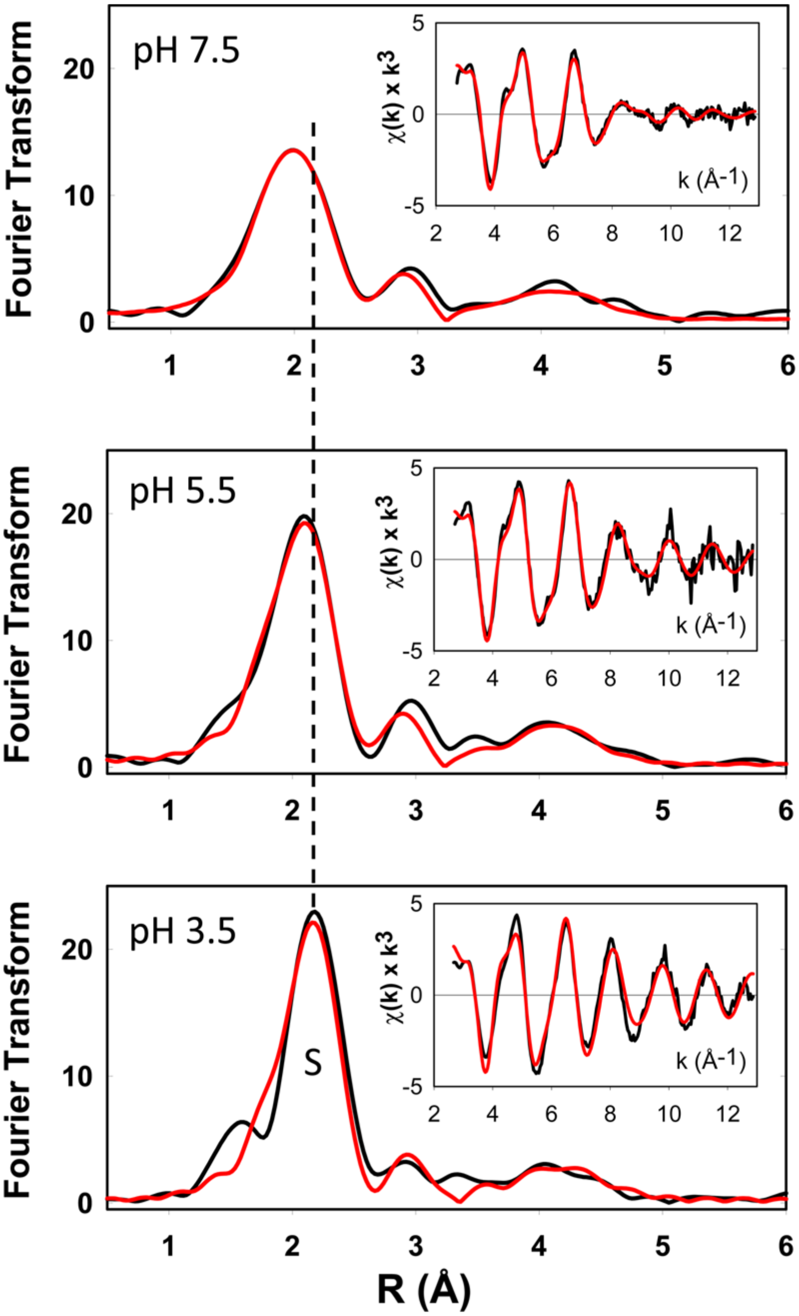

Figure 3-6 *Experimental and simulated Fourier transforms and EXAFS. The (insets) graph is the EXAFS for reduced Cu(I) forms of the M-site variant (H107AH108A) at pH 7.5 (top), 5.5 (middle), and 3.5 (bottom).Parameters used in the fits are listed in* Table 3-2*.*

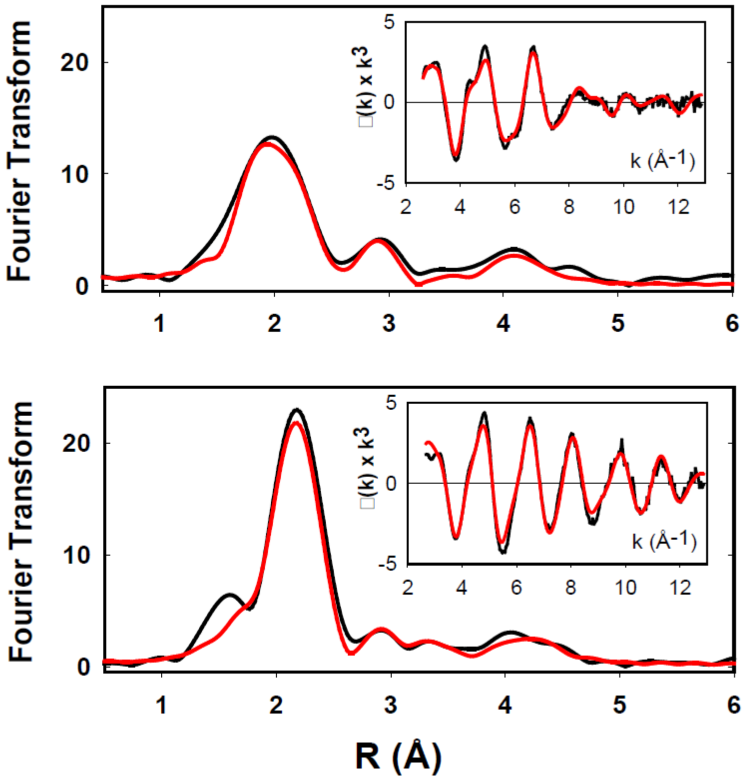

Figure 3-7 *Alternate fits to the EXAFS of the reduced Cu(I) forms of the M-site single-site variant H107AH108A.*
Top panel, pH 7 data fit to the average of the two fluxional forms with Cu-ligand distances (DW) 1.5 Cu-N(His) at 1.92 Å (DW, 0.009) and 0.5 Cu-S(Met) at 2.19 (DW, 0.007). The fit index was 0.381. Bottom panel, pH 3.5 data fit to two different conformations (a) 0.6 Cu- N(His) at 1.87 Å (DW, 0.010) corresponding to a 2-coordinate conformer, and (b) 1Cu-N(His) at 2.01 (DW, 0.002) +1 Cu-S(Met) at 2.24 (DW, 0.004). The fit index was 0.281.

3.2.2.2 CO Complexes

We also investigated the CO binding properties of both single-site variants as a function of pH, using FTIR and XAS. Panels a and b of Figure 3-8 compare the FTIR in the 2200−1950 cm^{-1} region for the CO complexes of H242A (H-site) at pH 7.5 and 3.5. On the basis of previous assignments derived from measurements of the WT and M109A derivatives, an H-site single-site variant is predicted to bind no CO at neutral pH but forms a CO complex at low pH where the S donor atom from M109 enters the coordination sphere [67]. In line with these predictions, no ν(CO) is observed at pH 7.5, whereas a rather weak band centered at 2102 cm^{-1} is found at pH 3.5, blue-shifted relative to that of the WT protein by ~8 cm^{-1}. The carbon−oxygen stretching frequency of Cu(I)−carbonyl complexes is a sensitive index of coordination and/or ligand conformation. ν(C≡O) is a measure of the C−O bond order, which is modulated by the degree of backbonding from the filled d shell of Cu(I) into the empty π-antibonding orbitals on CO, and is further influenced by the donor power of the other ligands to Cu(I). These trends are illustrated by the frequency of carbonmonoxy hemocyanin [$Cu(His)_3$, 2043−2063 cm^{-1}] relative to PHM and DBM [$Cu(His)_2(Met)$, 2089−2093 cm^{-1}], where substitution of the stronger histidine donor for the weaker thioether results in less back-bonding and a higher frequency for PHM/DBM.[122][55][59]. However, CO frequencies are also highly sensitive to metal site electronic structure, conformational state, and site polarity. In *Thermus thermophilus*, ν(C≡O) for the Cu_B−CO photoproduct of the *caa₃* oxidase is 10 cm^{-1} higher than that of the *ba₃* Cu_B−CO photoproduct, even though the ligand set consists of three His residues in both cases [153][154], which indicates at least two conformations in the Fe_{a3}−Cu_B active site cavity [155]. PHM and DBM likewise share identical ligand sets at CuM, but their ν(C≡O) values differ by 3 cm^{-1}; CO frequencies of hemocyanins from different species vary between 2043 and 2063 cm^{-1}

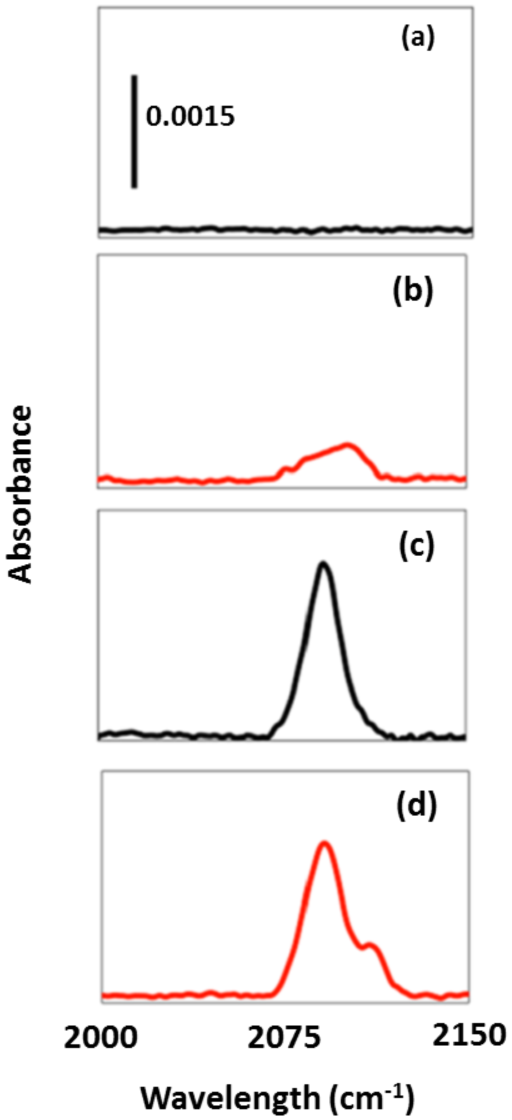

Figure 3-8 *FTIR spectra of single-site Cu(I)−CO complexes: (a) H-site CO at pH 7.5, (b) H-site CO at pH 3.5, (c) M-site CO at pH 7.5, and (d) M-site CO at pH 3.5.*

The 8 cm^{-1} shift in ν(CO) for the H242A variant is therefore not inconsistent with the $Cu(His)_2S(Met)CO$ coordination proposed for the low-pH CO complex of the H center in the WT protein, but the His-Met donor power, ligand conformation, or the site polarity must be different in the H single-site variant. It is also unclear why the intensity of the low pH band is so much lower than that of the WT protein.

Panels c and d of Figure 3-8 compare the CO complexes of theH107AH108A (M-site) variant at pH 7.5 and 3.5. Both spectra show the intense 2092 cm^{-1} band previously assigned to the M-site carbonyl. These data provide an unambiguous assignment of the origin of this IR band. The arguments in the preceding paragraph relating small changes in ν(C≡O) to conformational variation among complexes of the same ligand set have a converse, namely, that invariant frequencies are indicators of highly similar coordination and conformation. The invariant ν(C≡O) of WT and H107AH108A carbonyls therefore establishes that the ligand set and conformation of the carbonyl are identical in WT and the M single-site variant. The low-pH spectrum also shows a small shoulder at 2111 cm^{-1}. This feature could be due to a small component of a different conformation because bands at a similar frequency (with a much higher intensity) were observed previously for a low-pH H-site CO complex of the WT enzyme, which was shown to have a similar ligand set due to low-pH-induced flipping of M109 (*vide supra*) [67]. However, the structural differences between conformers and the factors that control their distribution are unknown at this time.

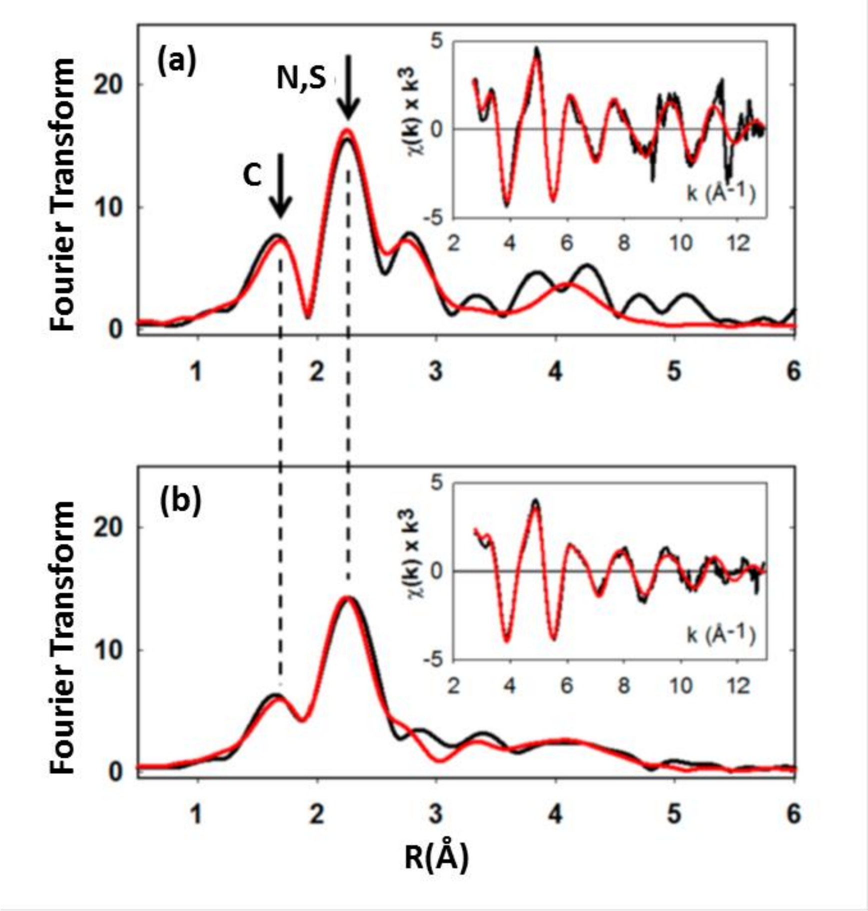

Figure 3-9 *Experimental and simulated Fourier transforms and EXAFS*
The (insets) graphs for reduced Cu(I) forms of the single-site Cu(I)−CO complexes: (a) M-site CO at pH 7.5 and (b) H-site CO at pH 3.5. Parameters used are listed in Table 3-4*.*

XAS was used to compare the structures of the H- and M-site carbonyls as shown in Figure 3-2 d (XANES) and Figure 3-9 a, b (EXAFS). Metrical parameters, including those of the coordinated CO derived from multiple scattering analysis, are listed in Table 3-4. The two carbonyls appear to be extremely similar with Cu−C and Cu−O distances of 1.80 and 2.85 Å and Cu−C−O angles of 171^{o} and 179^{o} for the H- and M-site complexes, respectively. From these values (and assuming errors in bond lengths of ±0.02 Å and angles of ±10^o), the C−O bond distances calculate out as 1.05 ± 0.08 Å, which is consistent with the expected C−O distance of a coordinated carbonyl of ~1.1 Å.

			Cu-N(His)[d]			$\mathbf{Cu{-}C \equiv O}$[e]			Cu-S			
	N(CO) (cm^{-1})	**F[a]**	**No[b]**	**R(Å)[c]**	**DW(Å^2)**	**No[b]**	**R(Å)[c]**	**DW(Å^2)**	**No[b]**	**R(Å)[c]**	**DW(Å^2)**	**-E$_0$**
M-site (H107AH108A)												
pH 7.5	2092	0.74	2	1.97	0.023	1C	1.80	0.006	1	2.26	0.007	-0.92
						1O	2.85	0.024				
$\angle \mathbf{Cu - C - O = 179^o}$												
pH 3.5	2092	Not determined										
H-site (H242A)												
pH 7.5	none											
pH 3.5	2102	0.32	2	1.98	0.020	1C	1.81	0.009	1	2.27	0.009	-0.97
						1O	2.85	0.021				
$\angle \mathbf{Cu - C - O = 170^o}$												

Table 3-4 *FTIR Frequencies and EXAFS Fitting Parameters for the CO Complexes of M-site (H107AH108A) and H-site (H242A) Single-Site Variants of PHM*

[a] *F is a least-squares fitting parameter defined as* $F^2 = (1/N)\sum_{i=1}^{N} k^6\,(data - model)^2$. [b] *Coordination numbers are generally considered to be accurate to* $\pm 25\%$. [c] *In any one fit, the statistical error in bond lengths is* ± 0.005 Å. *However, when errors due to imperfect background subtraction, phase shift calculations, and noise in the data are compounded, the actual error is close to* ± 0.02 Å. [d] *Fits modeled histidine coordination by an imidazole ring, which included single and multiple scattering contributions from the second-shell (C2/C5) and third shell (C3/C4) atoms, respectively. The Cu-N-C$_x$ angles were as follows: Cu-N-C2, 126^o; Cu-N-C3, -126^o; Cu-N-N4, 163^o; Cu-N-C5, -163^o.* [e] *Metrical parameters for the CO ligand were simulated using full multiple scattering treatment. Cu-C and Cu-O distances and Cu-C-O angles were allowed to float in the fits.*

Other details of the complexes reveal essentially identical ligand sets of two His residues, one S, and one CO, all with comparable and chemically reasonable distances and Debye−Waller factors. These structures are consistent with our predictions based on previous studies of the WT and its CO complexes. However, the M-site CO EXAFS data measured at pH 7.5 are of further interest because they establish that the Met ligand is fully coordinated to Cu(I) in the carbonyl (fully Met-on), even though M314 exists in Met-on and Met-off conformations in the unligated M-site at neutral pH. In this regard, the M-site CO structure corresponds to the Met-on conformation of the unligated M-site at pH 3.5, suggesting that CO binding provides a greater driving force than H-bonding (*vide supra*) in M-site conformational organization. This observation also rationalizes the invariant 2092 cm^{-1} frequency of the M−CO complex over the full pH range.

3.2.2.3 Silver Binding

We used single-site mutant H107AH108A to test whether other metals such as Ag(I) could bind at the M-site. When the M-site variant was reacted with an excess (1.3) of molar equivalents of silver nitrate in MES buffer (pH 6.0), followed by two rounds of desalting on MES buffer equilibrated spin columns, the protein bound 1.06 ± 0.15 Ag(I) per protein, indicating tight binding of silver. This result was then used to examine whether the WT protein would similarly bind silver and whether the binding was selective for the M-site. Ag(I) is electronically homologous to Cu(I) and in general shows similar coordination chemistry [156], although Ag is expected to have a higher affinity for ligand sets with S donors. Therefore, we used the M109I variant of the WT protein to control against M109 flipping that occurs at low pH and could influence Ag(I) binding at the H-center. The M109I variant (containing intact M- and H-sites) was incubated with 2.3 equivalents of silver nitrate followed by two desalting steps and the silver content measured by ICPOES. The protein was found to bind 0.84 ± 0.11 Ag(I) per protein. Taken together, the results of these experiments imply that Ag(I) binds selectively at the M-site and has little or no affinity for the H-site. [Note that the analogous experiment of reacting Ag(I) with the H-site variant H242A was deemed unreliable as deletion of a single histidine may not be sufficient to abrogate binding of silver to the remaining His and Met at the M-site.]

The ligand environments of the silver complexes of H107AH108A and M109I were investigated by EXAFS measurements at the silver absorption edge. The high energy of the Ag K-edge makes these experiments challenging because of the low intensity and beam heterogeneity at the large monochromator angles necessary to reach the required energy (25.5 keV). These factors restricted the usable *k* range of the data to ≤11 $Å^{-1}$. EXAFS data for the M109I variant are shown in Figure 3-10. Simulation of the data requires the presence of both Ag−N and Ag−S components, but because both components have very similar phases, they are correlated given the restricted data range in *k* space. Notwithstanding, a good fit was obtained with one Ag−N(His) component at 2.2 Å and one Ag−S component at 2.5 Å, although alternatives of similar quality could be obtained varying the N- and S-shell occupancies but keeping their sum equal to 2. These results are similar to those obtained for the Cu(I) complex of

H107AH108A at neutral pH and validate the conclusion that silver binds exclusively at the M-center. EXAFS data for the Ag(I) complex of H107AH108A were of poorer quality (data not shown) but could be simulated by a N + S ligand set. However, the poorer data coupled to the correlation discussed above led to large uncertainties in both distances and coordination numbers, and the simulations are considered unreliable.

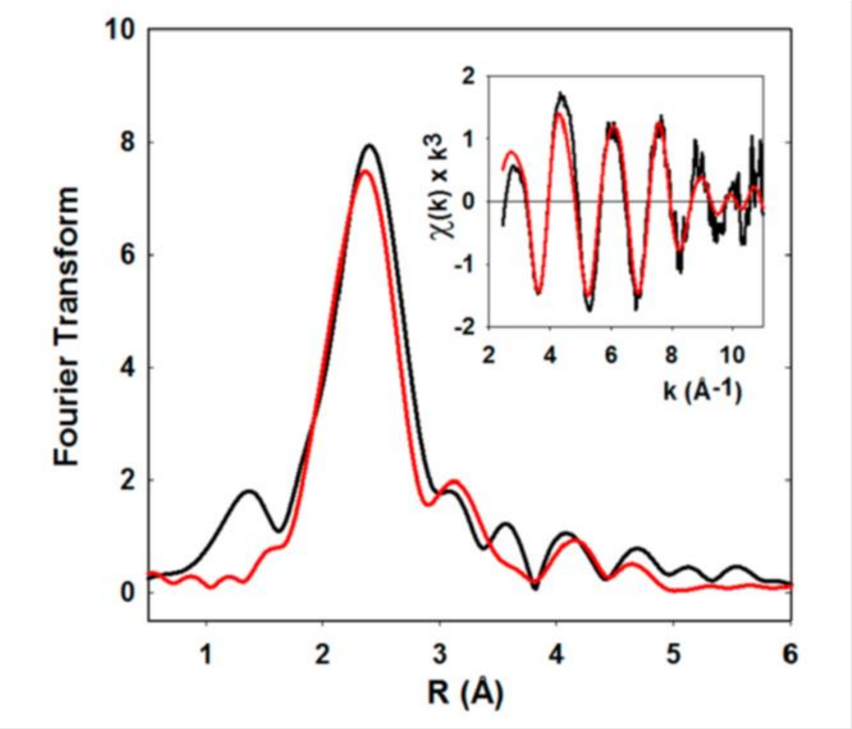

Figure 3-10 *Experimental and simulated Fourier transform and EXAFS*
The graph (inset) for the 1:1 Ag(I) complex of the M109I derivative of WT PHM. Data were collected at the Ag K-edge (25515 eV) and simulated with one Ag−N(His) component at 2.18 Å and one Ag−S component at 2.47 Å. Calculations included multiple scattering contributions from the histidine ligand using geometric parameters as listed for the copper EXAFS spectra in Table 3-2*.*

3.2.3 Discussion

We prepared and characterized two variants of PHM that contained mutations in the metal binding ligands at each of the two Cu sites. These derivatives bind only a single copper atom, suggesting that they indeed correspond to enzyme states with each of the two copper sites singly occupied. The variants are completely devoid of catalytic activity, emphasizing the obligatory requirement for both copper centers in the catalytic mechanism. The H242A variant contains copper only in the H-site, while the H107AH108A variant contains copper only in the M-site. Detailed spectroscopic studies of the Cu(II) and Cu(I) forms of these derivatives provide robust assignments for spectral features previously observed in the WT protein. In particular, the unique chemistry of the M-site, which includes its $His_2S(Met)$ ligation, and reactivity toward CO generating a carbonyl complex with $\nu(CO)=2092\ cm^{-1}$ are faithfully reproduced in the H107AH108A variant. Likewise, the low-pH conformational switch described previously for the H-site[67] is also observed in the H242A variant. However, the study also uncovers new structural elements of both sites in the cuprous forms, which were previously obscured by spectral overlap between the two inequivalent coppers of the WT protein. For example, the H-site coordinates only two of its three His ligands in the Cu(I) state, while the M-site appears to undergo interesting pH-dependent conformational dynamics between Met-on (low-pH) and Met-off (neutral pH) forms. These new observations provide unique and critical insight into the catalytic roles of each copper center.

Ag(I) is iso-electronic with Cu(I) and has been shown to be handled by similar cellular transport processes [157]. Although complexes of Ag in the Ag(III) state exists, the instability of the Ag(II) state renders the metal unsuitable for a functional substitute for copper in enzymes such as PHM and DBM. However, substitution of one of the metal centers with Ag(I) would create heterobimetallic complexes in which the spectroscopy of the two centers does not overlap, allowing the structural elements of each site to be studied independently. Such studies would be a useful adjunct to single-site variants, as the effect of M-site metal occupancy on the structure of the H site (and vice versa) could be distinguished. With this in mind, we used the H107AH108A variant to find conditions under which the Ag(I) ion could be incorporated at the PHM center and followed up with studies of Ag(I) with a WT analogue that showed that Ag(I) bound selectively at the M-center to generate a complex that gave structural (EXAFS) parameters similar to those of the Cu(I) complex. These data open the door to further investigations of the individual chemistry and spectroscopy of the metal centers in PHM. Although more challenging, the preparation of Ag/Cu heterobimetallic complexes is underway, and their detailed analysis will be the subject of future studies from this laboratory.

CHAPTER 4. STOPPED-FLOW STUDIES OF THE REDUCTION OF THE COPPER CENTERS SUGGEST A BIFURCATED ELECTRON TRANSFER PATHWAY IN PEPTIDYLGLYCINE MONOOXYGENASE.[2]

4.1 Introduction

Amidation is a post-translational modification required for the bioactivation of glycine-extended pro-peptides [31][52][133], which are components of essential signaling pathways.[136][158][159]. The reaction is catalyzed by the bifunctional enzyme peptidylglycine α-amidating monooxygenase (PAM) and involves addition of an amide group to the C-terminus of a glycine extended pro-peptide substrate[159][37]. Amidation proceeds in two sequential steps each catalyzed by individual domains of the PAM enzyme: hydroxylation, catalyzed by the copper-containing peptidylglycine α-hydroxylating monooxygenase (PHM) and dealkylation of the carbinolamide intermediate catalyzed by the Ca/Zn containing peptidylglycine α-amidating lyase (PAL)[40] [41]. Specifically, the PHM domain mediates the stereospecific hydroxylation of the terminal glycine of the peptide substrate to form a peptidyl-α-hydroxyglycine intermediate that undergoes N-C bond fission and elimination of glyoxalate to yield the α-amidated product [10][11][12]. (Figure 4-1)

---

[2] This chapter has been published in a similar form in *Biochemistry,* 2016, 55, 2008-2021.

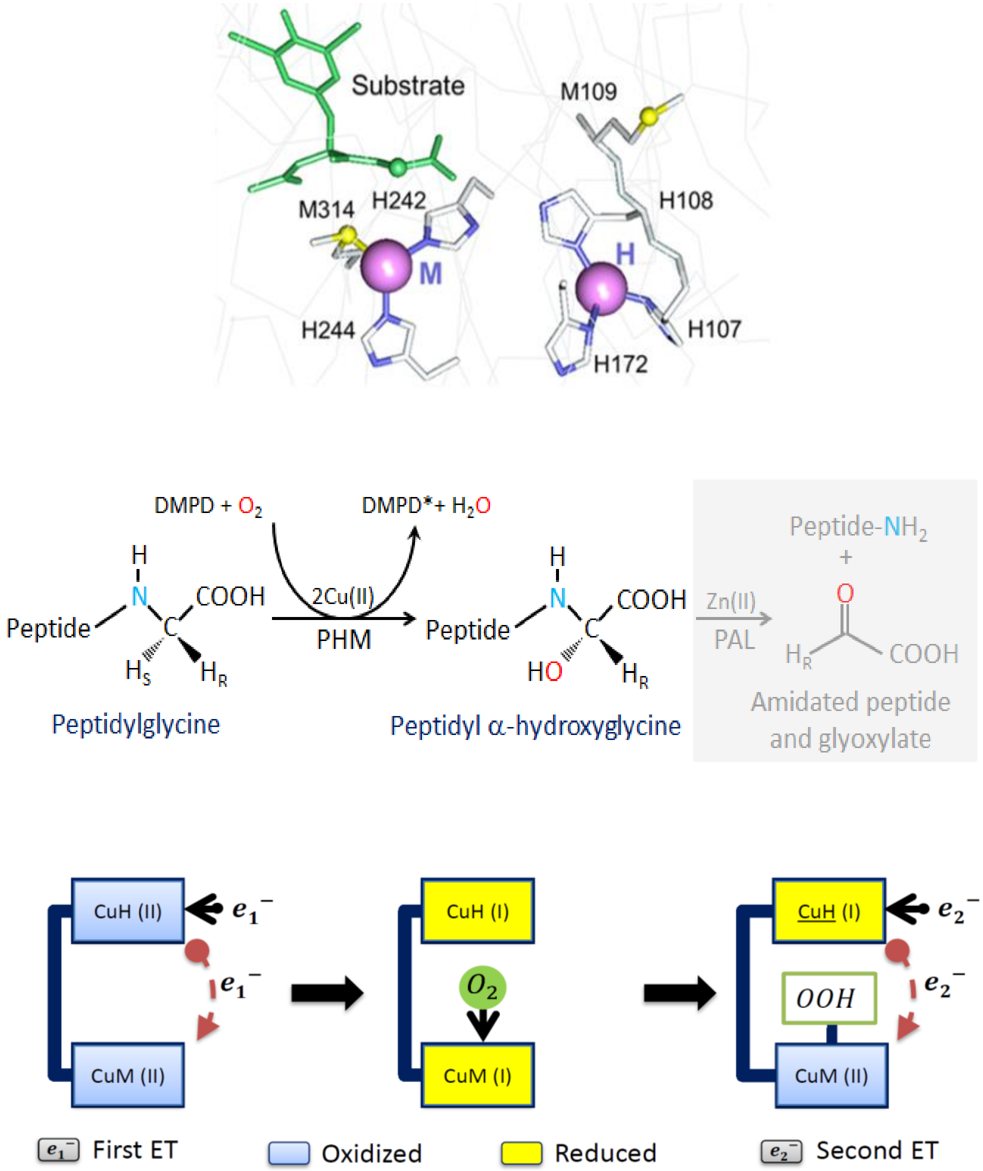

Figure 4-1 *Active site structure (top) of PHM showing the M center (left) and H center (right), with the substrate colored green, binding close to M. Taken from PDB entry 1OPM. Reaction (middle) catalyzed by PAM, showing the PHM-catalyzed hydroxylation of the C-terminal Glycine residue in bold and the PAL-catalyzed N-dealkylation shaded. Reductive and oxidative (catalytic) phases (bottom) of the reaction cycle.*

PHM belongs to the family of type 2 copper containing monoxygenases, which also includes its homologues, dopamine β-monoxygenase (DBM) [160] and tyramine βmonooxygense (TBM).[140][161]. PHM is a di-copper containing enzyme [55][62] composed of two domains [63], with each domain housing a copper center, separated by an 11 Å water-filled cleft .[35][125][133]. The copper centers, termed CuH and CuM are functionally inequivalent and differ in geometry as well as the set of ligands .[54][66]. The CuH site is ligated to Nδ of three histidines (H107, H108 and H172), whereas the CuM site is bound by the Nε of two histidines (H242, H244) and the sulfur of methionine (M314). [35][125][133]. The CuM site serves as the oxygen binding and catalytic site and a pre-catalytic dioxygen-bound state has been described by crystallography [69]. The CuH site is believed to be involved in electron transfer (ET) [46] [45][126][127].

During each catalytic turnover event, the Cu(II)H and Cu(II)M sites of the enzyme are reduced by the physiological reductant ascorbate to form Cu(I)H and Cu(I)M. [39][38][15]. This is the active state of the enzyme, which reacts via equilibrium-ordered binding of first peptide substrate and then dioxygen to form an $E \bullet S \bullet O_2$ ternary complex.[49][44]. The committed step in the enzyme reaction mechanism involves abstraction of an electron from the M-site to form a superoxo intermediate [$Cu(II)M\text{-}O_2^-$] [46][45][126][47][48], which is most likely bound end-on and protonated [162]. This is sufficiently electrophilic to abstract a *pro-S* hydrogen atom from the substrate by a hydrogen tunneling mechanism [49][50] thereby forming peroxide and a substrate radical. Hydroxylation is believed to be accomplished by peroxide O-O bond cleavage and radical rebound to the substrate radical in a step of low activation energy, which also includes the transfer of a second electron from CuH to CuM.

Among many aspects of PHM chemistry that remain elusive, the ET from H-site to the M-site is one of the most challenging. The two electrons required for substrate hydroxylation are delivered to the catalytic M-site at different stages of the reaction cycle. The first electron reduces the Cu(II)M species to the Cu(I)M state in a step we call the “reductive” ET phase prior to binding of dioxygen at M. The second electron is transferred in a step we call the oxidative or “catalytic” ET phase after the enzyme has committed to catalysis, and is generally believed to reduce a high-valent species such as Cu(III)=O or Cu(II)-O• formed after the O-O bond has broken. It has been proposed [45] that the spatial separation between the two coppers prevents fast ET from the CuH center, thereby amplifying the reactivity of the CuM-superoxo species, but the enzyme pays an energetic price for the increased oxygen reactivity by necessitating long range electron transfer from CuH to CuM. Although the intersite distance is consistent with fast ET [103], the open access of solvent to both copper centers, and the large coordination changes that accompany reduction to Cu(I) [66] have raised intriguing questions about how the enzyme avoids the associated unfavorable reorganizational energies. A number of proposals for the catalytic ET step have been advanced. These have included superoxide channeling [122]; a “substrate-mediated” pathway involving H108, Q170, a water molecule, and the peptide substrate; direct interaction of the Cu(I)H with the substrate radical via domain movement [123]; and transfer across the intersite cavity via an ordered array of water molecules, perhaps assisted by Y79. [126] [127] [128]. However, these mechanisms do not account for all of the available data. For example, the superoxide channeling theory predicts superoxide leakage, but none has been detected; instead the reduction of oxygen and substrate hydroxylation remained completely coupled even in the presence of slow substrates and variants of low catalytic activity [126] [141] [67]. Similarly, mutation of the critical substrate-mediated pathway residue Q170 has only limited effects on the steady state kinetics. [163]. Thus, none of these theories are able to fully explain all aspects of the ET.

In an effort to investigate further the important elements of the ET process, we have used stopped-flow spectrophotometry to measure the rates of reduction of the H- and M-sites in the oxidized state of the WT enzyme and important semi-functional variants. Cyclic voltammetry studies have also been undertaken in a bid to understand the significance of the reduction potential of the copper centers in defining their individual roles. Our results show that the reductive event is biphasic, with a fast step followed by a much slower one. The binding of substrates (Ac-YVG, hippuric acid and nitrohippuric acid) leads to a dramatic acceleration of the slow reductive step, associated with an increase in the reduction potential of one of the copper centers. Studies of the single-site mutants H107AH108A (M-site occupied, H-site empty) and H242A (H-site occupied, M-site empty) [68] have allowed assignment of fast and slow rates of reduction to the H- and M-site respectively. The role of the histidine ligands of the H-site was investigated by performing reduction kinetics on mutants in which each histidine was mutated to alanine (H107A, H108A, and H172A). The results suggested that H108 is the most important component of the reductive ET pathway, implying that it may serve as a unique conduit for H to M electron transfer. On the other hand, despite its profound effect on the rate of H-atom abstraction [141], H172 appeared to be unimportant for reductive ET. These data have led to the conclusion that the pathways for reductive and oxidative ET may be bifurcated, with the reductive electron following a path different from that of oxidative electron. Implications for the enzymatic mechanism are discussed.

4.2 Materials and Methods

Buffers, ascorbate, N, N-dimethyl-p-phenylenediamine dihydrochloride (DMPD) were obtained from Sigma-Aldrich at a minimum purity of 99%. The substrate Ac-Tyr-Val-Gly (Ac-YVG) was purchased from Peptide International. Hippuric acid and nitrohippuric acid were purchased from Sigma-Aldrich.

4.2.1 Construction of Variants

WT PHM catalytic core (PHMcc, residues 42-356) and its variants H107A, H172A and H242A were constructed as described previously [62]. For H108A and H107H108A, constructs carrying the mutations were individually introduced into pBS.ΔProPHM382s (obtained as a gift from Betty A. Eipper and Richard E. Mains) using Splicing by Overlap Extension (SOEing) also as described previously [68]. CHO DG44 cells were transfected with the recombinant DNA using Lipofectamine 2000 (Invitrogen). The transfected cells were subsequently selected for *Dhfr* cell lines in α-minimum Eagle's medium (MEM) containing 10% dialyzed fetal bovine serum. Only those cells that retained the *Dhfr* gene (co-located with PHM on the plasmid) were capable of growth under these conditions. Monoclonal cell lines were created by serial dilution into 96-well plates to select for wells which contained single cell colonies. These were passed individually into a fresh 96-well plate, grown to confluence, and screened via Western blot for PHMcc production under similar conditions. The strongest producers were inoculated into a Hollow Fiber Bioreactor with a molecular weight cutoff (MWCO) of 5 kDa (Fibercell Systems, Inc.).

4.2.2 Western Blot Analysis

CHO DG44 cells were incubated in DMEM/F12 media containing 0.5% Fetal Clone II (FCII, Fisher) for at least 24 h before a sample was collected. The sample was mixed with SDS and heated for 5 minutes at 100^{o} C. Each sample was separated on an 8 to 25% SDS-PAGE gel and then transferred to an Immobilon P membrane (Millipore) using the PhastSystem (Applied Biosciences). PHM proteins were visualized using rabbit antibody 246 [rPAM (116-131)] [37] diluted 1:1500, and secondary antibody anti-rabbit IgG (Sigma) diluted 1:1000, followed by an AP Conjugate Substrate Kit (Bio-Rad Laboratories).

4.2.3 PHM Expression and Purification

The stably transfected cell lines were thawed from freezer stock into a T75 flask with 20 mL of DMEM/F12 medium containing 10% FCII serum (Fisher). At 80% confluence, the cells were passed into five NUNC triple flasks (500 cm^2 per flask) which were also grown to confluence. The cells were trypsinized and resuspended in 50 mL of DMEM/F12 medium with 10% FCII serum prior to inoculation into the extra-capillary space (ECS) of a Hollow Fiber Bioreactor (Fibercell Systems 4300-C2008, MWCO 5 kDa, surface area of 3000 cm^2) precultured with 2 L of 50 mM PBS (pH 7.35) and 2 L of DMEM/F12 10% FCII serum [66][122][143]. Individual bioreactors containing each of the variants were fed with DMEM/F12/10% FCII serum for a month. The serum level was then reduced to

0.5%, at which point spent medium (20 mL) from the ECS was collected every other day and frozen at -20° C for purification later. Approximately a month's worth of the bioreactor harvest (300 mL) for each variant was purified as previously described [66][122][143].

4.2.4 PHM Copper Reconstitution.

For WT PHM, H107A, H108A and H172A, purified enzyme was dialyzed against 20 mM sodium phosphate buffer (pH 8.0) and then reconstituted with 2.5 molar equivalents of cupric sulfate per protein, followed by two cycles of dialysis to remove unbound cupric ions. For the single-site variants (H107H108A and H242A), the purified protein was initially dialyzed against 20 mM sodium phosphate buffer (pH 8.0) overnight, reconstituted with 2.5 equivalents of cupric sulfate using a syringe pump, at a rate of 60 ul/hr, and dialyzed exhaustively against copper-free phosphate buffer at the same pH and ionic strength. This procedure resulted in copper:protein ratios close to 1. Thereafter, the single-site mutants were reconstituted with 1.3 equivalents of cupric sulfate, and dialyzed overnight against 20 mM sodium phosphate buffer(pH 8).The protein concentration was determined by OD_{280} on a Cary-50 UV-vis spectrophotometer at room temperature using an extinction coefficient for a 1% solution at 280 nm of 0.980. The copper concentrations were determined using a Perkin-Elmer Optima 2000 DV inductively coupled plasma optical emission spectrometer (ICP-OES).

4.2.5 Specific Activity Measurements

The enzymatic activity was measured by monitoring oxygen consumption in a Rank Brothers Oxygen Electrode at 37° C as previously reported [66][122][67][68][143]. The reaction was performed in a water-jacketed cell maintained at 37^{o} C. The mixture (2 mL) contained 100 mM MES (pH 5.5), 200 µL of 6 mg/mL catalase solution (47,000 units/mg), 5 µM cupric sulfate, 10 mM ascorbate and 80 µM dansyl-YVG substrate. The reaction mixture was allowed to equilibrate for 1 minute, after which it was capped and a baseline was measured for 50 s. The reaction was then initiated by adding 10 – 50 µL of enzyme (depending on the mutant) through the cap of the reaction vessel with a 50 µL Hamilton syringe. The enzyme concentration for mutants was varied from 100 µM to 350 µM.

4.2.6 X-ray Absorption Spectroscopy

Oxidized samples were prepared in a single step by 5-fold dilution of 2mM protein in 50 mM MES (pH 5.5) [4 mM in Cu(II)] with the appropriate mixed buffer containing 20% ethylene glycol. Reduced protein samples were prepared under anaerobic conditions by 5-fold dilutions of 2 mM protein [4 mM in Cu(II)] samples of the oxidized enzyme with the appropriate buffer containing 5 mM ascorbate and 20% ethylene glycol. Samples were transferred to an XAS cuvette via a syringe and flash-frozen in liquid nitrogen. Final PHMcc copper concentrations ranged from 600 to 1200 µM.

Copper K-edge (8.9 keV) extended X-ray absorption fine structure (EXAFS) and X-ray absorption near edge structure (XANES) data were collected at the Stanford Synchrotron Radiation Lightsource operating at 3 GeV with currents between 300 and 450 mA maintained by continuous top-up. Samples were measured on beamline 7-3 using a Si[220] monochromator and Rh-coated mirror upstream with 13 keV energy cutoff in order to reject harmonics. Data were collected in fluorescence mode using a high-count rate Canberra 30-element Ge array detector with maximal count rates per array element of <120 kHz. A Z-1 nickel oxide filter and Soller slit assembly inserted in front of the detector was used to reduce elastic scattering relative to the Cu Kα fluorescence. Four to six scans of a sample containing only the buffer were averaged and subtracted from the averaged data for each protein sample to remove the Ni Kβ fluorescence and produce a flat pre-edge baseline. Samples were measured as aqueous glasses in 20% ethylene glycol at 10 K. Output from each detector channel was inspected for glitches and dropouts before inclusion in the final average. Data reduction and background subtractions were performed using the program modules of EXAFSPAK [145]. Spectral simulation was conducted using EXCURVE version 9.2 [146][148] as described previously [54][66][139][164]. Simulations of the EXAFS data used a mixed-shell model consisting of imidazole from histidine and S from methionine coordination. The threshold energy, E_0, was chosen at 8985 eV, and refinement of structural parameters included distances (R), coordination numbers (N), and Debye-Waller factors ($2\sigma^2$), and included multiple scattering contributions from outer-shell atoms of imidazole rings.

4.2.7 Stopped-Flow Spectroscopy

The protein sample was left in the anaerobic chamber for 30 minutes to deoxygenate, concentrated in an Amicon filter (10000 MWCO), and then diluted with argon-purged MES buffer (50 mM, pH 5.5) to a final concentration of 50 μM. For experiments performed in the presence of substrate, aliquots of stock solutions of Ac-YVG (K_m = 7 μM), hippuric acid (K_m = 1.2 mM) or nitrohippuric acid (K_m = 470 μM) were added to a final concentration of 100 µM or, in the case of the lower-affinity hippuric acid and nitrohippuric acid, 12 and 4 mM, respectively.

Pre-weighted DMPD, syringes, argon-purged deionized water, and buffer were made anaerobic by overnight storage in the anaerobic chamber. The 50 mM DMPD stock solution was made by dissolving preweighed salt in 1 mL of deionized water. This DMPD stock solution was used to prepare DMPD solution of 2 mM concentration, using deoxygenated deionized water.

Stopped-flow experiments were conducted under anaerobic conditions at room temperature on a SX20 Applied Photophysics stopped-flow instrument enclosed in a Vacuum Atmospheres anaerobic chamber with oxygen levels of ≤ 1 ppm.

4.2.7.1 Analysis of Stopped-Flow Data

DMPD (N, N-dimethyl-1, 4-phenylene diamine) is able to replace the physiological reductant ascorbate, undergoing one-electron oxidation to the radical cation with concomitant reduction of the enzyme copper centers [165]. The DMPD radical is a chromophoric agent which absorbs strongly at 515 nm (A_{515}) and 550 nm (A_{550}) with molar absorptivity at 515 nm of 5200 M^{-1} cm^{-1}. The formation of the DMPD radical strongly correlates with the reduction of the copper centers, making possible the measurement of copper reduction rates by monitoring the variation of absorbance at 515 nm (A_{515}) versus time.

The concentration of the reduced copper was determined from the equation

$$\text{Concentration of the reduced copper} = \frac{\Delta A_{515}}{\varepsilon_{DMPD}} \qquad \text{(4-1)}$$

Where ΔA_{515} is the difference in absorption at 515 nm at time t, and $\varepsilon_{DMPD} =$ 5200 M^{-1} cm^{-1}. The ratio of reduced copper to protein concentration was calculated for every time point and plotted versus the time using SigmaPlot 12.0. The total copper:protein ratio in each sample was also plotted as a reference value. The data were fit to a double-exponential equation for samples with both H- and M-sites intact (viz WT PHM, H108A, H172A, and H107A)

$$A_t = A_0 + A_1\,(1 - e^{-k_1 t}) + \, A_2\,(1 - e^{-k_2 t}) + \, ct \qquad \text{(4-2)}$$

Where A_1 and A_2 are the absorbance as a function of time for each of the two exponential time courses, putatively corresponding to reduction of the two copper centers with rate constants k_1, k_2, respectively. A_0 is the initial absorbance at time zero. In all experiments it was found that DMPD oxidation continued in a slow, almost linear phase for some time after the absorbance change indicated complete reduction of the copper centers. One explanation for the continued slow DMPD oxidation is enzyme turnover due to traces of oxygen that were not completely scavenged or enzyme instability resulting in other reductive events such as disulfide reduction, but other undefined enzymatic or nonenzymatic processes may also be occurring. To account for this effect, a linear factor (ct) was added to improve the fits at longer times in the reaction.

The reduction data of the mutants having only one of the two sites intact (H107AH108A and H242A) were fit to a single exponential equation.

$$A_t = A_0 + A_1\,(1 - e^{-kt}) + \ ct \tag{4-3}$$

A_1 is the absorbance associated with H-site (H242A) or M-site (H107AH108A), A_0 is the initial absorbance at t=0 and k is the rate constant. As before, a linear factor (ct) was found to improve the fits at long time points, presumably arising from non-catalytic sources of DMPD oxidation.

4.2.8 Protein Film Voltammetry

Protein film voltammetry was used to measure redox potential values of the proteins. A 3-5 μL drop of a protein solution was placed on a pyrolytic graphite electrode (PGE) surface, and samples were measured either after 3 min or when the drop was dried. All the experiments were performed in degassed 50 mM MES (pH 6.0) with 100 mM NaCl, on ice, and under Ar flow. The scan rate was either 250 or 100 mV/s, with a quit time of 2s. Data analysis was carried out using OriginPro9.0 (Origin Lab), licensed to the University of Illinois at Urbana-Champaign, using the previously reported procedure [166]. In brief, the presence of the peaks was confirmed by plotting the first derivative of the initial scans. The raw data was analyzed using the “peak analysis” option in Origin software. Through the process, the faradaic capacitance of background was subtracted to obtain the red curves shown in Figure 4-12, Figure 4-13, Figure 4-14, and Figure 4-15.

4.3 Results

4.3.1 Reduction Kinetics of WT PHM

Determining the independent rates of reduction of the H and M-sites required the enzyme to be stabilized in its fully reduced Cu(I) state. Therefore, to preclude turnover and prevent oxidation of the protein sample, the entire experiment, including the sample preparation, was performed under anaerobic conditions. Figure 4-2 (top left) shows a representative absorbance versus time plot for DMPD as a reductant with the associated time course at 515 nm as an inset. It can be seen that the absorbance rises rapidly from near zero in the visible (reduced DMPD is colorless) and eventually reaches a constant value. This endpoint represents less than 8% of the total DMPD present, indicating that another species (i.e, the concentration of the enzyme-bound copper) is the limiting reagent. The structure of the Cu(I) centers has previously been studied in detail by XAS for the ascorbate-reduced forms [167][55][66], including single site H and M structures[163][168][169], reactions with exogenous ligands [122][59], changes induced by pH [67][139], and active site mutants [167][67][139][141]. To verify that DMPD reduction generated the same reduced enzyme species, we first measured the EXAFS spectrum of a DMPD-reduced form of the WT enzyme, and analyzed its metrical parameters in MES buffer at pH 5.5.

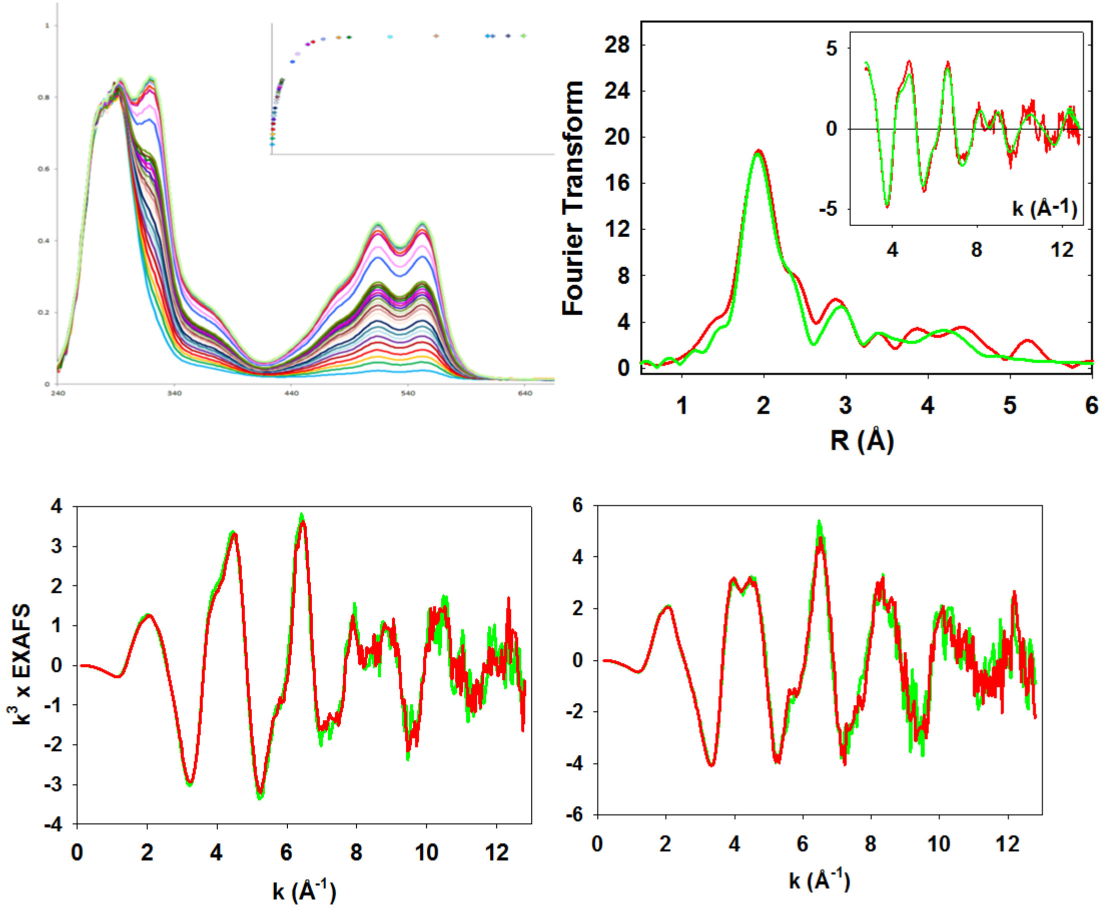

Figure 4-2 *Spectroscopic features of PHM reduction by DMPD (Top left) Stopped-flow absorbance versus time plot showing increasing absorbance in the visible due to formation of the DMPD cation radical one-electron oxidized species. (Top right) Fourier transforms and EXAFS (inset) for the DMPD-reduced PHM Cu(I) centers: experimental data are colored red and simulated data green. EXAFS data are shifted in k-space by an amount corresponding to the theoretical energy threshold. Parameters used in this fit are given in* Table 4-1. *Bottom panels show comparisons of DMPD-reduced (left) and oxidized (right) PHM in absence (red) and presence (green) of the substrate Ac-YVG.*

The results (Figure 4-2, top right) showed insignificant differences among ligation, bond-lengths, and Debye-Waller factors of the DMPD and ascorbate-reduced forms. The DMPD-reduced form was simulated by an average per copper coordination of 2.5 histidine and 0.5 S(Met) ligands with bond lengths of 1.96 ± 0.02 Å and 2.27 ± 0.02 Å, respectively. This compares favorably with the coordination previously determined for the ascorbate-reduced enzyme at pH 5.5 of 2.5 Cu-His at 1.96 ± 0.02 Å and a 2.25 ± 0.02 Å Cu-S(Met) bond length[139]. We also investigated the effect of substrate binding to the reduced (Figure 4-2, bottom left) and oxidized (Figure 4-2, bottom right) enzyme on the EXAFS spectra. These data also confirmed the previous observation that substrate binding induces no structural rearrangement at the copper centers that can be detected within the resolution of the experiment, because the EXAFS data are superimposable.

	Cu-N(His)			**Cu-S(Met)**			E_0
F	N	R_{Cu-N}	$2\sigma^2$	N	R_{Cu-S}	$2\sigma^2$	
0.37	2.5	1.96	0.010	0.5	2.28	0.010	-2.84
	2.5C	2.94	0.012				
	2.5C	3.01	0.012				
	2.5C	4.16	0.016				
	2.5N	4.23	0.016				

Table 4-1 *Parameters used to simulate the EXAFS of the DMPD-reduced PHM (pH 5.5) in the absence of substrate.*
N is the shell occupancy, R the distance from the copper absorber to the scatterer, and $2\sigma^2$ *the Debye-Waller factor for that shell. The simulations included multiple scattering contributions from the Cu-C2/C5 and Cu-C3/N4 atoms of the imidazole rings of the histidine ligands. F is a goodness of fit parameter defined previously as* $F^2 = {}^{1}/_{N} \sum_i k^6 \left(\chi_i^{theory} - \chi_i^{experiment}\right)^2$

Figure 4-3 shows kinetic traces for reduction of WT PHM in the absence and presence of the substrate Ac-YVG (empty blue circles and empty green circles, respectively). The dashed line represents the initial total copper:protein ratio at the beginning of the experiment (2.3 Cu per protein). The solid curves represent the simulated traces using fits generated from Equation (4-2) The data show that in the absence of the substrate, approximately half of the total oxidized copper present in the sample is reduced within 200 ms, followed by the slower reduction of the rest of the oxidized copper present in the sample in a second phase taking ~2.5 s to reach completion.

Curve fitting shows that the reduction is a biphasic process with one of the copper centers being reduced in an initial fast phase, followed by a much slower reduction of the other copper center. This is not an entirely unanticipated result because the ligand sets of the copper centers as well as their functions differ. However, at this point it is not possible to assign either rate to a specific Cu center (H or M). The rates of reduction in the presence of the substrate Ac-YVG exhibit different behavior. Although both rates are accelerated, there is a much larger increase in the rate of the slow phase.

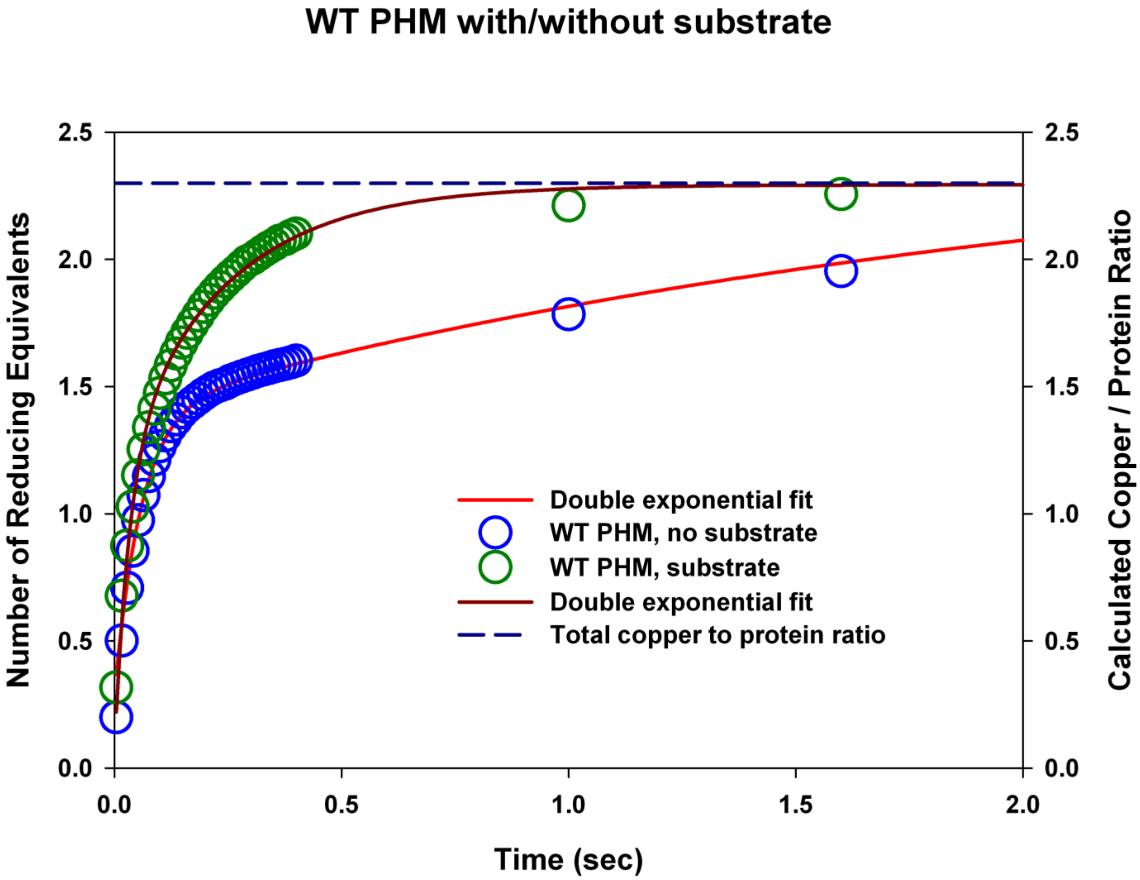

Figure 4-3 *Reduction kinetics of the WT PHM (0-2 seconds).*
Empty blue circles, WT PHM in the absence of substrate along with the double exponential fit (red line); empty green circles, WT PHM in the presence of the substrate Ac-YVG along with the double exponential fit (brown line) The dashed blue line represents the total copper to protein ratio in the WT PHM sample. The parameters used for the fits are listed in Table 4-2. *Note that the split time base used to capture the end point of slower phase results in fewer time points after 400 ms.*

The kinetic traces were fit to a double exponential equation to obtain the value of the rate constants which are listed in Table 4-2. The rate constant of the slow phase (0.46 s^{-1}) is accelerated by a factor of 10 in the presence of the substrate (4.2 s^{-1}), whereas the rate constant of the fast phase (17.2 s^{-1}) is accelerated by a factor of 2 (30.8 s^{-1}). Use of the substrate nitrohippuric acid showed a similar trend with the slow and fast rates increasing by factor of 6 and 2, respectively. However, hippuric acid accelerated the slow phase by only 4.3-fold and decreased the fast phase by a factor of 1.7 (Table 4-2, Figure 4-4 and Figure 4-5).

Sample	CuH[a] amplitude	CuH Rate(s^{-1})	CuM[a] amplitude	CuM Rate (s^{-1})
		No Substrate		
WT PHM	1.1	17.6(6)[b]	1.0	0.5(1)
H242A	0.7	42.5(10)		
H107AH108A			0.7	0.026(5)
H108A	0.6	40.3(8)		
H172A	0.9	19.8(8)	0.3	12.9(9)
		With Substrate		
WT Ac-YVG	1.1	30.7(19)	1.1	4.2(3)
WT Nitrohippurate	0.9	37.5(13)	1.1	2.8(2)
WT Hippurate	0.7	9.7(11)	1.1	2.0(5)
H242A-AcYVG	0.7	26.3(1)		
H107AH108A-AcYVG	0.6		0.6	0.025(1)
H108A-Ac-YVG	0.7	38.9(7)		
H172A-Ac-YVG	0.9	24.0(4)	0.6	4.1(1)

Table 4-2 *Rate constants for reduction of WT PHM and its variants in the absence and presence of substrates.*

[a] *Values of the amplitude of each exponential are related to the site occupancy of H and M sites. They were initially floated to determine approximate values and then fixed in subsequent iterations of the non-linear regression analysis*

[b] *Numbers in parentheses represent the standard deviation in the preceding value. Thus 17.2(6) represents 17.2 ± 0.6 while 42.5(10) represents 42.5 ± 1.0.*

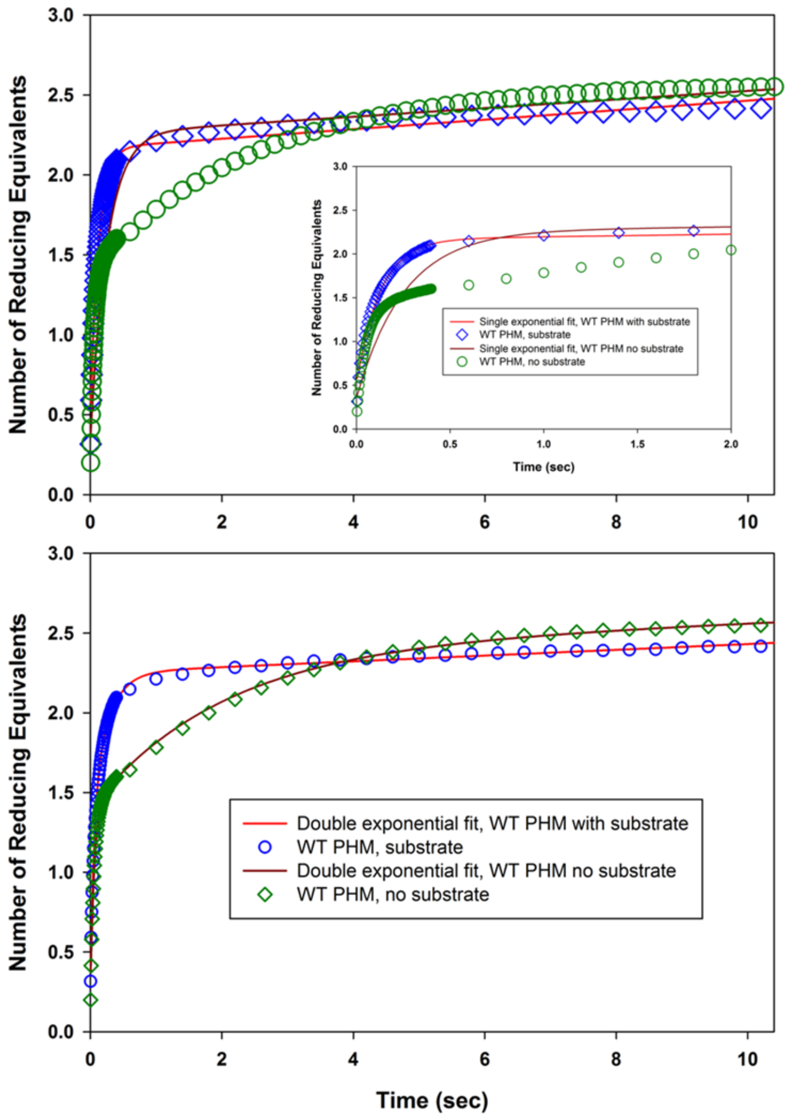

Figure 4-4 *Comparison of single and double exponential fits to the reduction kinetic traces of the WT PHM in the absence of and presence of the substrate Ac-YVG. Top panel: Single exponential fits to WT data in presence (blue squares) and absence (green circles) of Ac-YVG. The inset shows an expanded time scale to more clearly depict the behavior at earlier time points. Bottom panel: double exponential fits in absence (green squares) and presence (blue circles) of Ac-YVG. Although the double exponential fits appear to better simulate the experimental data, the single exponential in the presence of substrate gives an acceptable fit with k= 8.0 ± 0.2 s^{-1}. However, the single exponential fit requires amplitude of 1.6 reducing equivalents due to deviation of the simulated curve at time points close to zero, and a consequent higher value of Y_0. This is less consistent with the experimentally determined copper:protein ratio of 2.3.* Fitting results for the single and double exponential fits are given below in Table 4-3 and Table 4-4.

Sample	Y_0	Amplitude	Rate Constant	Linear Factor	R^2
WT PHM No Substrate	0.36(4)	1.9	3.96(2)	0.020(1)	0.881
WT PHM Substrate	0.52(2)	1.6	8.0(2)	0.030(2)	0.991

Table 4-3 *Single exponential fits*

Sample	Y_0	Amplitude		Rate Constant		Linear Factor	R^2
		Fast	Slow	Fast	Slow		
WT PHM No Substrate	0.30(1)	1.1	0.1	17.2(3)	0.5(2)	0.170(1)	0.998
WT PHM Substrate	0.30(1)	1.1	0.1	30.7(19)	4.2(3)	0.020(1)	0.998

Table 4-4 *Double exponential fits*

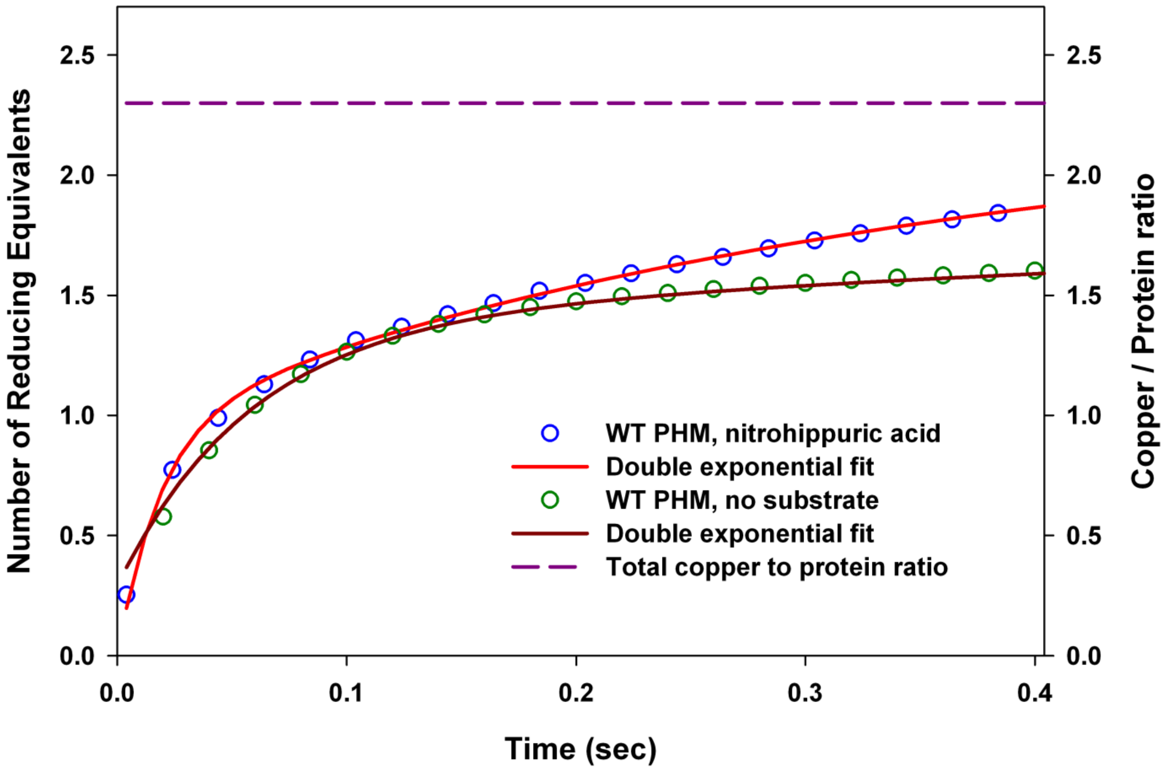

Figure 4-5 *Reduction kinetic traces of the WT PHM in the absence of substrate (empty green circles) and presence of the substrate nitrohippuric acid (empty blue circles), both fitted to a double exponential equation. The dashed purple line represents the total copper:protein ratio in the WT PHM. The parameters used for the fits are listed in the* Table 4-2*.*

4.3.2 Assigning Slow and Fast Rates to their Respective Copper Centers

In previous work, we reported two PHM variants H242A and H107AH108A in which one histidine residue at the M center (H242) and two histidine residues at the H center (H107 and H108) were mutated to alanine, and showed that these variants displayed properties consistent with single copper site occupancy at the H and M sites, respectively [68]. Specifically, ICPOES analysis indicated that each variant bound only a single copper atom, and EXAFS of the reduced forms could be simulated using the expected ligands sets for the chemically inequivalent H (3 His) and M (2His + 1 Met) copper centers, respectively. These single site variants were used to assign the fast and slow rates of reduction observed in the WT enzyme to the H and M copper centers. After protein isolation and copper reconstitution, ICPOES was used to confirm copper:protein ratios for H242A (H-site) of 0.96, and H107AH108A (M-site) of 0.90, indicating almost full occupancy of the individual centers. Both the mutants were found to be inactive in the assay conducted on the oxygen electrode (data not shown).

Figure 4-6 shows the reduction kinetics of the H242A H-site mutant in the presence and absence of Ac-YVG (empty blue circles and empty green circles, respectively). The reduction event is fast and is complete within 150 ms. There is a complete absence of the slow phase. The data fit well to a single exponential equation, further confirming that the reduction is a monophasic event. A higher percentage of copper atoms (92%) was reduced in the presence of the substrate compared to 82% in its absence.

Figure 4-7 shows the reduction kinetics of the H107AH108A M-site only mutant in the presence and absence of the substrate Ac-YVG (filled cyan circles and filled purple circles, respectively). The time taken for reduction of the single M-site suggests that it is a much slower process. Only 53.4% of the copper in the M-site was reduced by 100 s compared to almost complete reduction of the H-site in 150 ms. Reduction of the isolated M center in H107AH108A takes more than 200 s to reach completion (data not shown). The presence or absence of substrate has negligible effect on the rate of the reduction event (Table 4-5). These results allow us to assign unambiguously the fast reduction rate to the H-site and the slow rate to the M-site in the WT PHM.

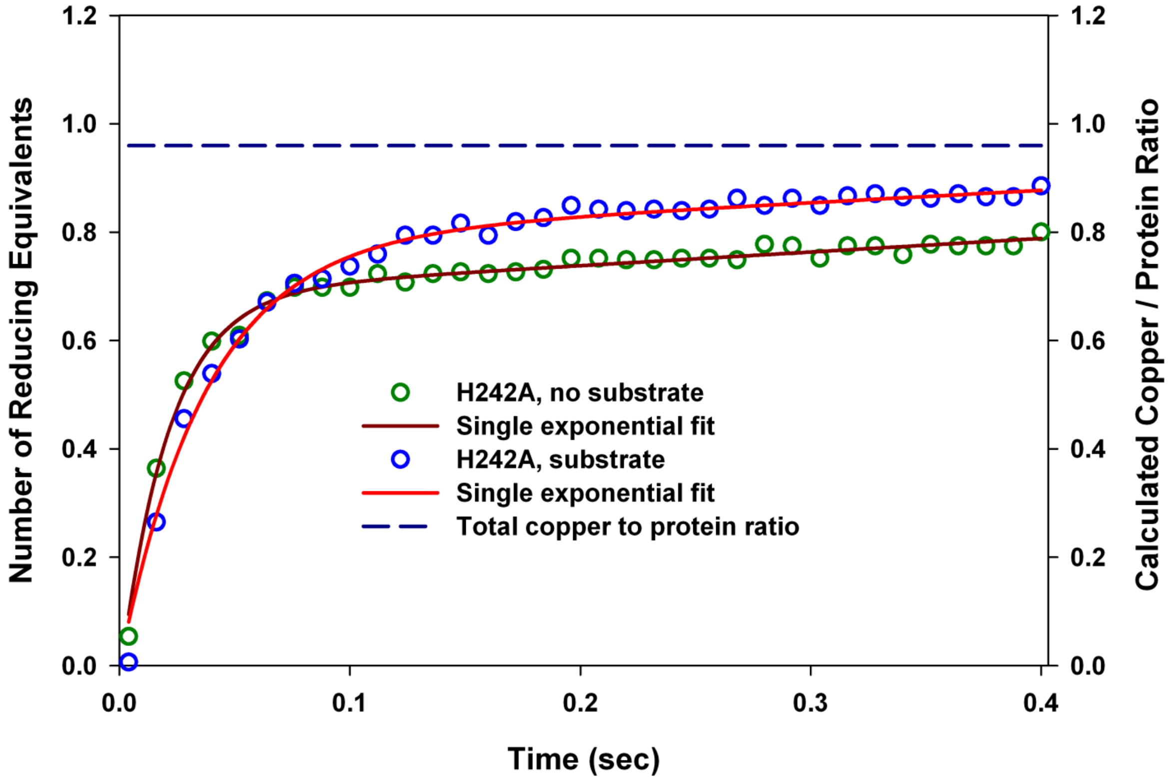

Figure 4-6 *Stopped-flow reduction kinetic traces of the H242A mutant (H-site only) (0-400 ms) in the absence of substrate (empty green circles) fitted to a single exponential (brown line) and in the presence of the substrate Ac-YVG (empty blue circles) fitted to a single exponential (red line). The dashed blue line represents the total copper:protein ratio in the H242A sample. The parameters used for the fits are listed in* Table 4-2*.*

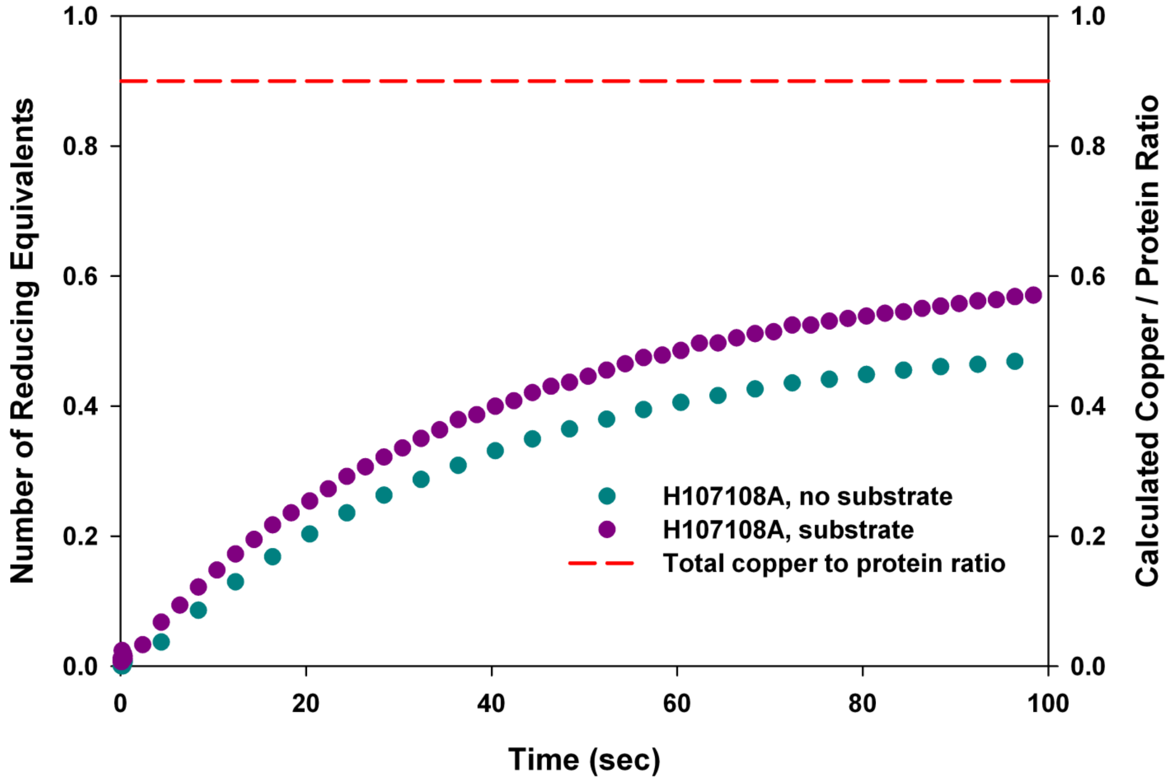

Figure 4-7 *Stopped-flow reduction kinetic traces of the H107AH108A mutant (M-site only) (0-100 s) in the absence of substrate (filled cyan circles) and in the presence of the substrate Ac-YVG (filled purple circles).The dashed red line represents the total copper to protein ratio in the H107AH108A sample. The parameters used for the fits are listed in Table 4-2.*

Sample	E_m(mV)	Standard Deviation
WT peak 1	-15	8
WT peak 2	270	5
WT + Ac-YVG	83	18
H242A	213	5
H107AH108A	140	2
H108A	270	1
H172A	(210)[a]	Poorly defined

Table 4-5 *E_m Values (vs NHE) for WT PHM and its variants at pH 6.0*
[a] *This mutant behaved poorly on the electrode and probably unfolded. This value therefore represents an estimate with a large undefined error.*

4.3.3 Importance of H-site Ligand H108 in the ET Process

In an effort to understand the role of H-site ligands in the ET process, reduction kinetics were measured for alanine variants of each of the three H-site ligands (H107A, H108A and H172A). H107A did not show any significant changes in the rate of reduction from the WT PHM (Figure 4-8) and was not studied in detail. More interesting results were obtained from the H108A and the H172A mutants. Figure 4-9 shows the reduction kinetics of the H108A mutant in the presence and absence of the substrate Ac-YVG (empty brown circles and empty green squares, respectively) compared with the WT PHM in presence of the substrate Ac-YVG (empty violet circles) over a 10 s time interval, while Figure 4-10 shows the initial 200 ms of reaction. The copper:protein ratio for the H108A sample was 1.9, indicating 95% occupancy of both the copper sites. The data highlights two important observations: 1) the slow phase, associated with the M-site, is completely absent, and 2) despite the presence of both the copper sites, only half the copper present in the sample is reduced. Because only the fast phase is present, it can be concluded that only the H-site is being reduced in the H108A mutant. The data fit well to a single exponential equation (Figure 4-10) and the value of the rate constants confirms that the rate of reduction is both fast and monophasic (Table 4-2). The results show that the M-site is not reduced in the H108A mutant in the time-frame of the experiment (10 s). This very surprising result provides evidence that the electrons are transferred from the H-site to the M-site via a specific path, which is destroyed when H108 is mutated, and implies that H108 is one of the key components of the pathway utilized for delivery of electrons into the M-site.

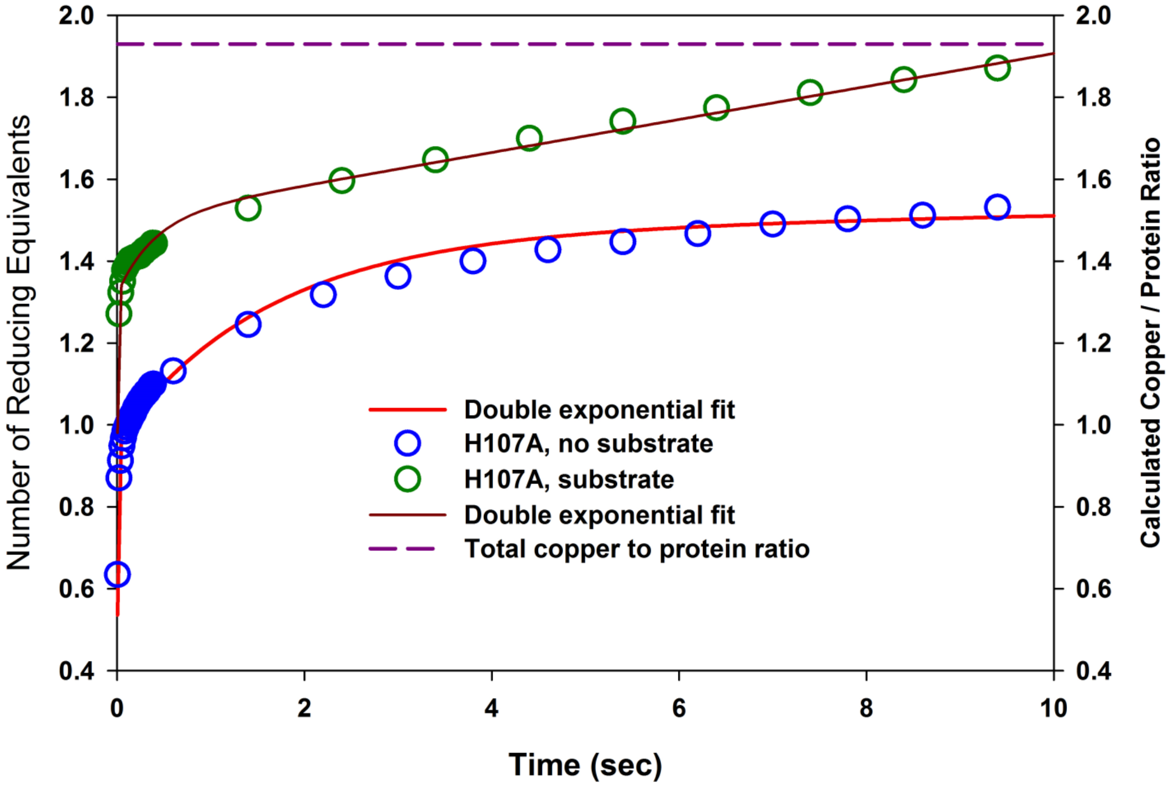

Figure 4-8 *Stopped-flow reduction kinetic traces of the H107A in the absence (empty blue circles) and presence (empty green circles) of the substrate Ac-YVG. The dashed purple line represents the total copper:protein ratio in the sample. The parameters used for the fits are listed in Table 4-2.*

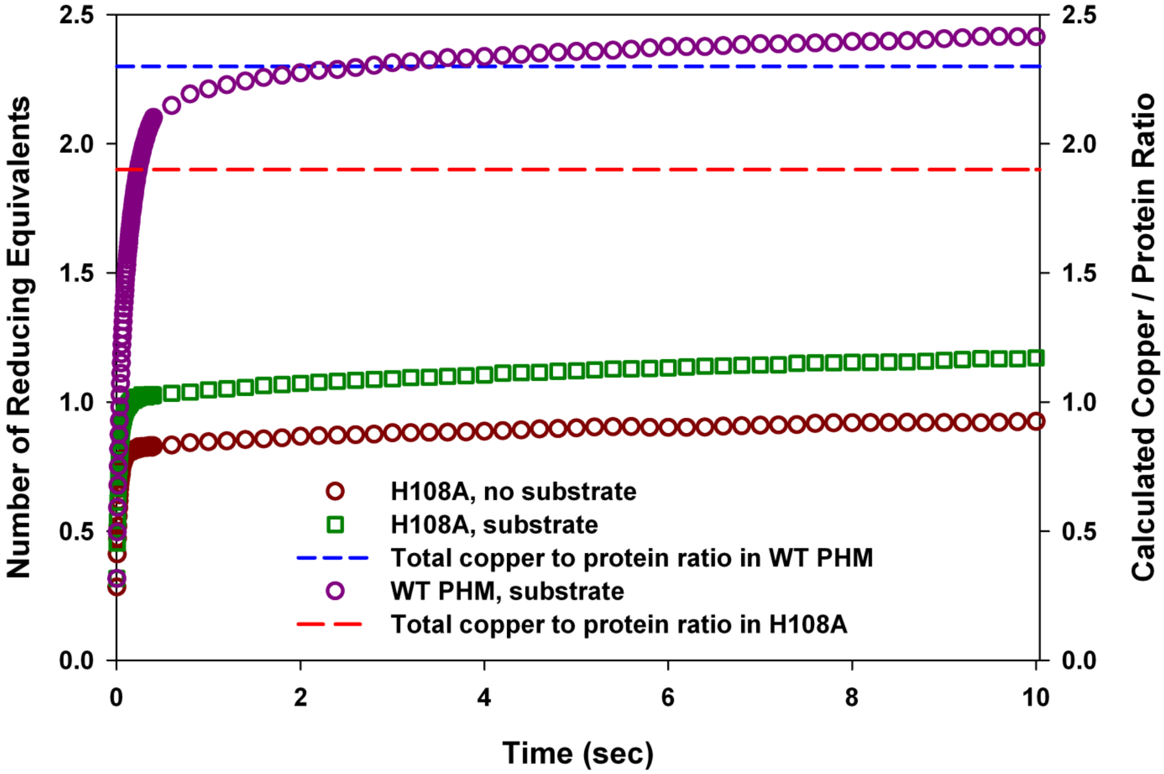

Figure 4-9 *Stopped-flow reduction kinetic traces of the H108A mutant (0-10 s) in the absence of substrate (empty brown circles) and in the presence of substrate Ac-YVG (empty green squares). Data for WT PHM in the presence of substrate Ac-YVG is shown for comparison (empty purple circles). The red and the blue dashed lines represent total copper:protein ratio in the H108A and the WT PHM samples, respectively.*

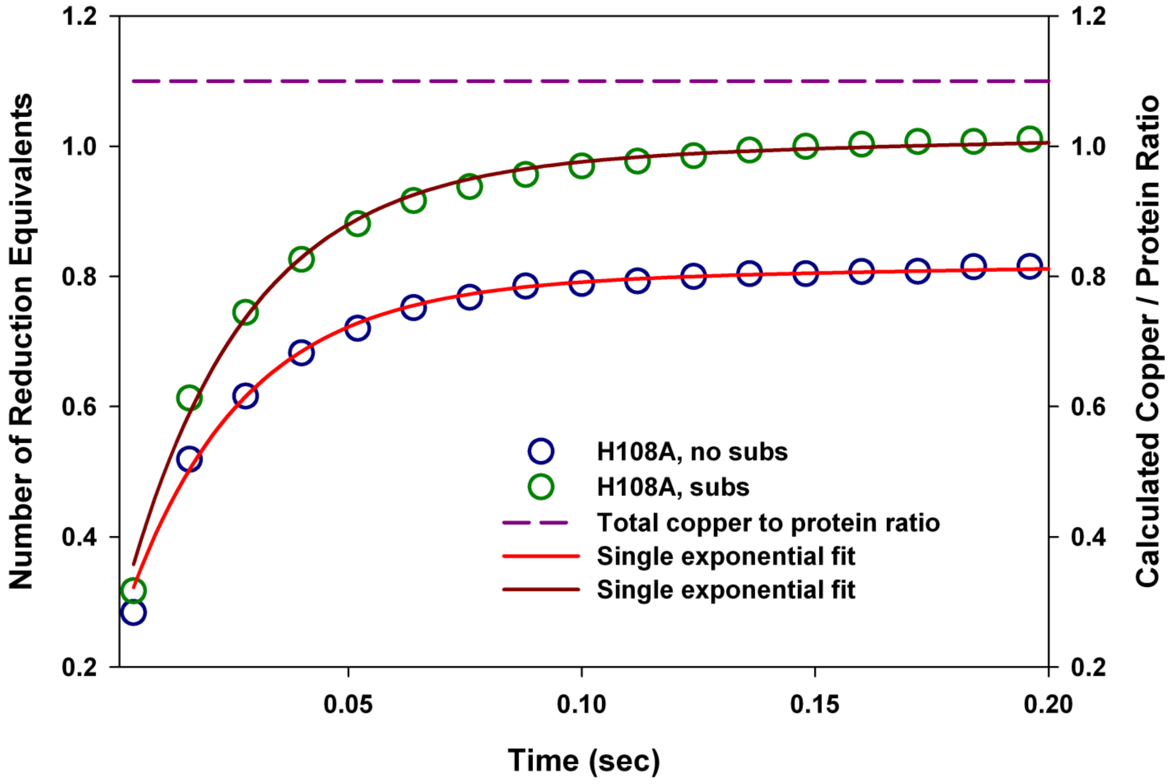

Figure 4-10 *The expanded view of the stopped-flow reduction kinetic traces of the H108A mutant (0-200 ms) in the absence of substrate (empty blue circles) and in the presence of the substrate Ac-YVG (empty green circles) fitted to single exponential fits. The parameters used for the fits are listed in Table 4-2*

4.3.4 H172A Reduction Kinetics

We have reported on the structural and kinetic properties of the H172A variant in previous studies. [141][170]. H172A is <0.3% active compared to the WT PHM. Copper binding and K_m (Ac-YVG) are not affected; however, the k_{cat}/K_m (O_2) shows a 300-fold decrease in magnitude compared to that of the WT enzyme, and kinetic isotope analysis suggests a large decrease in the rate of the chemical step (H atom abstraction) [141][170]. Reduction kinetics were performed in the hope of clarifying the role of H172 in the ET process.

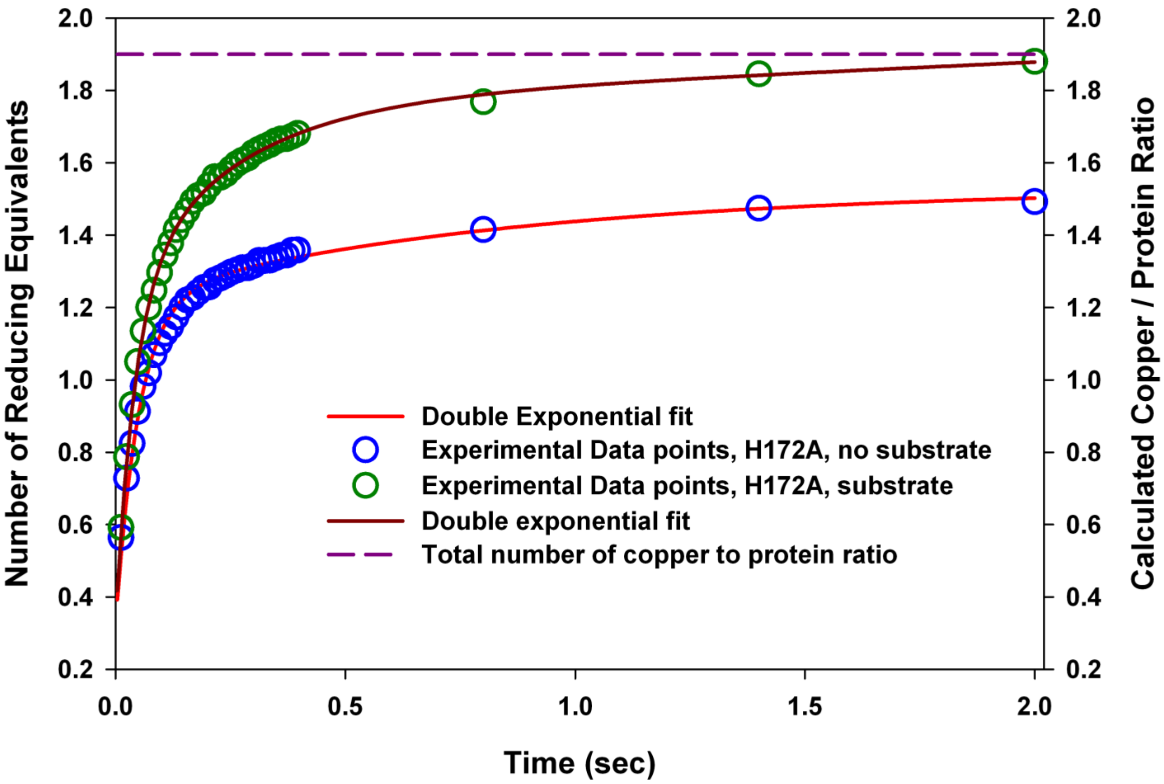

Figure 4-11 *Stopped-flow reduction kinetic traces of the H172A mutant (0-2 s) in the absence of substrate Ac-YVG (empty blue circles) fitted to a double exponential (red line) and in the presence of the substrate Ac-YVG (empty green circles) fitted to a double exponential (brown line).The purple dashed line represents the total copper:protein ratio in the H172A sample. The kinetic parameters used for the fits are listed in* Table 4-2. *Note that split time base used to capture the end point of the slower phase results in fewer time points after 400 ms.*

The total copper:protein ratio in the sample was 1.9, indicating 95% occupancy of both the H- and M-sites. The data for H172A reduction (Figure 4-11) are similar to those of the WT PHM, with the same characteristics, that is, the reduction is biphasic with a faster phase (<200 ms) and a slow phase (~2.5 s). Nonlinear regression analysis shows that the rate constant of the fast phase is comparable to that of the WT PHM in the absence of the substrate (Table 4-2). The slow phase, however, is at least 2.6 times faster and is little changed in the presence of substrate. The results suggest that H172 is not an important pathway residue for electron delivery to the M center, although the lack of a substrate dependence of the slow rate is puzzling. It is possible that redox potential effects are more important than pathway residues in this variant.

4.3.5 Protein Film Voltammetry

To explore the contribution of changes in redox potential to the reduction rates, we measured the redox potentials of the two copper centers using protein film voltammetry [171][172]. For all experiments, reversible waves were obtained (Figure 4-12, Figure 4-13, Figure 4-14, and Figure 4-15). As expected on the basis of the chemical inequivalence of H and M centers, the WT protein generated two waves centered at -15 mV and 270 mV versus the normal hydrogen electrode (NHE) where the more negative value would be consistent with slower M-site reduction and the larger (more positive) value would be consistent with the faster H-site reduction. In the presence of the substrate Ac-YVG, a single (unresolved) PFV wave was obtained centered at a potential of +83 mV, consistent with the observation that substrate binding decreases the difference in reduction rates of the two copper centers. Experiments using the single H-site variant H242A gave a potential of 213 mV closer to that observed for the WT peak 2 (Table 4-5). This observation confirms that the fast reduction rate is associated with the H center. The single M-site variant H107AH108A gave a potential of 140 mV, 60 mV more positive than the WT in the presence of substrate. These data suggest that the M-site potential is very sensitive to changes in its environment induced by nearby substrate binding, as well as more distant effects such as loss of metal from the H center. Factors such as solvent ordering and/or charge distribution in the active site cleft may also contribute to the observed trends in the redox potentials.

Despite the loss of a coordinating His residue, the H108A and H172A variants each bind two coppers [67], and therefore like WT, might be expected to exhibit two separate potentials. However, the H108A variant showed only a single peak with potential of ~270 ±1 mV vs the NHE. Because this peak is identical to that observed for WT peak 2 (Table 4-5), this peak can be assigned to the H-site. Of great interest, the removal of a His ligand to give a two-coordinate structure as determined from EXAFS studies of this mutant [67] does not appear to perturb the potential in the absence of substrate, giving support to previous conclusions that only two of the three His residues are coordinated in the WT H center [68][66]. The lack of a peak at lower potentials corresponding to the CuM-site may suggest that its observation is limited by slow reduction kinetics, which would be in good agreement with our kinetic data that show that reduction of the CuM-site does not occur on the 10 s time scale of the experiment. For H172A we observed a broad peak at ~210 mV versus the NHE, close to that of H108A, and believe that this peak, at least partly, is from the CuH-site. The oxidative peak was very small, and any effort to increase the magnitude of the signal by increasing the protein concentration or longer incubation times resulted in unfolding the protein and the appearance of an intense peak due to unfolded protein (data not shown). Moreover, because the peak was broad, it is possible that it is from two sites, similar to what was observed in WT-PHM with the peptide. In this case, the result is consistent with faster reduction rates of H172A. However, the resolution of the data and the low stability of H172A on the electrode surface made it hard to draw any definite conclusions.

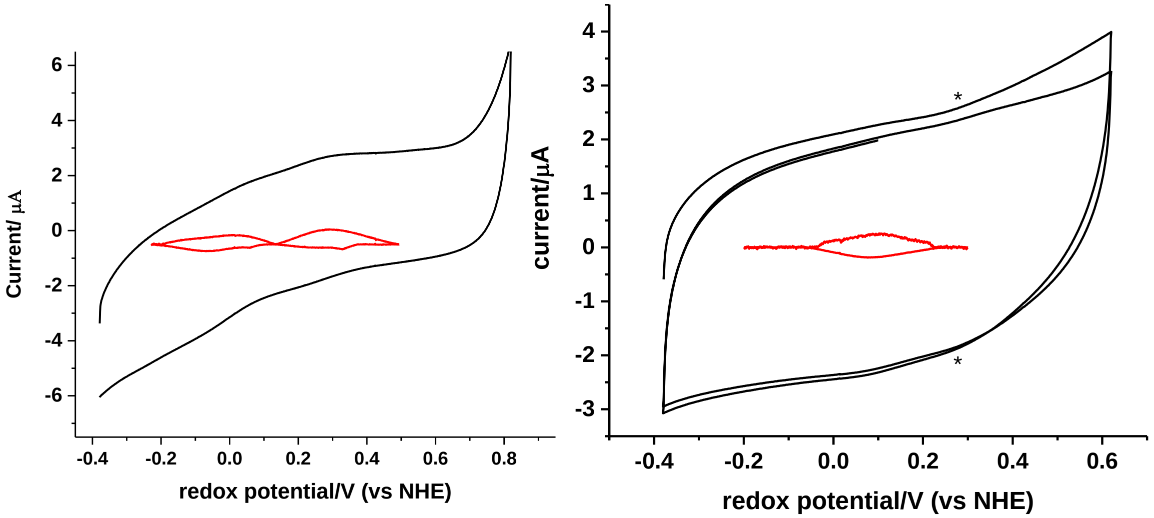

Figure 4-12 *Reversible behavior of the PHM Cu(II)/Cu(I) redox couple in the absence (left) and presence (right) of Ac-YVG substrate. Voltammagrams were measured in 50 mM MES, (pH 6) with 100 mM NaCl, on ice, and under Ar flow. The scan rate in all cases was 250 mV/s (black line). The signal with the capacitative current subtracted is shown as an inset in the middle (red line).* E_m *values are listed in* Table 4-5.

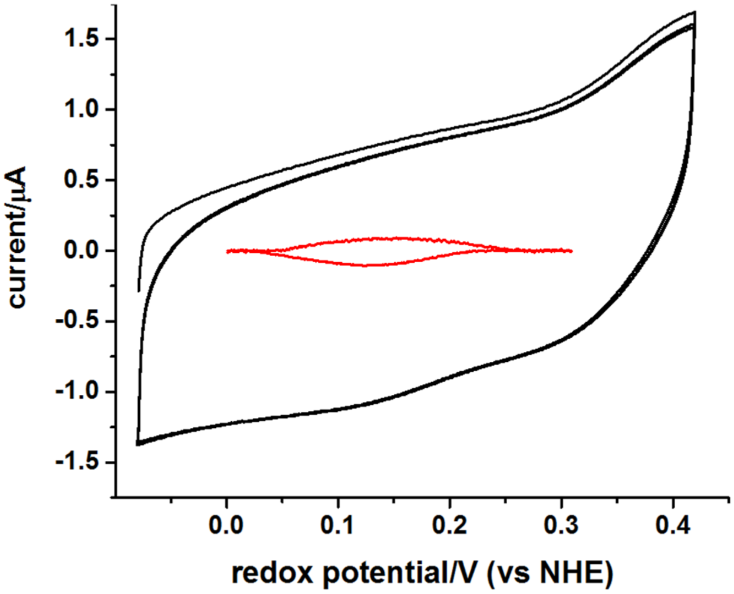

Figure 4-13 *Reversible behavior of the H107AH108A PHM (M-site only). Voltammagrams were measured in 50 mM MES, (pH 6) with 100 mM NaCl, on ice, and under Ar flow. The scan rate in all cases was 250 mV/s. (black line). The signal with the capacitative current subtracted is shown as an inset in the middle (red line).* E_m *values are listed in* Table 4-5.

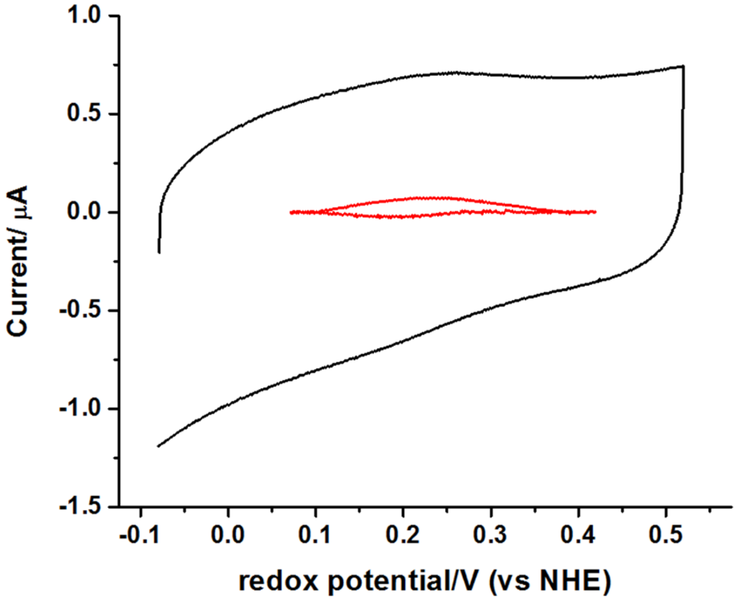

Figure 4-14 *Reversible behavior of the H242A PHM (H-site only). Voltammagrams were measured in 50 mM MES (pH 6) with 100 mM NaCl, on ice, and under Ar flow. The scan rate in all cases was 250 mV/s. (black line). The signal with the capacitative current subtracted is shown as an inset in the middle (red line).* E_m *values are listed in* Table 4-5.

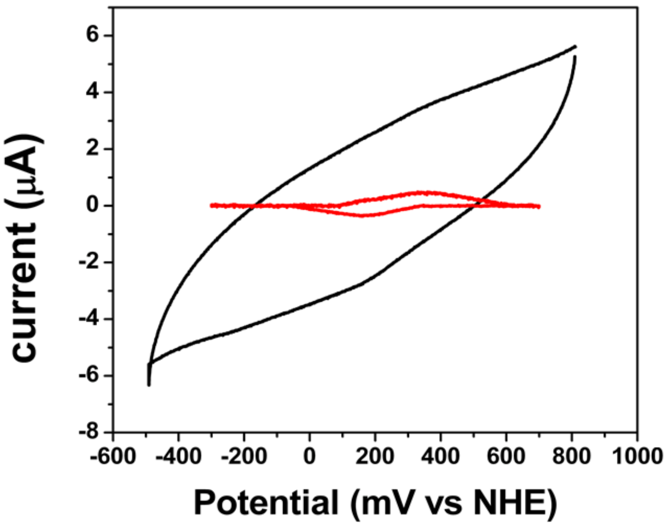

Figure 4-15 *Reversible behavior of the H108A PHM. Voltammagrams were measured in 50 mM MES (pH 6) with 100 mM NaCl, on ice, and under Ar flow. The scan rate in all cases was 250 mV/s. (black line). The signal with the capacitative current subtracted is shown as an inset in the middle (red line).* E_m *values are listed in* Table 4-5.

4.3.6 Discussion

We have investigated the reduction of fully oxidized PHM to its Cu(I)M – Cu(I)H form using the chromophoric reductant DMPD. For the WT protein, a two-step process is observed, suggestive of differing rates of reduction for each of the two copper centers. Measurements on the two single-site variants H242A (H-site occupied, M-site empty) and H107AH108A (M-site occupied, H-site empty) [68] have allowed us to assign the fast rate to reduction of the H-site and the slow rate to the reduction of the M-site. Whereas the rates of H-site reduction were largely unchanged between WT and the single-site H variant, the rate of reduction of the M center was two orders of magnitude slower when the H center was absent. This latter observation implies a fundamental difference in reduction mechanism between PHM derivatives containing both centers and those where the H center lacks its metal, and strongly supports a mechanism in which electrons enter preferentially at a site in the vicinity of H and are then transferred via an intramolecular pathway to the M center. In the absence of the H center, this latter pathway is unavailable and reduction likely reverts to a less efficient outer-sphere interaction between the DMPD and the Cu(II) ligand environment at the M center.

The pathway for intramolecular electron transfer in PHM and DBM has generated much debate in the literature, but current proposals are still speculative. The copper centers are separated by 11 Å of solvent-filled channel [35][125][69], while large changes in first-shell coordination spheres occur at both copper centers as a result of reduction of the oxidized protein to the di-Cu(I) form [66]. These structural attributes might be expected to inhibit rapid intersite ET due to the large reorganizational energies anticipated as the result of ligand and solvent rearrangement.[122]. The shortest "through-bond" pathway is about 80 Å, which in the absence of multiple intervening redox centers [114] is too long for efficient intramolecular ET. These factors have prompted a number of alternative suggestions for the preferred ET pathway by mechanisms that allow short-circuiting of the through-bond pathway. Jaron and Blackburn initially proposed the superoxide channeling mechanism in which O_2 reacted first with Cu(I) at the CuH-site, and the superoxide that was formed then migrated across the 11 Å solvent-filled cavity and reacted with CuM(I), to generate an "active" CuM-peroxo species. This mechanism in which the electron is carried by the superoxide entity, predicted that under conditions or with mutants where the reaction is very slow, the superoxide would “leak” out of the cavity and lead to uncoupling of oxygen consumption from substrate hydroxylation. Subsequent observations that oxygen consumption remained 100% coupled to hydroxylation in H172A [141] and M314H [139] even though the catalytic rate had decreased up to 1000-fold rendered this mechanism untenable. A second proposal suggested by Amzel and coworkers on the basis of crystal structures [133][35][125] involved an ET pathway comprised of H108, Q170, a water molecule, and the peptide substrate. However, mutation of the critical substrate-mediated pathway residue Q170 had only limited effects on the steady state kinetics [163]. A third suggestion from Klinman and coworkers [127] proposed that the electron could transfer across the intersite cavity, perhaps assisted by Y79 provided the solvent was ordered. This latter mechanism has also been tested *in silico* where a pathway composed of a chain of three H-bonded water molecules was calculated to have sufficiently low activation energy for rapid proton-coupled ET provided that the CuM-site acceptor was the Cu-O• (cupryl) species [173]. A mechanism involving interdomain motion has also been suggested [123] but deemed unlikely on the grounds that the interdomain distance does not change in any of the crystal structures published to date.

PHM is a monooxygenase, which means that that the external reductant supplies two of the four electrons necessary to reduce dioxygen, with the other two coming from the activated C-H bond of the substrate. These electrons are stored on the enzyme in the two uncoupled Cu(I) sites, but it is important to recognize that they are different mechanistically and are transferred to the catalytic M center at different stages of the reaction cycle. The first electron reduces the Cu(II)M species to the Cu(I)M state prior to binding of dioxygen at M. The second electron is transferred after the enzyme has committed to catalysis and is generally believed to reduce a high-valent species such as Cu(III)=O or Cu(II)-O• formed after the O-O bond has broken [126][80][136]. The study presented here focuses on the initial reduction of the M center and therefore relates only to the first electron. To gain further insight, we examined the effect of the presence of peptide substrate on the reduction kinetics.

Binding of Ac-YVG was found to accelerate the rate of M-site reduction in the WT protein by a factor of ~10 (see Table 4-2), such that the reduction rates of each metal center were less disparate. This result suggests that one important mechanistic attribute of substrate binding is to couple the redox chemistry of the two centers such that they behave more as a coupled system even though they are separated by 11 Å. This electronic coupling could arise from effects on the redox potentials of CuH and CuM (thermodynamic) or from more efficient long-range electronic coupling (kinetic). Data from protein film voltammetry supports an effect on the redox potential as one factor in the substrate activation. Voltammagrams of the WT protein in the absence of substrate show two reversible waves centered at mid-point potentials of 270 mV and -15 mV, while H-site and M-site single site variants show mid-point potentials of 213 and 140 mV, respectively. This suggests that an E_{red} (WT) of 270 mV can be assigned to the H center while an E_{red} (WT) of -15 mV should be assigned to the M center. In the presence of substrate, only a single reversible wave was observed at E_{red} (WT, Ac-YVG) of 83 mV. The single wave in the presence of substrate could arise from substrate coupling of the two copper centers so that they reduce at the same potential, or to the average of two nonresolvable midpoint potentials of near equivalent value. In either case, the CV data are in good agreement with the kinetic data, and imply that the substrate activates the first reductive step by equalizing the redox potential of each center. Similar substrate activation has been observed in cytochrome P450, where binding of camphor leads to an increase in E_{red} for NADH reduction [174][175].

The structural origin of substrate redox coupling in the PHM system is of great interest. An increase in M-site potential could be due either to stabilization of the Cu(I)M state or a decrease in the stability of Cu(II)M. In previous work [68] we have established that the thioether ligand of M314 adopts both Met-on and Met-off conformations, because the shell occupancy is substoichiometric and pH dependent. This suggests that an increase in the occupancy of Met-on conformer might be responsible for the increase in potential, because thioether ligands favor the Cu(I) state. However, a careful comparison of the EXAFS of the reduced protein at pH 5.5 in the presence and absence of Ac-YVG failed to detect any change in the intensity of the Cu-S wave. An alternative possibility is that the binding of Ac-YVG to the PHM active site cavity via its salt bridge to R240 neutralizes one positive charge and affects the electrostatics of the active site cleft. However, this too is problematic, because the effect is in the wrong direction, where decreased positive charge should stabilize the cupric state and/or destabilize the cuprous state [176]. It is further possible that substrate binding could alter solvent structure and H-bonding interaction in the vicinity of metal centers. Indeed, a closer look at the structure of reduced PHM without substrate (PDB entry: 3PHM) and in the presence of substrate (IYG) (PDB entry: 1OPM) showed the possibility of such changes. First and foremost, the presence of the substrate would place the M-site in a more hydrophobic environment. Multiple studies have demonstrated increased hydrophobicity as a contributor to increased reduction potential of a metal site. Aside from this obvious change, subtle changes in the Cu sites can also be detected. As shown in Figure 4-16 , substrate binding causes an overall rearrangement of the solvent structure around the M site. The change in the arrangement of solvent molecules around a metal center has been postulated as a major factor in perturbing the redox potential of the site when other factors remain the same. The H-site also undergoes small but potentially significant geometrical rearrangement of the ligand orientation. Taken together, these factors may be sufficient to induce the changes in redox potential that are observed.

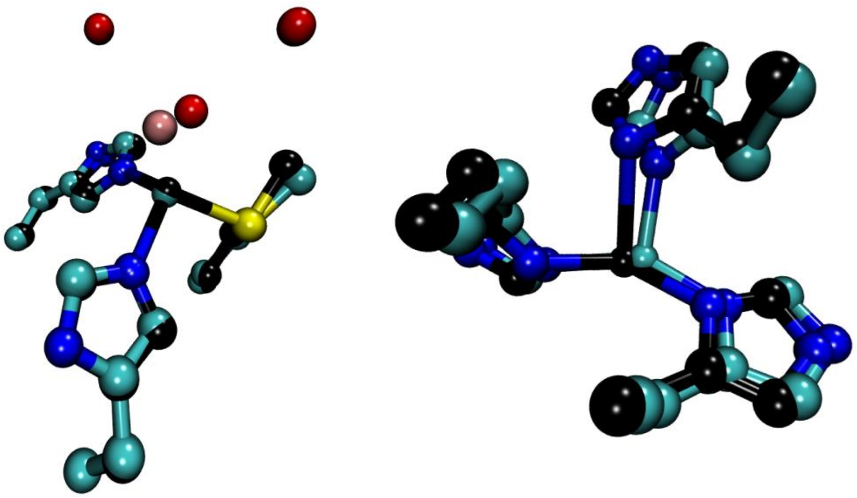

Figure 4-16 *Comparison of the M-site (left) and H-site (right) between WT PHM with substrate (black, PDB ID: 1OPM) and without substrate (cyan, PDB ID: 3PHM). The red balls are water molecules within 5 Å of CuM in the structure with the substrate. The pink ball represents a water molecule within 5 Å of CuM in the absence of the substrate*.

To further explore the importance of intersite electronic coupling, we examined the reduction rates of H center variants in which one of the coordinated histidine ligands was mutated to alanine. Previous studies have shown that H-site single histidine to alanine variants (H107A, H108A, H172A) are fully competent to bind Cu(I) in a two-coordinate structure involving the two remaining His ligands [67]. The reduction rates of these variants therefore inform as to which His residue is important in the intramolecular ET pathway. To our surprise, we found that whereas H108A could be rapidly reduced by one equivalent per copper, further reduction was not observed on the time scale of the experiment (0 – 10 seconds). We ascribe the first reducing equivalent to the reduction of the H center that proceeds at a rate comparable to that of the WT protein. The abrogation of any further redox chemistry in this mutant strongly suggests that H108 is an essential element of the exit pathway for the H to M electron transfer. In support of this interpretation, we also observed that in the presence of substrate, the H172A variant was unperturbed relative to the WT protein. Redox potential measurements were also consistent with these arguments, showing only a single wave at 270 mV (Table 4-5) that can be assigned to the H-center, suggesting that redox chemistry at the M center might be kinetically limiting.[The more positive potential relative to the WT protein is expected on the basis of our recent EXAFS studies which showed a two-coordinate geometry more favorable to Cu(I) [67]]. These observations are in good agreement with Amzel's proposed "substrate-mediated" pathway involving H108, Q170, a water molecule, and the peptide substrate. The substrate-induced acceleration of reduction in the WT protein further supports this pathway, where long-distance electronic coupling through the substrate backbone could combine with its effect on redox potential to increase ET rates. The fast rates exhibited by the H172A variant in the absence of substrate are puzzling, and are not fully accommodated by the model, but it is possible that this mutation alters the intersite structure such that the advantage of electronic coupling via the substrate is lost.

While substrate mediated ET is an attractive hypothesis, and appears to be consistent with our new data, the failure of a Q170A mutation to abrogate catalysis has cast doubt on its validity [163]. The alternative pathway via His172 and the nearby Y79 that π-stacks against the histidine ring has been evaluated both experimentally [127][141] and computationally [80]. In this pathway, the tyrosine is about 7 Å from the CuM center and could operate as a facile ET pathway provided the intervening solvent is ordered. To evaluate the importance of this pathway, PHM H172A, and TBM Y216W, -I and -A variants have been studied. Detailed kinetic analysis of PHM H172A [170] based on both steady state and kinetic isotope data reported a 3 order-of-magnitude decrease in k_{cat}. Because this mutant bound copper with ratios close to that of the WT enzyme [141], the effect was not due to the loss of copper from the H center. Rather, and consistent with other His to Ala variants at the H center [67], the CuH structure was proposed to be two-coordinate, retaining its H107, and H108 ligands [141]. The impaired activity was traced to a dramatic reduction in the rate of C-H bond cleavage in the chemical step of the mechanism, which was suggested to arise from perturbation of important H-bonding networks that modulate H atom tunneling during the HAT chemistry. Thus, while the mutation of H172 was expected to impact H-site redox potentials and exit pathways, any decrease in ET rate was masked by the larger decrease in the rate of H-atom abstraction. For TBM Y216 variants (PHM Y79 homologues), a comparable effect on the HAT step was not observed, allowing the ET rates to be estimated. Here, the alanine mutation resulted in a profound decrease in H to M ET rate, such that it was now rate limiting. This work provided compelling evidence that a pathway that includes the Y79 residue must be important at least during the irreversible steps following dioxygen binding and activation.

We are therefore presented with two seemingly inconsistent findings: (i) the H108 – water – substrate pathway is implicated from the present work, and (ii) the H172 – Y79 – water pathway is implicated from previous work. However, these results are not necessarily inconsistent if we recognize that (as discussed above) the two electrons stored on the enzyme are different mechanistically and are transferred to the catalytic M center at different stages of the reaction cycle. The first electron reduces the Cu(II)M species to the Cu(I)M state prior to binding of dioxygen at CuM (the reductive electron), while the second electron is transferred after the enzyme has committed to catalysis (the catalytic electron). The pathway for each of these electrons need not be the same, and here we propose a new hypothesis that indeed they are not the same. We propose that H108 and a substrate molecule are involved in the reductive pathway while H172 and Y79 are important in the catalytic pathway. This hypothesis then allows us to rationalize an additional unique property of this class of monooxygenases, that substrate hydroxylation remains fully coupled to oxygen reduction even with very slow substrates [126], and with mutants of very low specific activity [141][67]. Our hypothesis posits that electron transfer is gated such that the catalytic electron can only flow from CuH to CuM after the enzyme has committed to catalysis. Otherwise, with slow substrates or mutants, reduction of the Cu(II)-superoxo species to peroxide could not be prevented, leading to uncoupling. By utilizing bifurcated ET, the enzyme can "gate" each pathway so that it is only operative during the appropriate phase of the reaction Figure 4-17.

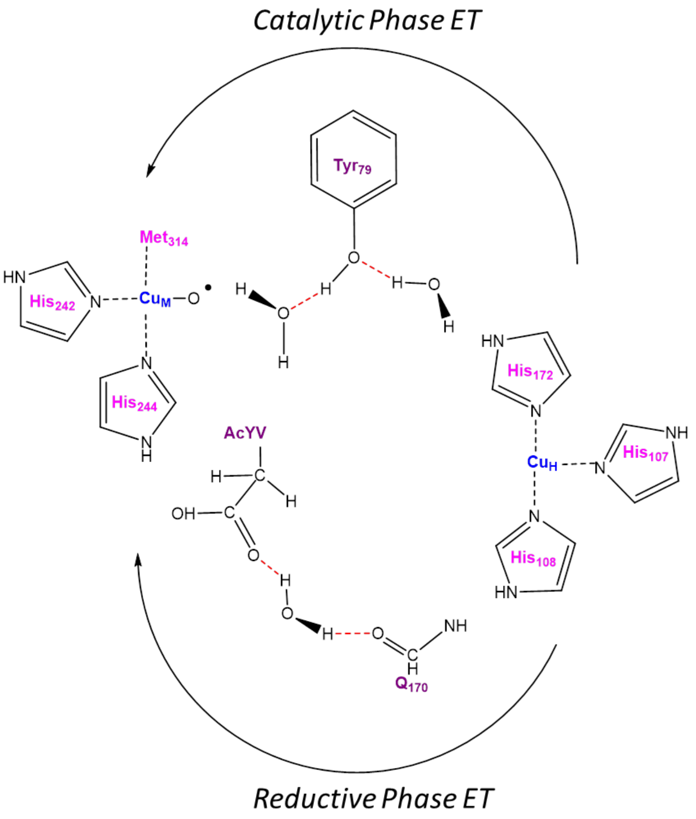

Figure 4-17 *Proposed bifurcated ET pathways for the reductive and catalytic electron transfer steps.*

The means by which the enzyme might gate these two ET pathways are unknown, but our work suggests a number of possibilities. First, we know from previous

EXAFS studies on WT [66] and the H242A H single-site variant[68] that one of the three His residues at CuH is very weakly bound; second, XAS on all three His to Ala variants at the H-site have established that the site becomes stably occupied by Cu(I) provided any two His ligands are present [67]. Third, removal of a His ligand at the H-center (H108A) does not perturb the E_m value in the absence of bound substrate. From these observations we predict that stable enzyme states can exist with H108 and H172 in either coordinated (on-states) or dissociated (off-states). This implies that H108 can act as a gate for transfer via the H108 –Q170-water-substrate pathway while H172 can act as a gate for the H172-Y79-water pathway. The gate is open when the ligand is "on" and closed when it is "off". The finding from the present study that H108A abrogates H to M transfer fully supports this idea. We can then model the ensuing gated chemistry as follows. The cycle begins with the oxidized enzyme having both coppers in the Cu(II) state, and CuH coordinated by all three histidines. Electrons enter the H-site and can rapidly transfer to CuM via the H108—substrate pathway. A second electron enters the H-site, but now the preferred enzyme state is a two-coordinate H center with H108 in the off position and H172 in the on position generating the fully reduced di-Cu(I) state ready to bind O_2. Since the gate is closed, no further ET from H to M is possible, and this form of the enzyme is therefore protected from uncoupling reactions that would generate H_2O_2 at the M-site. As the catalytic chemistry progresses, an enzyme state that is able to turn on the catalytic gate via H172 and Y79 is reached. It has been proposed that this event may be initiated by formation of a high potential intermediate such as a high-valent Cu(III)-oxo or Cu(II)-O•- species which is able to overcome the high reorganizational energy for ET through the H172-Y79 –water pathway [46][173]. One hypothesis worthy of merit posits that the electron “hops” from Y79 to the high-potential intermediate, forming a transient tyrosyl radical hole. This process would require a potential of at least 920 mV [177] that would be accessible only after O-O bond breaking such that formation of the tyrosyl hole would be gated by the catalytic chemistry [138]. Electron hopping through tyrosine or tryptophan residues has been well documented in ribonucleotide reductase [114], TTQ cofactor formation in methylamine dehydrogenase catalyzed by MauG [178][179], and photosynthetic reaction centers [180], and modeled by introducing nitrotyrosinate residues into ET pathways in azurin [181]. These studies have emphasized the importance of proton coupled oxidation (PCET) mechanisms for tyrosine hole formation because the phenol moiety must be deprotonated for oxidation to proceed at accessible potentials, requiring the presence of a proton acceptor that is usually H-bonded to the phenolate OH. We note that in the PHM system, an ordered chain of H-bonded water molecules bridging the phenolate and cupryl intermediate could fulfil this function, because a proton could be transferred via the H-bond network to the cupryl species as the tyrosyl oxidation proceeded. Further, the requirement for coupled proton transfer would provide additional tuning of the gate, because ET could only progress when the solvent was properly ordered between the donor and acceptor. The final electron transfer from CuH to Y• would occur rapidly via the π-stacked H172 residue.

It is important to note that mutagenesis of PHM-Y79 to W reduced V_{max} 200 fold [163], while the effect of mutation of TBM-Y216 to W or I was minor, and could be traced primarily to changes in the rates of substrate and product release [127]. Whereas tryptophan radical holes have been implicated in MauG [179], the insensitivity of the TBM catalysis to isoleucine substitution suggests that aromatic radical hole formation is not an essential factor. An alternative hypothesis for the ET pathway of the catalytic electron has recently been suggested from studies on the TBM system. Unlike the TBM Y216W and -I variants, the TBM Y216A mutant shows rate-limiting electron transfer [127], which has allowed the deuterium solvent isotope effect on this rate constant to be determined [128]. The size of this isotope effect and its T-dependence indicate a large entropic contribution to the driving force, suggesting solvent reorganization as a critical step in the catalytic ET process. The data lead to the conclusion that the phenol moiety of Y216 (PHM Y79) participates in and helps to pre-organize a network of ordered water molecules which extend from the H-site to the M-site. How the protein might “gate” this solvent organization is an open question.

CHAPTER 5. FUTURE DIRECTIONS: PRELIMINARY STUDIES ON THE PHM COPPER-OXYGEN INTERMEDIATE

5.1 Introduction

Peptidylglycine α-hydroxylating monooxygenase (PHM) participates in the bioactivation of peptides by amidation. These amidated peptides serve as signaling molecules in various endocrine pathways [133][134][69][35][125][135]. Amidation takes place in two sequential steps. The first step, hydroxylation, is catalyzed by PHM [127][182][138]. The resulting carbinolamide intermediate undergoes dealkylation, catalyzed by peptidylglycine α-amidating lyase (PAL), to yield an amidated peptide and glyoxalate as a byproduct [126][122]. The schematic representation of the reaction is given in the Figure 5-1. Structurally PHM possesses two domains [62], each housing a copper center [139][140], separated by a 11 Å water-filled cleft [67][62][69]. The copper centers, termed, CuH and CuM, serve distinct functions during the course of the catalytic cycle of PHM [63][130]. The CuM serves as the oxygen binding and catalytic site [142], while the CuH serves as the electron transfer site [37][132][144][145][125][183]. The CuH site is ligated to three histidines (H107, H108 and H172), whereas, CuM is ligated to two histidines (H242, H244) and the sulfur of methionine (M314) [67][62][69].

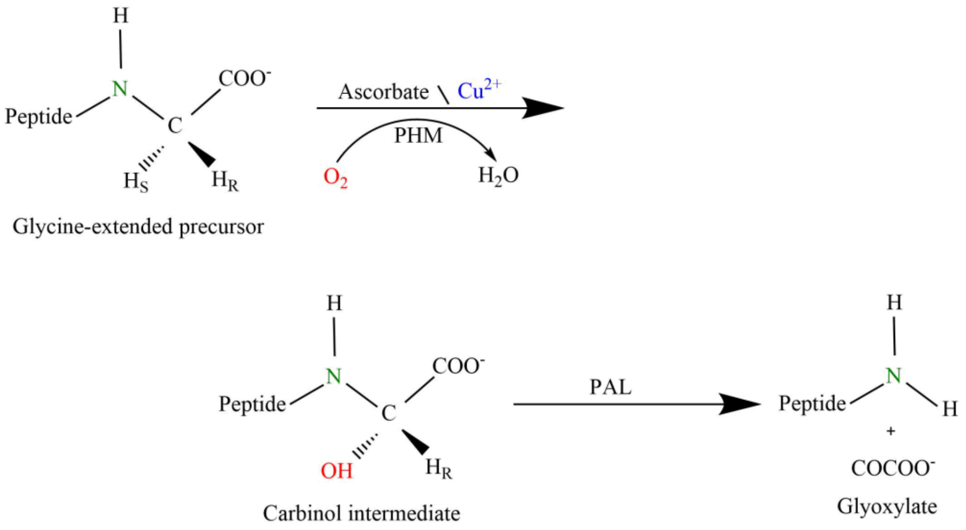

Figure 5-1 *Two-step amidation reaction catalyzed by peptidyl amidating monooxygenase (PAM).*

The catalytic cycle is initiated by reduction of both the copper sites by the physiological reductant ascorbate [146][148][147]. This is succeeded by the equilibrium ordered binding of substrate near the CuM-site, followed by the binding of oxygen to the CuM-site[184][49]. The bound oxygen accepts an electron from the Cu(I)M-site and is envisaged to form a superoxo intermediate [37][132][144][150][152]. This Cu(II)M-superoxo intermediate harnesses enough energy to abstract a hydrogen atom [185][153], leading to formation of a Cu(II)M-hydroperoxo intermediate and a substrate radical. Preceded by an electron transfer from the CuH to the CuM-site, the final stage involves the lysis of the O-OH bond, culminating in transfer of the hydroxyl group to the substrate radical [186].

Although the PHM reaction mechanism has been studied in detail some aspects of it remain elusive. One of the important debates has been about the nature of the

Cu(II)M-oxygen intermediate. It has been suggested through kinetic isotopic studies, DFT calculations, and study of intermediates in other homologues of PHM, that the Cu(II)M-superoxide is the intermediate species [182][184]. A significant step in this direction has been the crystal structure of PHM and the slow substrate, diiodo-tyrosine-threonine (IYT), with oxygen, which showed oxygen bound in an end-on fashion to the CuM-site [69] (Figure 1-7).

Many model complexes of the copper superoxo intermediates have been studied [187][88][95][138][91]. There has been a renewed interest in the copper(II) superoxide complexes since they have been speculated to be the reaction intermediates of not just PHM but dopamine β-monooxygenase, tyramine β-monooxygenase, galactose oxidase, copper amine oxidase, and recently the lytic polysaccharide monooxygenases [186][74][75][76].

In this chapter we present research conducted to isolate the PHM CuM (II) oxygen intermediate in order to characterize and study it in detail. Azide, a structural analog of oxygen, was chosen as the reporter ligand for the Cu(II) state of the Cu(II)M-site. Crystallography data had showed that the azide bound exclusively to the CuM-site [134]. A study of azide binding studies was conducted with WT PHM and its various mutants to determine the K_d. Surprisingly, our results showed that azide bound only to the CuH-site and exhibited no interaction with the CuM-site. Azide exhibited weak binding to H107A and H108A mutants. Intriguingly, the H172A mutant showed no interaction with azide.

The experiment to detect and trap the Cu(II)M-oxygen intermediate was conducted by using various approaches. The successful ones are presented here. The first consisted of a novel enzyme system, chlorite dismutase (Cld), and sodium chlorite. This enzyme system has been used to trap metal-oxygen intermediates in other enzyme reactions [188]. A stopped-flow study, using this system at 4^{o} C, was successful in detecting the first trace of a Cu(II)M-oxygen intermediate in PHM. The trace of the Cu(II)-oxygen intermediate was also observed when the reduced enzyme, in the presence of azide, was exposed to oxygen in stopped-flow studies. Another approach using the PHM substrate, 4-phenyl-3-butanoic acid (PBA), was also successful in detecting the Cu(II)M-oxygen intermediate. We speculate that the copper oxygen intermediate being detected is the Cu(II)M-peroxo species. However many questions remain unanswered and future experiments to probe the matter further are discussed.

5.2 Materials and Methods

Buffers, ascorbate, sodium chlorite, sodium azide, hippuric acid and 4-phenyl-3-butanoic acid were obtained from Sigma-Aldrich at minimum purity of 99%. Ac-Tyr-Val-Gly (Ac-YVG) was purchased from Peptide international.

5.2.1 PHM Expression and Purification

WT PHM catalytic core (PHMcc, residues 42-356) and its variants H107A, H172A and H242A were constructed as described previously [62]. The construction of the PHM mutants, H108A and H107AH108A, has been described in [68]. The stably transfected cell lines were thawed from freezer stock into a T75 flask with 20 mL of DMEM/F12 medium containing 10% FCII serum (Fisher). At 80% confluence, the cells were passed into five NUNC triple flasks (500 cm^2 per flask) which were also grown to confluence. The cells were trypsinized and resuspended in 50 mL DMEM/F12 medium with 10% FCII serum prior to inoculation into the extra-capillary space (ECS) of a Hollow Fiber Bioreactor (Fibercell Systems 4300-C2008, MWCO 5 kDa, 3000 cm^2 surface area) pre-cultured with 2 L of 50 mM PBS pH 7.35 and 2 L of DMEM/F12 10% FCII serum [66][122][143].

Individual bioreactors containing each of the variants were fed with DMEM/F12/10% FCII serum for a month. The serum level was then reduced to 0.5%, at which point spent medium (20 mL) from the ECS was collected every other day and frozen at -20^{o} C for later purification. About a month worth of the bioreactor harvest (300 mL) for each variant was purified as previously described [66][122][143].

5.2.2 PHM Copper Reconstitution

The purified enzyme was dialyzed against 20 mM sodium phosphate buffer (pH 8.0) and then reconstituted with 2.5 equivalents of cupric sulfate per protein, followed by two cycles of dialysis to remove the unbound cupric ions. This procedure was followed for WT PHM, H107A, H108A and H172A mutant. For the single-site variants (H107AH108A and H242A), the purified protein was initially dialyzed against 20 mM sodium phosphate buffer (pH 8.0) overnight, reconstituted with 2.5 equivalents of cupric sulfate using a syringe pump, at a rate of 60 µL/hr, and dialyzed exhaustively against copper-free phosphate buffer at the same pH and ionic strength. This procedure resulted in copper:protein ratios close to 1. Thereafter, the single-site mutants were reconstituted with 1.3 equivalents of cupric sulfate, and dialyzed overnight against 20 mM sodium phosphate buffer (pH 8.). Protein concentration was determined by O.D$_{280}$ on a Cary-50 UV-vis spectrophotometer at room temperature using an extinction coefficient for a 1% solution at 280 nm of 0.980. The copper concentrations were determined using a Perkin-Elmer Optima 2000 DV inductively coupled plasma optical emission spectrometer (ICP-OES).

5.2.3 Specific Activity Measurements

The enzymatic activity was measured by monitoring oxygen consumption in a Rank Brothers Oxygen Electrode at 37^{o} C as previously reported [66][122][67][68][143]. The reaction was performed in a water-jacketed cell maintained at 37^{o} C. The mixture (2 mL) contained 100 mM MES pH 5.5, 200 µL of 6 mg/mL catalase solution (47,000 units/mg), 5 µM cupric sulfate solution, 10 mM ascorbate and 80 µM dansyl-YVG substrate. The reaction mixture was allowed to equilibrate for 1 minute after which it was capped and a baseline was measured for 50 s. The reaction was then initiated by adding 10 – 50 µL of enzyme (depending on the mutant), through the cap of the reaction vessel with a 50 µL Hamilton syringe. The enzyme concentration for mutants was varied from 100 µM to 350 µM.

5.2.4 DaCld Production and Reconstitution

The plasmid with cld gene was kindly provided to us by Dr John Lipscomb (University of Minnesota). The plasmid was transformed into competent *Escherichia coli* BL21 (λDE3). The *Escherichia coli* BL21 (λDE3) containing the *cld trx-his$_6$-tev* plasmid were grown from a freshly streaked plate into LB media containing 100 µg/mL ampicillin at 37^{o} C until they reached an O.D$_{600}$ of 0.8, at which point protein production was induced with 0.4 mM isopropyl β-D-1-thiogalactopyranoside. Growth was allowed to continue at 37^{o} C for 4 h, whereupon the cells were harvested by centrifugation and pelleted. The cells were resuspended, lysed using the French pressure method, and centrifuged to remove the cell debris. The filtered supernatant was poured over a Ni-NTA resin column, rinsed with buffer, and eluted using a 250 mM imidazole buffer rinse. To remove the His$_6$-Trx tag, tobacco etch virus (TEV) protease and 5 mM β-mercaptoethanol were added to the protein solution, and the mixture was incubated at 20^{o} C overnight. After a round of dialysis, the protein solution was once again poured over a Ni-NTA resin column to yield cleaved, pure apo DaCld. SDS-PAGE gel analysis of the purified protein showed the final product to be in a single band at the appropriate weight (31 kDa) with no visible impurities. The purified enzyme was stored in Na-P buffer (50 mM, pH 8) for subsequent metalation steps.

5.2.5 DaCld Reconstitution with Iron

The hemin stock solution (125 µM) was prepared by dissolving hemin in 10 mM NaOH solution. Freshly prepared hemin was then added to the Da-Cld in Na-P buffer (50 mM, pH 8) in aliquots of 2 µL and a UV-vis spectrum was taken. The 2 µL aliquots were added till a Soret peak was observable (417 nm). The hemin was added till the ratio of the Soret peak (417 nm) to protein peak (280 nm) was ~1.8. The reconstituted protein was passed through a desalting column to get rid of excess heme.

5.2.6 Specific Activity of DaCld

The specific activity was determined in a Rank Brothers oxygen electrode. The reaction was performed in a water-jacketed cell maintained at 4^{o} C. Na-P buffer (50 mM, pH 8) was taken in a water jacketed cell to which Da-Cld was added (final concentration = 2.2 µM) and (417 nm/280 nm = 1.8). The reaction mixture was allowed to equilibrate for 1 minute after which it was capped and a baseline was measured for 50 s. The reaction was initiated by adding 10 µL of 50 mM sodium chlorite (final concentration 250 µM) through the cap of the reaction vessel with a 50 µL Hamilton syringe. The final volume of the reaction mixture was 2 mL. The calculated specific activity was 19, 600 µM/mg.s.

5.2.7 Azide Titration UV-vis

The WT PHM was diluted with Na-P buffer (50 mM, pH 8.0) to a final concentration of 500 µM and final volume of 1250 µL in a quartz cuvette with a micro flea magnetic stir bar. The Starna 'Spinette' electronic cell stirrer was placed at the base of the sample holder of the Cary-50 UV-vis spectrophotometer and the cuvette containing the PHM solution was placed on it. The azide stock solution (2M) was taken in a 100 µL Hamilton syringe and set on a KDS model 100 series syringe pump. The capillary tube attached to the syringe, containing the azide solution, was very carefully inserted into the cuvette containing the PHM solution away from the path of the UV-vis radiation. The azide was pumped into the PHM solution at a rate of 100 µL/hr and the data was gathered for 61 minutes at a scan rate of 0.00125 min/nm. The increase in absorbance was recorded between the wavelength ranges of 300 nm-500 nm. The data was processed in SigmaPlot 12.and fit to a two-site saturation binding equation (5-1) for the WT PHM, H108A and H242A, and single-site saturation binding equation (5-2) for H107A, respectively.

$$f = \frac{B_{max1} * abs(x)}{(K_{d1} + abs(x))} + \frac{B_{max2} * abs(x)}{(K_{d2} + abs(x))} \tag{5-1}$$

$$f = \frac{B_{max} * Abs(x)}{(K_d + abs(x))} \tag{5-2}$$

Where, B_{max1} and B_{max2} are the amplitudes and K_{d1} and K_{d2} are the dissociation rate constants.

5.2.8 Stopped Flow with Azide as a Reporter Agent

The WT PHM sample was concentrated in an Amicon filter (10,000 MWCO) to a volume of 50 µL (~2 mM) and purged under a gentle stream of CO gas for 5 minutes before addition of a 5-fold excess (5 mM) of anaerobic buffered ascorbate. The reduced WT PHM mixture was then incubated under an atmosphere of pure CO for an additional 5 minutes. The reduced PHM-CO complex was moved to the anaerobic chamber and the PHM substrate, Ac-YVG), was added to a final concentration of 100 µM. Anaerobic sodium phosphate buffer (50 mM, pH 8) was added to a final volume of 1 mL and placed in an anaerobic syringe.

Sodium azide stock solution (2M) was diluted to a final concentration of 20mM by adding sodium phosphate buffer (50 mM, pH 8), which was then oxygenated by bubbling pure oxygen through it for 30 minutes. The diluted and oxygenated sodium azide solution was loaded in a syringe and moved into the anaerobic chamber.

The reduced carbonylated PHM was shot against oxygenated sodium azide solution and the data was recorded up to 10 s. The stopped-flow experiments were conducted on a SX20 Applied Photophysics stopped-flow instrument maintained at 4° C and enclosed in a Vacuum Atmospheres anaerobic chamber with oxygen levels of ≤ 1 ppm. The syringes used for the experiment were made anaerobic by overnight storage in the anaerobic chamber. The experimental data points were fit to a single exponential decay equation (5-3). Where, *a* is the amplitude and *b* is the rate constant.

$$f = ae^{-bx} \tag{5-3}$$

5.2.9 Stopped flow of WT PHM with the DaCld Enzyme System

The WT PHM sample was concentrated in an Amicon filter (10,000 MWCO) to a volume of 70 µL (1 mM) and purged under a gentle stream of CO gas for 5 minutes before addition of a 5-fold excess (5 mM) of anaerobic buffered ascorbate. The reduced WT PHM-CO complex was then incubated under an atmosphere of pure CO for an additional 5 minutes. The carbonylated WT PHM sample was taken to the anaerobic chamber and argon purged Da-Cld (final concentration = 720 µM) and the PHM substrate hippuric acid (final concentration = 240 µM) were added to it. The PHM, DaCld and substrate mixture was diluted with argon-purged KH_2PO_4 buffer (100mM, pH 8), (final concentration of WT PHM = 720 µM). Argon purged sodium chlorite (stock solution = 50 mM) was taken and diluted with argon purged Na-P buffer (50 mM, pH 8) to a concentration of 10 mM (final concentration = 5 mM).

Stopped-flow experiments were conducted under anaerobic conditions at 4° C on a SX20 Applied Photophysics stopped-flow instrument enclosed in a Vacuum Atmospheres anaerobic chamber with oxygen levels of ≤ 1 ppm. The data were recorded up to 10 seconds. The syringes, argon-purged deionized water and buffer were made anaerobic by overnight storage in the anaerobic chamber. The experimental data points were fit to a single exponential decay equation (5-3). Where, *a* is the amplitude and *b* is the rate constant.

$$f = ae^{-bx} \tag{5-4}$$

5.3 Results

5.3.1 Azide Binding Affinity Studies

5.3.1.1 WT PHM

Figure 5-2 shows the results of the binding studies conducted for determining the affinity of azide (the reporter ligand) to the WT PHM (receptor). Azide is known to bind copper and generate a copper azido complex, which exhibits strong absorbance at 390 nm (ε = 1800 $M^{-1}cm^{-1}$). The absorption occurs due to the phenomenon of ligand-to-metal charge transfer (LMCT) transitions from the π-orbital of azide to the empty d-orbital of the Cu(II) metal. The experimental conditions were optimized by adding about 500 µM of the WT PHM for better signal to noise ratio and by conducting the experiment at pH 8. This ensured that the protein remained soluble during the course of the experiment.

To obtain the K_d values, the data were fit to a two-site saturation binding equation. The K_d values indicated that the azide does not bind tightly to the copper in WT PHM. Two different K_d values were obtained, with one being around 60 times stronger than the other (Table 5-1). However, these data do not reveal whether the CuM and CuH-sites bind an azide anion each, or whether the two azide anions bind any one of the CuM and CuH-sites. Since crystallography had shown previously that an azide anion bound to the CuM-site of WT PHM exclusively [69], it was assumed that both the binding events were taking place at the CuM-site.

Sample	**WT PHM**	**H242A**	**H108A**	**H107A**	**H242A**
Binding	Two site	Two site	Two site	Single site	Single site
B_{max1}	0.43	0.31	0.62	1.07	0.65
K_{d1} (μM)	1097.93	8059.71	4233.96	70485.71	25452.28
B_{max2}	1.30	0.60	1.12		
K_{d2} (μM)	65549.31	149762.42	61662.89		

Table 5-1 *The table presents the B_{max} and the K_d values of WT PHM and its various mutants. The H242A mutant (CuH-site only) experimental data points were fit to both single and double-site saturation binding equation.*

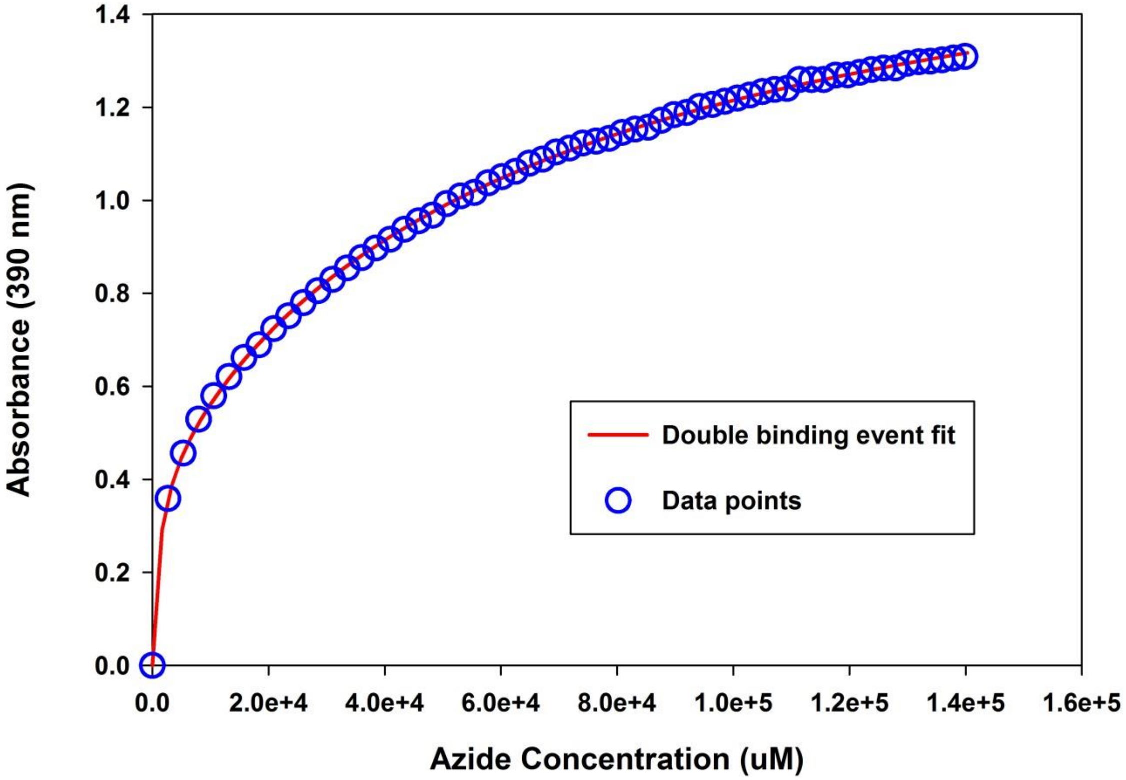

Figure 5-2 *Titration curve of WT PHM with azide. The circles represent experimental data points and the solid line is the fit to two-site saturation binding equation.*

5.3.1.2 H242A (CuH-site only Mutant)

Since the crystallography data showed that only the CuM-site was able to interact with azide, the H242A mutant was used as a control. Figure 5-3 shows the results of the titration. Surprisingly, the results show interaction between azide and the CuH-site. This is not in accordance with the previously reported crystallography data [134]. The data fit well to two-site saturation binding equation ($R^2 = 0.99$). The values of K_d are listed in Table 5-1. Both the strong and weak binding K_d's are about 8 and 2 times weaker, respectively, compared to the WT PHM.

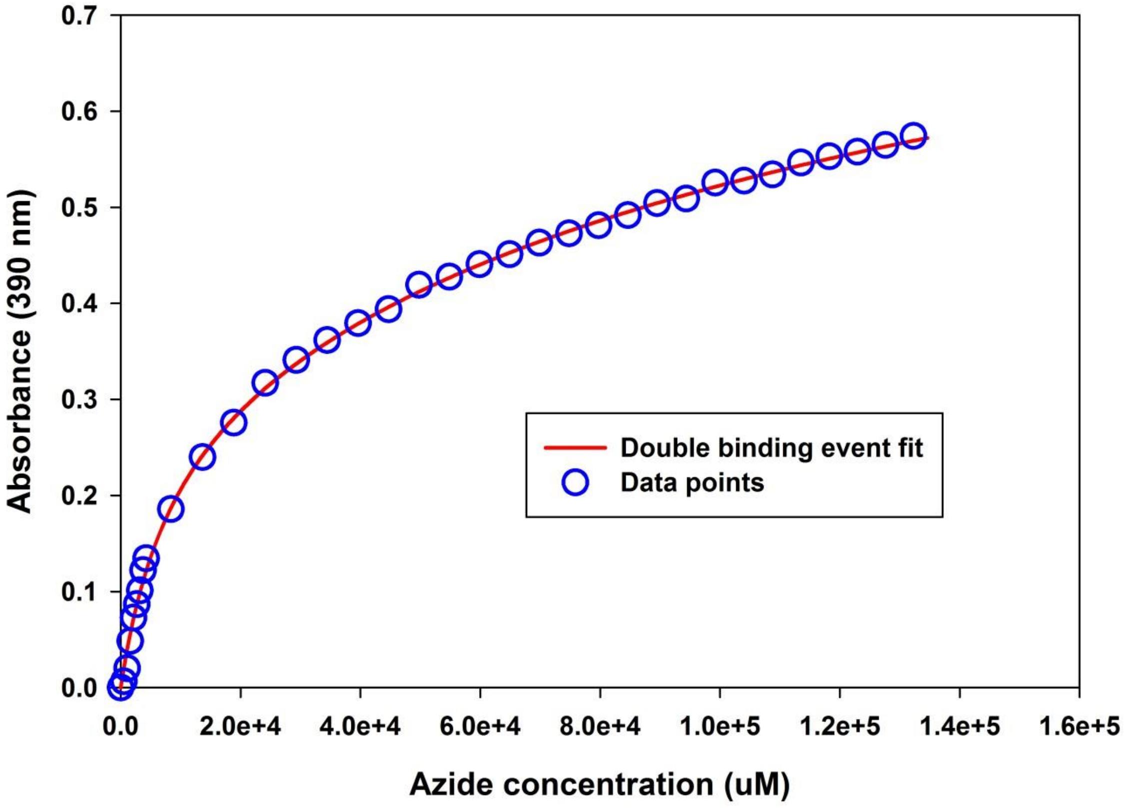

Figure 5-3 *Titration curve of H242A with azide. The circles represent the experimental data points and the solid line is the fit to a two-site saturation binding equation.*

5.3.1.3 H107AH108A (CuM-site only Mutant)

The H107AH108A (CuM-site only) was the next mutant to be studied. Since it was known that azide anion bound to the CuM-site [69], the H107AH108A mutant titration curve was expected to be a parabola. The data were also expected to fit to a two-site saturation binding equation. However, the H107AH108A mutant failed to show any interaction with azide (data not shown). Despite repeating the experiment with increased concentration of the enzyme (900μM), no interaction was observed. There is a possibility that the mutation of the two histidine ligands (H107 and H108) to alanine in the CuH-site, affects the secondary protein structure, which in turn affects the CuM-site. However, in a previous publication [68] EPR, FTIR and XAS studies on the H107AH108A mutant have shown that the structure, geometry and the binding properties of the CuM-site are not affected. Thus this result agrees with the inference that azide interacts exclusively with the CuH-site.

5.3.1.4 H107A

To probe the significance of the H-site ligands on the azide binding, a titration was performed with H107A, H108A and the H172A mutants. All the three histidines are very important for the catalytic activity of the PHM [67]. Structurally, the substitution of histidines by alanine, in the CuH-site, has not been found to affect the binding of copper. It is speculated that the substituted histidine is either replaced by a solvent or by the main chain amide O group, resulting in very little changes in coordination geometry [67]. These changes were expected to reflect in the values of the K_d.

The titration curve of H107A is shown in Figure 5-4. The data fit poorly to a two-site saturation binding equation ($R^2 = 0.82$), but the fit to a single-site saturation binding equation was good ($R^2 = 0.99$). The value of K_d (Table 5-1) showed that the azide binding was weak. It is plausible that the histidine to alanine substitution makes the CuH-site less positive overall, affecting the binding of azide (negatively charged) and resulting in only one azide anion binding to the CuH-site.

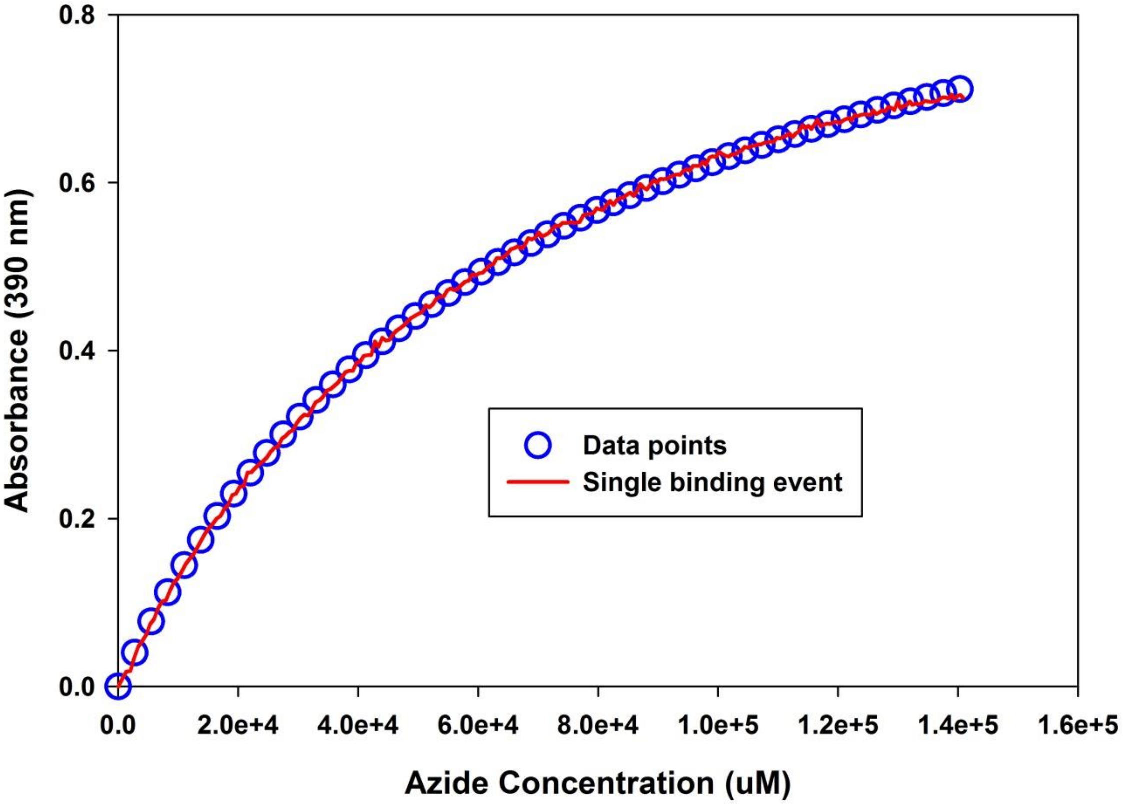

Figure 5-4 *Titration curve of H107A with azide. The circles represent the experimental data points and the solid line is the fit to single-site saturation binding equation.*

5.3.1.5 H108A

The binding curve of the H108A mutant is shown in Figure 5-5. The data fit well to a two-site saturation binding equation (R^2=0.99). Although the result shows similarity in the behavior of H108A and WT PHM towards azide, the values of K_d are not comparable (Table 5-1). The first binding event, also the stronger binding event of the two, is 6 times weaker. The second binding K_d value is 2 times weaker. The weaker binding compared to the WT PHMcould be an outcome of slight changes in the coordination geometry and/or reduction potential of the CuH-site. Further studies are required to shed more light on this matter.

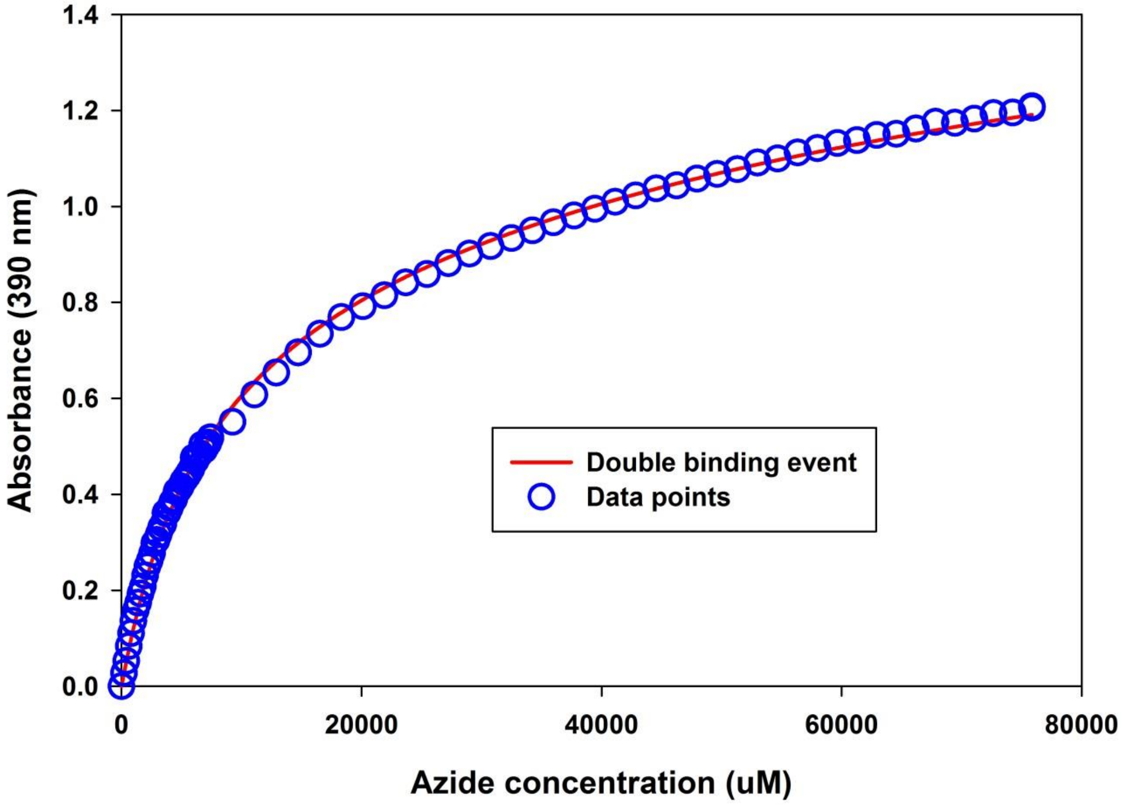

Figure 5-5 *Titration curve of H108A with azide. The circles represent the experimental data points and the solid line is the fit to a double-site saturation binding equation.*

5.3.1.6 H172A

The H172A showed no interaction with azide. This was an intriguing result. In order to get a better signal to noise ratio, the experiment was repeated with an increased concentration of enzyme (800 µM). However, no interaction with the azide was observed (data not shown). It has been shown by cyclic voltammetry studies that the H172A mutant is unstable and prone to denaturation [183]. Even if that were the case, the azide concentration was high enough to interact with the unbound copper from the H172A and should have resulted in a linear graph. Since no such interaction was observed, it can be assumed that the copper remained bound to the copper sites of the H172A mutant but failed to bind azide.

5.3.2 Stopped-Flow Experiments Conducted to Detect and Trap the CuM-Superoxo Intermediate

In an attempt to trap the CuM-oxygen intermediate in traceable amounts, various reporter agents and enzyme systems were explored. Different approaches were followed when designing the experiment. Each approach afforded some advantage in favoring the build-up of the CuM-oxygen intermediate. However, only three were successful. The results from these different systems and the reasoning behind the experimental designs are presented in the following sections.

5.3.2.1 Chlorite Dismutase-Sodium Chlorite System

The chlorite dismutase system can generate up to 10mM oxygen by dismutation of sodium chlorite in less than 2 ms [188], making it an ideal system for generating large amounts of oxygen within the mixing time of the stopped-flow instrument. The main objective was to build up the Cu(II)M-oxygen intermediate in detectable amounts. This was achieved by using three measures. Firstly, the concentration of one of the reactants (oxygen) was increased to high levels to move the equilibrium of the reaction towards the right side of the equation (5-5).

$$\mathrm{Cu(I)M} + \mathrm{O_2} \leftrightarrow \mathrm{Cu(II)M} - \mathrm{O_2^-} \qquad (5\text{-}5)$$

Secondly, the formation of the Cu(II)M-oxygen intermediate was delayed so that the reaction would not be over within the mixing time of the stopped-flow instrument. This was achieved by carbonylating the CuM-site. The carbon monoxide forms an adduct with the Cu(I)M-site by two bonding interactions with the copper: a two electron donation from the lone pair on the carbon of CO to the vacant d-orbital and the interaction of the filled metal d-orbital with the empty π*-orbital of the carbon monoxide ligand. Since the CO forms an adduct with the CuM-site, the oxygen can only bind to the CuM-site after displacing CO. This delays the formation of the CuM-oxygen intermediate, ruling out the possibility of formation and disintegration of the intermediate during the dead time of the stopped-flow instrument and increasing the probability of observing the intermediate. Finally, the Cu(II)M-oxygen intermediate was stabilized by decreasing the rate of its dissociation. This was achieved by conducting the experiment at 4° C and by use of a slow substrate (4-phenyl-3-butanoic acid).

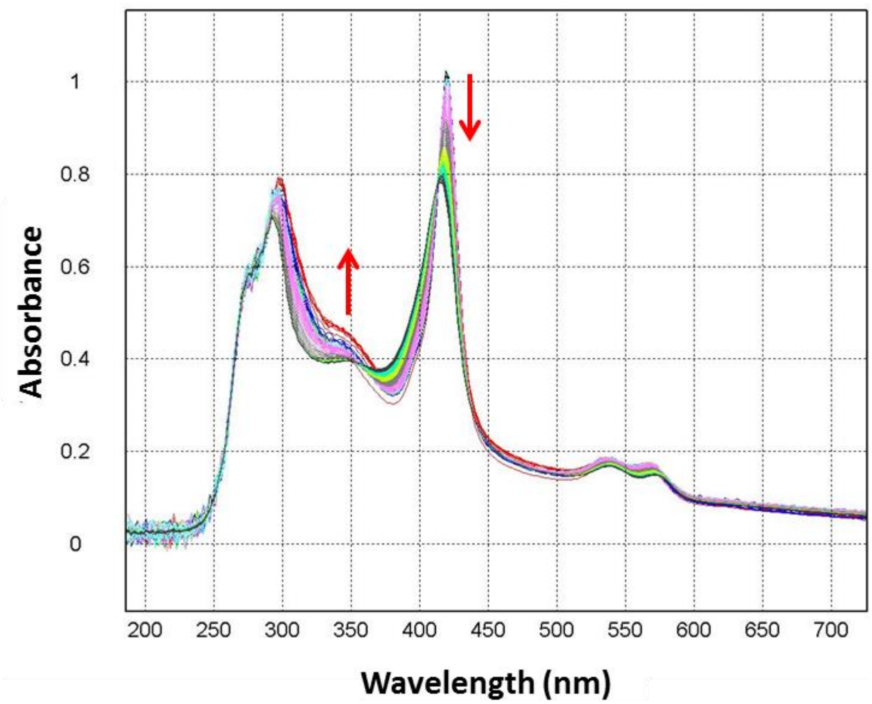

Figure 5-6 *Kinetic traces of the WT PHM in the presence of the substrate (hippuric acid) and oxygen.*

Figure 5-6 shows the kinetic traces of reduced WT PHM, chlorite dismutase and PHM substrate (hippuric acid), when shot against the potassium phosphate buffer containing sodium chlorite at 4^{o} C. Besides the Soret peak of the heme protein, DaCld, at 410 nm and the α, β bands (530 nm and 570 nm), another species appears to be absorbing near the isosbestic point at 350 nm.

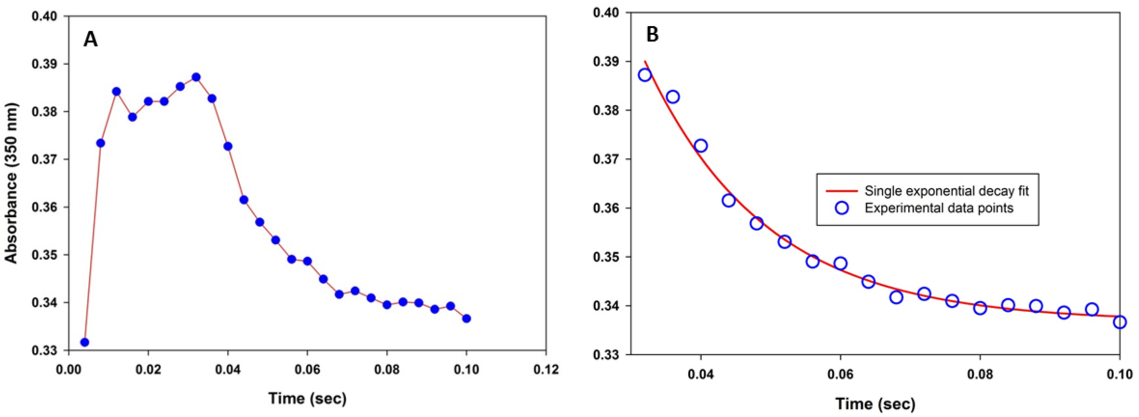

Figure 5-7 *kinetic traces of WT PHM in the presence of the substrate (hippuric acid) and oxygen. A) change in absorbance of the 350 nm trace plotted against time. B) The single exponential decay fit (solid red line) to the experimental data points (open blue circles)*

Figure 5-7 shows the absorbance at 350 nm plotted against time, after adjusting out the offset. The absorbance is observed to increase for the first 10 ms. Thereafter, it remains constant from 10 to 30 ms before finally decaying. This indicates that the absorbing species formed during the course of reaction, builds up and remains stable for some time before disintegrating.

Klinman and coworkers analyzed the individual steps of the PHM mechanism using kinetic isotope approaches [170]. In particular, they calculated a rate constant for hydroxylation of substrate after the enzyme had committed to catalysis. The value of this rate constant at 25^{o} C was 1330 s^{-1} and was a composite of all chemical steps subsequent to formation of the superoxide intermediate and prior to product release. The rate constant obtained in the present study (57.8 s^{-1}) corresponds to the decay of one intermediate along the pathway and was measured at the lower temperature of 4^{o} C and is therefore not directly comparable. However the value is not inconsistent with expectations given the differences in reaction conditions. Based on the wavelength of absorption [189], it may be inferred that the absorbing species is Cu(II)M-peroxide intermediate.

Figure 5-8 shows the control experiment, performed under the same conditions, without the substrate hippuric acid (HA). The absorbing species observed in Figure 5-6 is not seen in Figure 5-8. The result is in good agreement with the PHM reaction mechanism. The copper-oxygen intermediate is only formed when the substrate is present to avoid formation of deleterious reactive oxygen species, which can cause damage to the cell. Thus, the results strongly suggest that the species absorbing at 350 nm is indeed a Cu(II)M-peroxide intermediate.

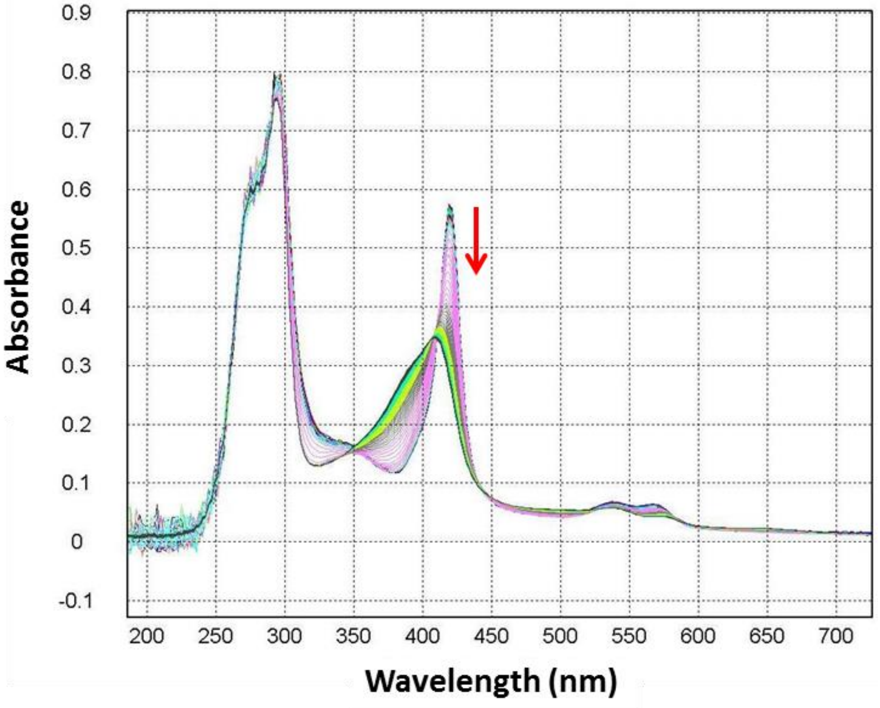

Figure 5-8 *Kinetic traces of WT PHM and oxygen in absence of the substrate.*

5.3.2.2 WT PHM with Azide in Oxygenated Buffer

Azide is a structural analog of oxygen and was used as a reporter agent for the stopped-flow experiments. Although the stopped flow experiments were performed with the aim of determining the rate of reoxidation of the CuH-site, an increase in absorbance around 350 nm was observed (Figure 5-9). The increase in absorbance around 350 nm was detected in the other PHM mutants, H108A and H107A, as well (data not shown). However, it was most prominent in the case of WT PHM. Figure 5-10 shows the change in absorbance of the 350 nm trace plotted against time, after adjusting out the offset. The data were fit to a single exponential equation and a decay rate constant of 0.42 s^{-1} was obtained. The value of the rate constant is much lower than determined by oxygen burst chemistry in the absence of azide. It is possible that azide binding to the Cu(I) form of the CuH-site slows the second electron transfer, resulting in the reduced decay rate of the species absorbing at 350 nm.

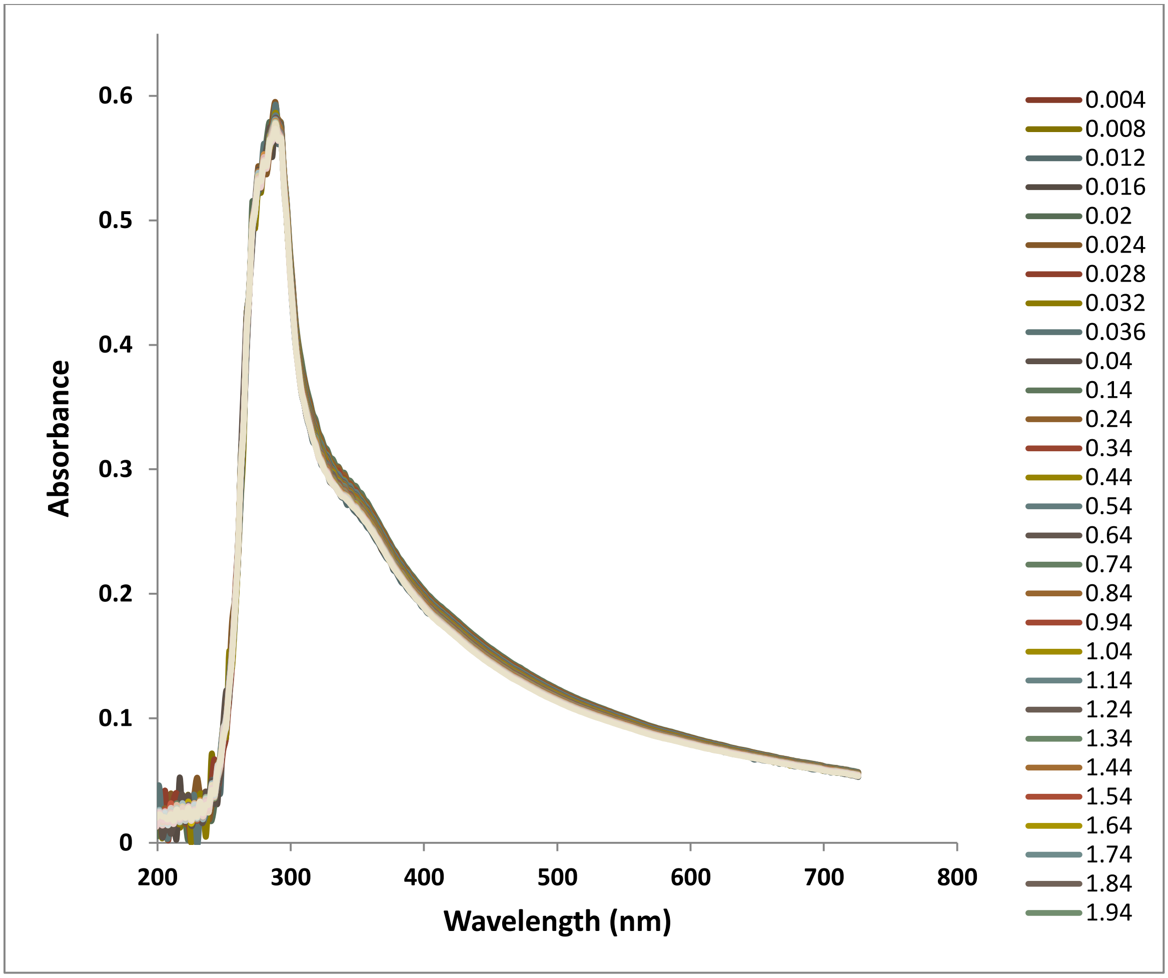

Figure 5-9 *Kinetic traces of WT PHM shot against azide (25mM) in the presence of the substrate (Ac-YVG).*

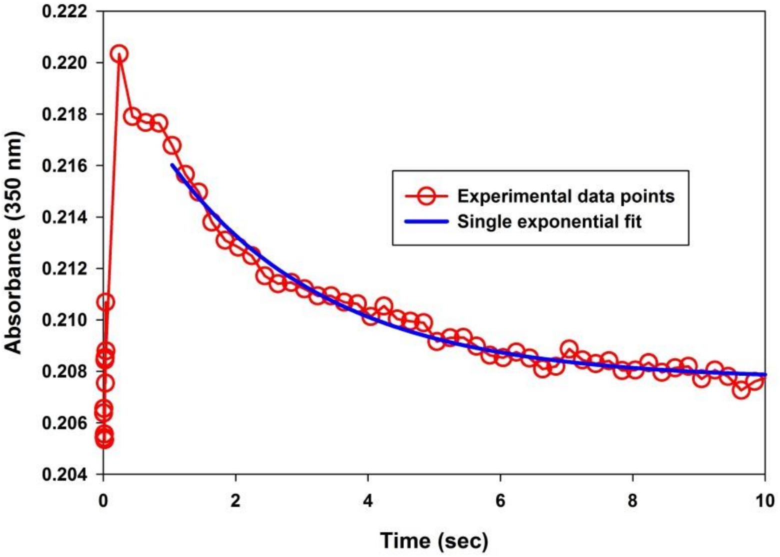

Figure 5-10 *Kinetic (350 nm) trace of WT PHM shot against azide (25mM) in the presence of the substrate (Ac-YVG). Experimental data points are shown in red and the single exponential decay fit is shown in blue.*

5.3.2.3 WT PHM with Substrate 4-Phenyl-3-butanoic acid and Azide in Oxygenated Buffer

PBA (4-phenyl-3-butenoic acid) is a potent mechanism-based inhibitor of PHM [190][191][192]. It is believed that inhibition occurs through formation of a stable delocalized radical, as shown in the Figure 5-11.

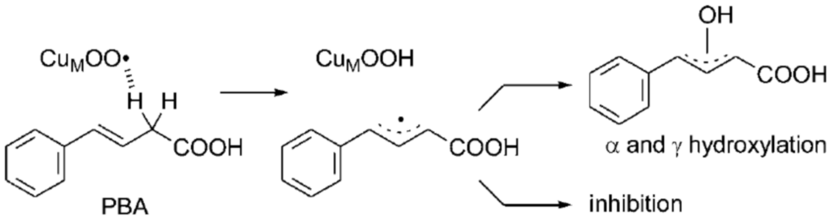

Figure 5-11 *Mechanism based inhibition of PHM by the substrate 4-phenyl-3-butanoic acid. Reprinted with permission from Langella et al. (ChemMedChem, 2010, 5(9). Copyright (2010) WILEY-VCH Verlag GmbH & Co. KGaA, Weinheim.*

Although no covalent adduct has been observed so far, the delocalized radical is believed to form a covalent bond with the amino acid residues in the catalytic site of the PHM, causing irreversible damage and inactivation [193]. Since the delocalized radical formation occurs right after the hydrogen abstraction step, very little or no substrate is available for hydroxylation. It appears that this phenomenon provides an opportunity for the build-up of the Cu(II)M-oxygen intermediate. The graph from the stopped-flow experiment conducted with reduced carbonylated PHM, PBA and azide is shown in Figure 5-12. As mentioned previously, azide was used in the experiment to increase the chances of build-up of the Cu(II)M-peroxo intermediate.

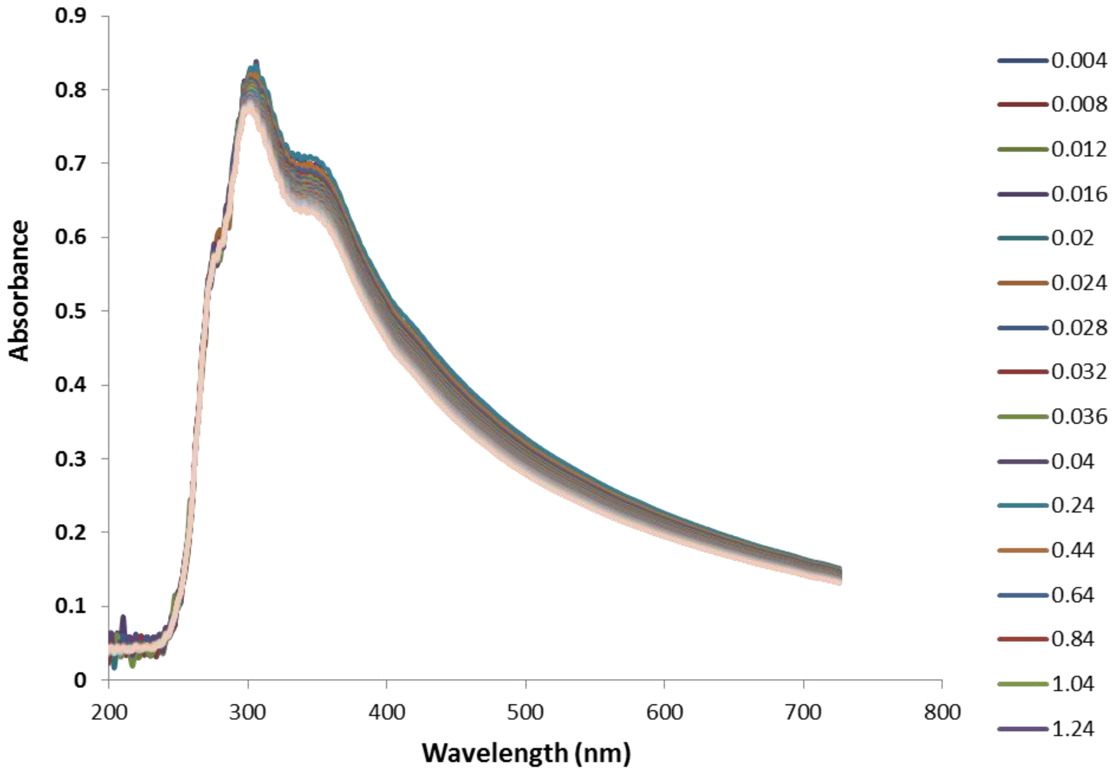

Figure 5-12 *Kinetic traces of WT PHM against azide in oxygenated buffer, in the presence of 4-phenyl-3-butanoic acid.*

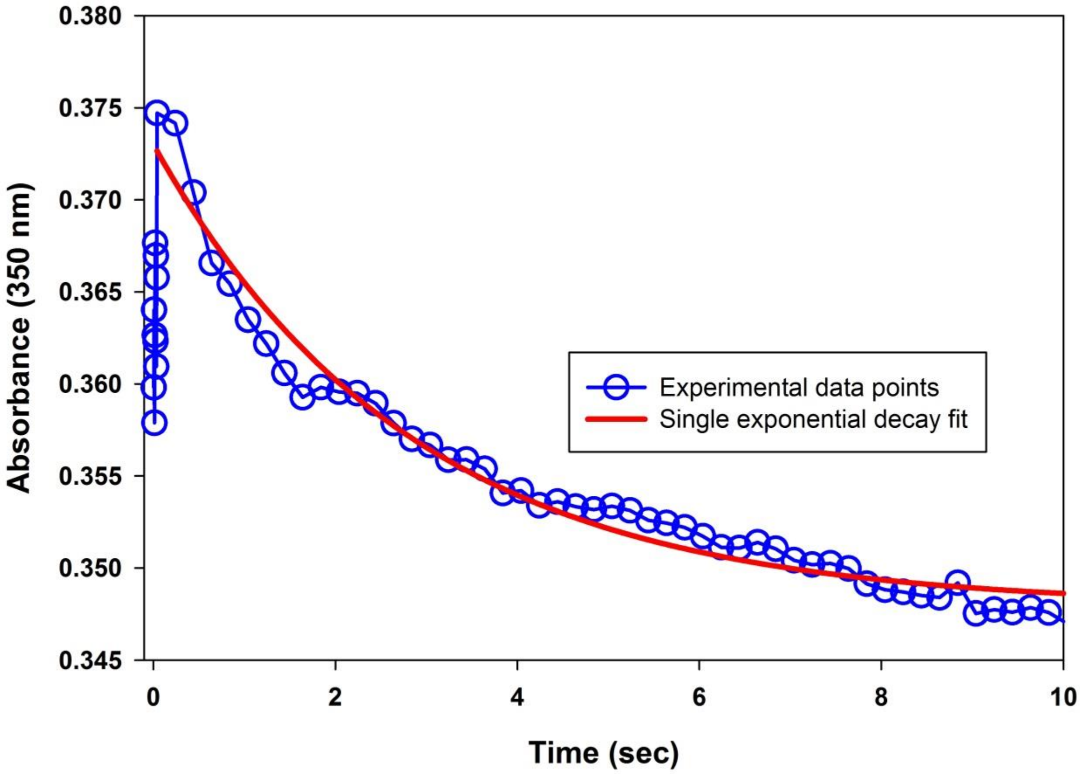

Figure 5-13 *Kinetic (350 nm) trace of WT PHM against azide in oxygenated buffer, in the presence of 4-phenyl-3-butanoic acid. Experimental data points are shown in blue and the single exponential decay fit is shown in red.*

It is seen in Figure 5-12 that there are changes in absorbance around 350 nm and 400 nm. The change in absorbance at 350 nm with time after adjusting out the offset, is plotted in Figure 5-13. The decay rate constant is 0.36 s^{-1}. The observed decay constant is remarkably similar to that determined from the reaction of carbonylated reduced PHM with oxygen in the presence of azide (Figure 5-10, 42 s^{-1}), suggesting the decay of identical species in each case.

5.4 Discussion and Summary

The copper-oxygen complexes such as the superoxides and peroxides play a very important role in various biological systems and also in several copper-catalyzed oxidation reactions in synthetic chemistry [71][73]. Figure 5-14 shows the possible pathways for generation of the superoxide and peroxide complexes.

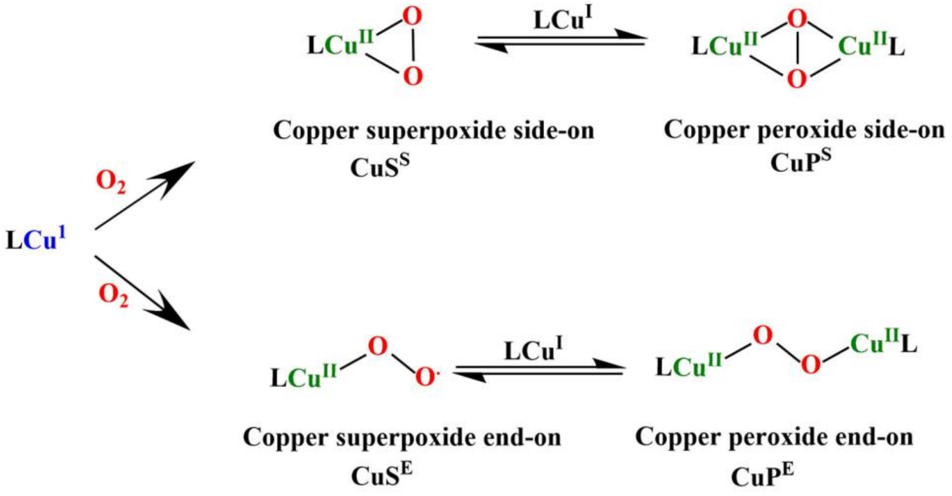

Figure 5-14 *Reaction pathways for the generation of copper superoxide and peroxide complexes.*

The mononuclear copper (II) superoxide complexes have received special attention lately due to their role as the reaction intermediates in several copper monooxygenases [186][74][75][76].

Since the publication of the crystal structure of PHM with oxygen [69], the emphasis has been on studying the end-on copper-superoxide complexes (CuS^{E}). The CuS^{E} complexes in the biological enzymatic system have been found to be four-coordinate and possessing tetrahedral geometry. Initially, only pentacoordinate, trigonal pyrimidal and square planar CuS^E complexes were isolated [83][84][85][86][87][187], but recently, model complexes mimicking the biological intermediates have been isolated as well [77][95]. It has not been possible to trap and study the CuS^E in the biological systems so far.

This chapter explores the research conducted in a bid to generate and study the Cu(II)M-oxygen intermediate species in PHM. Initial experiments were designed with the objective of determining the rate of reoxidation of the Cu(I)M-site, using azide as a reporter ligand. The binding experiments, conducted with azide in this regard gave unexpected results. In a previous publication, the crystal structure of WT PHM with azide had shown that it bound exclusively to the CuM-site. The presence or absence of substrate had no effect on the binding of azide [134]. Contrary to this, our results showed that in the absence of substrate, the azide bound only to the CuH-site. Despite the high concentration (2M) of azide, the CuM-site only mutant, H107AH108A, failed to show any interaction with it. A previous publication from our lab has shown that the CuM-site in the H107AH108A mutant undergoes no change in coordination or geometry and is comparable to the CuM-site in the WT PHM [68]. Hence, the failure of azide to bind to the CuM-site cannot be attributed to changes in structure or geometry of the CuM-site.

The binding studies performed on H242A, CuH-site only mutant, showed definite interaction with azide. Curve fit results showed that two azide molecules bound to the CuH-site, but with larger values of the dissociation constants. Although the CuH-site remains structurally intact in the H107AH108A mutant, it is possible that the complete loss of the CuM-site leads to a decrease in the overall positive charge and the electrode potential, leading to weaker binding of the azide anion.

The curve fitting results of the CuH-site mutant, H107A and H108A, indicated binding of one azide and two azide anions, respectively. Both mutants exhibited weak azide binding compared to the WT PHM. Although these mutants possess an intact CuM-site, the weak binding could be a reflection of changes in the geometry of the CuH-site or the overall charge of the CuH-site due to the replacement of the histidine ligand with alanine. Cyclic voltammetery studies are required to probe this further. The H172A mutant presented an intriguing result by exhibiting no interaction with azide. The failure to interact with azide in this case can be attributed to either drastic changes in geometry or changes in the overall charge of the CuH-site.

The experiment of trapping the Cu(II)-oxygen intermediate was approached in a number of ways. The first approach was to increase the concentration of one of the reactants, oxygen in this case, to tip the reaction in favor of increased rate of formation of the Cu(II)M-superoxide intermediate. Oxygen has low solubility (1.2mM at 25^{o} C, 1 atm) [194], making it difficult to increase the concentration beyond a certain point. Hence, a novel system capable of generating up to 10mM oxygen, using the heme enzyme ,chlorite dismutase, was used [188]. Another approach used to increase the chances of trapping the Cu(II)M-superoxo intermediate was to decrease its rate of dissociation by conducting the experiment at lower temperatures (4^{o} C). Since data collection on stopped-flow is limited by the dead time (2 ms), there was a chance of the

CuM-oxygen intermediate forming and dissociating within that period. This problem was circumvented by protecting the Cu(I)M-site by forming a Cu(I)M-carbon monoxide adduct. The formation of the Cu(II)M oxygen intermediate is delayed, increasing the probability of its detection.

Species which exhibited an absorbance around 350 nm were detected in three different set of experiments (chlorite dismutase system, oxygenated buffer with azide and use of a suicide inhibitor, which forms a more stable radical species). Various control reactions strongly indicated these absorbing species to be an intermediate of the PHM reaction. In particular, the almost identical rates of decay (~0.4 s^{-1}) of the intermediate species formed in experiments conducted in the presence of azide support the premise that they represent the same species. Several copper-peroxo model complexes have been shown to absorb at 350 nm [189], strongly indicating that the absorbing species could be a Cu(II)M-OOH peroxo intermediate. Further studies with sophisticated techniques like the x-ray emission spectroscopy (XES) will be required to probe the exact nature of the Cu(II)M-oxygen intermediate.

We propose that the detection of Cu(II)M-oxygen intermediate is made possible by the slowing down of the electron transfer from the CuH-site by azide. This stabilizes the Cu(II)M-OOH peroxo intermediate, allowing its detection by stopped-flow. Cyclic voltammatery studies are required to test this hypothesis.

Recently, stopped-flow spectroscopy studies were successful in detecting the mononuclear copper superoxide in the polysaccharide monooxygenases, absorbing at 625 nm [76], giving boost to stopped-flow spectroscopy as a tool, for studying the biological copper-superoxide species. Although we were successful in detecting the Cu(II)M-peroxo intermediate in PHM using different experimental conditions, it has not been possible to characterize it due to its short lived nature. Use of rapid freeze quench EPR (RFQ-EPR) and x-ray emission spectroscopy (XES) are good techniques to use in order to probe this problem. Many questions remain unanswered and future experiments to investigate the matter further are required.

LITERATURE CITED

[1] E. B. De Souza and M. J. Kuhar, "Corticotropin-releasing factor receptors in the pituitary gland and central nervous system: methods and overview.," *Methods Enzymol.*, vol. 124, no. 1948, pp. 560–90, 1986.

[2] A. Tazi, R. Dantzer, M. Le Moal, J. Rivier, W. Vale, and G. F. Koob, "Corticotropin-releasing factor antagonist blocks stress-induced fighting in rats.," *Regul. Pept.*, vol. 18, no. 1, pp. 37–42, 1987.

[3] S. Harvey, "Thyrotrophin-releasing hormone: a growth hormone-releasing factor.," *J. Endocrinol.*, vol. 125, no. 3, pp. 345–358, 1990.

[4] W. Vale, J. Spiess, C. Rivier, and J. Rivier, "Characterization of a 41-residue ovine hypothalamic peptide that stimulates secretion of corticotropin and beta-endorphin.," *Science*, vol. 213, no. 4514, pp. 1394–1397, 1981.

[5] K. Breddam, F. Widmer, and M. Meldal, "Amidation of growth hormone releasing factor (1-29) by serine carboxypeptidase catalysed transpeptidation," *Int. J. Pept. Protein Res.*, vol. 37, no. 2, pp. 153–160, Jan. 2009.

[6] K. Suzuki, K. a Simpson, J. S. Minnion, J. C. Shillito, and S. R. Bloom, “The role of gut hormones and the hypothalamus in appetite regulation.,” *Endocr. J.*, vol. 57, no. 5, pp. 359–372, 2010.

[7] Q. Wang and M. D. Whim, “Stress-induced changes in adrenal neuropeptide y expression are regulated by a negative feedback loop,” *J. Neurochem.*, vol. 125, no. 1, pp. 16–25, 2013.

[8] J. Cornish and I. R. Reid, “Effects of amylin and adrenomedullin on the skeleton.,” *J. Musculoskelet. Neuronal Interact.*, vol. 2, no. 1, pp. 15–24, 2001.

[9] P. H. Taghert, R. S. Hewes, J. H. Park, M. a O’Brien, M. Han, and M. E. Peck, “Multiple amidated neuropeptides are required for normal circadian locomotor rhythms in Drosophila.,” *J. Neurosci.*, vol. 21, no. 17, pp. 6673–6686, 2001.

[10] M. M. B. Ribeiro, A. Pinto, M. Pinto, M. Heras, I. Martins, A. Correia, E. Bardaji, I. Tavares, and M. Castanho, “Inhibition of nociceptive responses after systemic administration of amidated kyotorphin,” *Br. J. Pharmacol.*, vol. 163, no. 5, pp. 964–973, 2011.

[11] V. du Vigneaud, C. Ressler, and S. Trippett, “the Sequence Proposal of Amino Acids in Oxytocin, With a for the Structure of Oxytocin,” *J. Biol. Chem.*, vol. 205, pp. 949–957, 1953.

[12] G. E. Pratt, D. E. Farnsworth, N. R. Siegel, K. F. Fok, and R. Feyereisen, “Identification of an allatostatin from adult Diploptera punctata,” *Biochem. Biophys. Res. Commun.*, vol. 163, no. 3, pp. 1243–1247, Sep. 1989.

[13] B. A. Eipper, S. L. Milgram, E. J. Husten, H. Y. Yun, and R. E. Mains,

"Peptidylglycine alpha-amidating monooxygenase: a multifunctional protein with catalytic, processing, and routing domains.," *Protein Sci.*, vol. 2, no. 4, pp. 489–497, 1993.

[14] J. Fuhlendorff, U. Gether, L. Aakerlund, N. Langeland-Johansen, H. Thøgersen, S. G. Melberg, U. B. Olsen, O. Thastrup, and T. W. Schwartz, "[Leu31, Pro34]neuropeptide Y: a specific Y1 receptor agonist.," *Proc. Natl. Acad. Sci. U. S. A.*, vol. 87, no. 1, pp. 182–186, 1990.

[15] A. S. N. Murthy, H. T. Keutmann, and B. A. Eipper, "Further Characterization of Peptidylglycine α-Amidating Monooxygenase from Bovine Neurointermediate Pituitary," *Mol. Endocrinol.*, vol. 1, no. 4, pp. 290–299, Apr. 1987.

[16] B. A. Eipper, R. E. Mains, and C. C. Glembotski, "Identification in pituitary tissue of a peptide alpha-amidation activity that acts on glycine-extended peptides and requires molecular oxygen, copper, and ascorbic acid.," *Proc. Natl. Acad. Sci. U. S. A.*, vol. 80, no. 16, pp. 5144–8, 1983.

[17] A. Murthy, R. Mains, and B. Eipper, "Purification and characterization of peptidylglycine alpha-amidating monooxygenase from bovine neurointermediate pituitary.," *J. Biol. Chem.*, vol. 261, no. 4, pp. 1815–1822, 1986.

[18] K. Mizuno, K. Ohsuye, Y. Wada, K. Fuchimura, S. Tanaka, and H. Matsuo, "Cloning and sequence of cDNA encoding a peptide C-terminal α-amidating enzyme from," *Biochem. Biophys. Res. Commun.*, vol. 148, no. 2, pp. 546–552, Oct. 1987.

[19] D. Stoffers, L. Ouafik, and B. Eipper, "Characterization of novel mRNAs encoding enzymes involved in peptide alpha-amidation," *J. Biol. Chem.*, vol. 266, no. 3, pp.

1701–1707, Jan. 1991.

[20] A. G. Katopodis, D. Ping, and S. W. May, “A novel enzyme from bovine neurointermediate pituitary catalyzes dealkylation of .alpha.-hydroxyglycine derivatives, thereby functioning sequentially with peptidylglycine .alpha.-amidating monooxygenase in peptide amidation,” *Biochemistry*, vol. 29, no. 26, pp. 6115–6120, Jul. 1990.

[21] J. P. Gilligan, S. J. Lovato, N. M. Mehta, A. H. Bertelsen, A. Y. Jeng, and P. P. Tamburini, “Multiple Forms of Peptidyl α-Amidating Enzyme: Purification from Rat Medullary Thyroid Carcinoma CA-77 Cell-Conditioned Medium,” *Endocrinology*, vol. 124, no. 6, pp. 2729–2736, Jun. 1989.

[22] A. E. N. Landymore-Lim, A. F. Bradbury, and D. G. Smyth, “The amidating enzyme in pituitary will accept a peptide with c-terminal d-alanine as substrate,” *Biochem. Biophys. Res. Commun.*, vol. 117, no. 1, pp. 289–293, Nov. 1983.

[23] P. P. Tamburini, B. N. Jones, A. P. Consalvo, S. D. Young, S. J. Lovato, J. P. Gilligan, L. P. Wennogle, M. Erion, and A. Y. Jeng, “Structure-activity relationships for glycine-extended peptides and the α-amidating enzyme derived from medullary thyroid CA-77 cells,” *Arch. Biochem. Biophys.*, vol. 267, no. 2, pp. 623–631, Dec. 1988.

[24] P. P. Tamburini, S. D. Young, B. N. Jones, R. A. Palmesian, and A. P. Consalvo, “Peptide substrate specificity of the α-amidating enzyme isolated from rat medullary thyroid CA-77 cells,” *Int. J. Pept. Protein Res.*, vol. 35, no. 2, pp. 153–156, Feb. 1990.

[25] D. J. Merkler and S. D. Young, “Recombinant type A rat 75-kDa α-amidating enzyme catalyzes the conversion of glycine-extended peptides to peptide amides via an α-hydroxyglycine intermediate,” *Arch. Biochem. Biophys.*, vol. 289, no. 1, pp. 192–196, Aug. 1991.

[26] A. F. Bradbury, M. D. A. Finnie, and D. G. Smyth, “Mechanism of C-terminal amide formation by pituitary enzymes,” *Nature*, vol. 298, no. 5875, pp. 686–688, Aug. 1982.

[27] A. D Ping, A G. Katopodis and S. W. May, “Tandem Stereochemistry of Peptidylglycine a-Monooxygenase and Peptidylamidoglycolate Lyase, the Two Enzymes Involved in Peptide Amidation,” *J. Am. Chem. Soc.*, vol. 114, pp. 3998–4000, 1992.

[28] A. F. Bradbury and D. G. Smyth, “Biosynthesis of the C-terminal amide in peptide hormones,” *Biosci. Rep.*, vol. 7, no. 12, pp. 907–916, 1987.

[29] S. D. Young and P. P. Tamburini, “Enzymatic peptidyl .alpha.-amidation proceeds through formation of an .alpha.-hydroxyglycine intermediate,” *J. Am. Chem. Soc.*, vol. 111, no. 5, pp. 1933–1934, Mar. 1989.

[30] K. Takahashi, H. Okamoto, H. Seino, and M. Noguchi, “Peptidylglycine α-amidating reaction: Evidence for a two-step mechanism involving a stable intermediate at neutral pH,” *Biochem. Biophys. Res. Commun.*, vol. 169, no. 2, pp. 524–530, Jun. 1990.

[31] R. E. Eipper, B. A., Stoffers, D. A., and Mains, “The biosynthesis of neuropeptides,” *Ann. Rev. Neurosci.*, vol. 15, p. 57–85., 1992.

[32] S. Perkins, E. Husten, R. Mains, and B. Eipper, “pH-Dependent Stimulation of Peptidylglycine α-Amidating Monooxygenase Activity by a Granule-Associated Factor,” *Endocrinology*, vol. 127, no. 6, pp. 2771–2778, Dec. 1990.

[33] S. N. Perkins, E. J. Husten, and B. A. Eipper, “The 108-kDa peptidylglycine α-amidating monooxygenase precursor contains two separable enzymatic activities involved in peptide amidation,” *Biochem. Biophys. Res. Commun.*, vol. 171, no. 3, pp. 926–932, 1990.

[34] B. A. Eippers, S. N. Perkinsg, E. J. Husten, R. C. Johnson, H. T. Keutmannll, and R. E. Mains, “Peptidyl-a-Hydroxyglycine a-Amidating Lyase,” pp. 7827–7833, 1991.

[35] S. T. Prigge, A. S. Kolhekar, B. A. Eipper, R. E. Mains, and L. M. Amzel, “Amidation of Bioactive Peptides: The Structure of Peptidylglycine α-Hydroxylating Monooxygenase,” *Science (80-.).*, vol. 278, no. 5341, pp. 1300–1305, Nov. 1997.

[36] F. Hauser, M. Williamson, and C. J. P. Grimmelikhuijzen, “Molecular Cloning of a Peptidylglycine α-Hydroxylating Monooxygenase from Sea Anemones,” *Biochem. Biophys. Res. Commun.*, vol. 241, no. 2, pp. 509–512, Dec. 1997.

[37] E. J. Husten and B. A. Eipper, “The membrane-bound bifunctional peptidylglycine alpha-amidating monooxygenase protein. Exploration of its domain structure through limited proteolysis.,” *J. Biol. Chem.* , vol. 266, no. 26, pp. 17004–17010, Sep. 1991.

[38] D. J. Merkler, R. Kulathila, A. P. Consalvo, S. D. Young, and D. E. Ash, “Oxygen-18 isotopic carbon-13 NMR shift as proof that bifunctional peptidylglycine .alpha.-amidating enzyme is a monooxygenase,” *Biochemistry*, vol. 31, no. 32, pp. 7282–

7288, Aug. 1992.

[39] J. C. Freeman, J. J. Villafranca, and D. J. Merkler, “Redox cycling of enzyme-bound copper during peptide amidation,” *J. Am. Chem. Soc.*, vol. 115, no. 11, pp. 4923–4924, Jun. 1993.

[40] J. Bell, D. E. Ash, L. M. Snyder, R. Kulathila, N. J. Blackburn, and D. J. Merkler, “Structural and Functional Investigations on the Role of Zinc in Bifunctional Rat Peptidylglycine α-Amidating Enzyme,” *Biochemistry*, vol. 36, no. 51, pp. 16239–16246, Dec. 1997.

[41] L. M. Chufan, E. E., De, M., Eipper, B. A., Mains, R. E., and Amzel, “Amidation of bioactive peptides: the structure of the lyase domain of the amidating enzyme, Structure,” vol. 17, p. 965–973.

[42] T. M. Zabriskie, H. Cheng, and J. C. Vederas, “Incorporation of aerobic oxygen into the hydroxyglycyl intermediate during formation of C-terminal peptide amides by peptidylglycine [small alpha]-amidating monooxygenase (PAM),” *J. Chem. Soc. Chem. Commun.*, no. 8, pp. 571–572, 1991.

[43] M. Noguchi, H. Seino, H. Kochi, H. Okamoto, T. Tanaka, and M. Hirama, “The source of the oxygen atom in the α-hydroxyglycine intermediate of the peptidylglycine α-amidating reaction,” *Biochem. J.*, vol. 283, no. 3, pp. 883–888, May 1992.

[44] W. A. Francisco, D. J. Merkler, N. J. Blackburn, and J. P. Klinman, “Kinetic Mechanism and Intrinsic Isotope Effects for the Peptidylglycine α-Amidating Enzyme Reaction,” *Biochemistry*, vol. 37, no. 22, pp. 8244–8252, Jun. 1998.

[45] P. Chen and E. I. Solomon, “O2 activation by binuclear Cu sites: noncoupled versus exchange coupled reaction mechanisms.,” *Proc. Natl. Acad. Sci. U. S. A.*, vol. 101, no. 36, pp. 13105–10, Sep. 2004.

[46] P. Chen, J. Bell, B. A. Eipper, and E. I. Solomon, “Oxygen Activation by the Noncoupled Binuclear Copper Site in Peptidylglycine α-Hydroxylating Monooxygenase. Spectroscopic Definition of the Resting Sites and the Putative CuIIM−OOH Intermediate†,” *Biochemistry*, vol. 43, no. 19, pp. 5735–5747, May 2004.

[47] A. T. Bauman, E. T. Yukl, K. Alkevich, A. L. McCormack, and N. J. Blackburn, “The hydrogen peroxide reactivity of peptidylglycine monooxygenase supports a Cu(II)-superoxo catalytic intermediate.,” *J. Biol. Chem.*, vol. 281, no. 7, pp. 4190–8, Feb. 2006.

[48] A. Crespo, M. A. Martí, A. E. Roitberg, L. M. Amzel, and D. A. Estrin, “The Catalytic Mechanism of Peptidylglycine α-Hydroxylating Monooxygenase Investigated by Computer Simulation,” *J. Am. Chem. Soc.*, vol. 128, no. 39, pp. 12817–12828, Oct. 2006.

[49] N. R. McIntyre, E. W. Lowe, J. L. Belof, M. Ivkovic, J. Shafer, B. Space, and D. J. Merkler, “Evidence for Substrate Preorganization in the Peptidylglycine α-Amidating Monooxygenase Reaction Describing the Contribution of Ground State Structure to Hydrogen Tunneling,” *J. Am. Chem. Soc.*, vol. 132, no. 46, pp. 16393–16402, Nov. 2010.

[50] W. A. Francisco, M. J. Knapp, N. J. Blackburn, and J. P. Klinman, “Hydrogen

Tunneling in Peptidylglycine α-Hydroxylating Monooxygenase," *J. Am. Chem. Soc.*, vol. 124, no. 28, pp. 8194–8195, Jul. 2002.

[51] J. S. Kizer, R. C. Bateman, C. R. Miller, J. Humm, W. H. Busby, and W. W. Youngblood, "Purification and Characterization of a Peptidyl Glycine Monooxygenase from Porcine Pituitary," *Endocrinology*, vol. 118, no. 6, pp. 2262–2267, Jun. 1986.

[52] R. Kulathila, K. A. Merkler, and D. J. Merkler, "Enzymatic formation of C-terminal amides," *Nat. Prod. Rep.*, vol. 16, no. 2, pp. 145–154, 1999.

[53] C. Southan and L. I. Kruse, "Sequence similarity between dopamine β-hydroxylase and peptide α-amidating enzyme: Evidence for a conserved catalytic domain," *FEBS Lett.*, vol. 255, no. 1, pp. 116–120, Sep. 1989.

[54] N. J. Blackburn, S. S. Hasnain, T. M. Pettingill, and R. W. Strange, "Copper K-EXAFS studies of oxidized and reduced dopamine-b-hydroxylase: confirmation of a sulfur ligand to Cu(I) in the reduced enzyme," *J. Biol. Chem.*, no. 266, p. 23120–23127., 1991.

[55] J. S. Boswell, B. J. Reedy, R. Kulathila, D. Merkler, and N. J. Blackburn, "Structural Investigations on the Coordination Environment of the Active-Site Copper Centers of Recombinant Bifunctional Peptidylglycine α-Amidating Enzyme," *Biochemistry*, vol. 35, no. 38, pp. 12241–12250, Jan. 1996.

[56] M. C. Brenner, C. J. Murray, and J. P. Klinman, "Rapid freeze and chemical-quench studies of dopamine .beta.-monooxygenase: comparison of pre-steady-state and steady-state parameters," *Biochemistry*, vol. 28, no. 11, pp. 4656–4664, May

1989.

[57] G. Tian, J. A. Berry, and J. P. Klinman, “Oxygen-18 kinetic isotope effects in the dopamine .beta.-monooxygenase reaction: Evidence for a new chemical mechanism in non-heme, metallomonooxygenase,” *Biochemistry*, vol. 33, no. 1, pp. 226–234, Jan. 1994.

[58] L. C. Stewart and J. P. Klinman, “Characterization of alternate reductant binding and electron transfer in the dopamine .beta.-monooxygenase reaction,” *Biochemistry*, vol. 26, no. 17, pp. 5302–5309, Aug. 1987.

[59] T. Pettingill, R. Strange, and N. Blackburn, “Carbonmonoxy dopamine beta-hydroxylase. Structural characterization by Fourier transform infrared, fluorescence, and x-ray absorption spectroscopy,” *J. Biol. Chem.*, vol. 266, no. 26, pp. 16996–17003, Sep. 1991.

[60] D. Ping, C. E. Mounier, and S. W. May, “Reaction versus subsite stereospecificity of peptidylglycine - monooxygenase and peptidylamidoglycolate lyase, the two enzymes involved in peptide amidation,” *J. Biol. Chem.*, vol. 270, no. 49, pp. 29250–29255, 1995.

[61] X. Siebert, B. a Eipper, R. E. Mains, S. T. Prigge, N. J. Blackburn, and L. M. Amzel, “The Catalytic Copper of Peptidylglycine α-Hydroxylating Monooxygenase also Plays a Critical Structural Role,” *Biophys. J.*, vol. 89, no. 5, pp. 3312–3319, 2005.

[62] B. A. Eipper, A. S. W. Quon, R. E. Mains, J. S. Boswell, and N. J. Blackburn, “The Catalytic Core of Peptidylglycine .alpha.-Hydroxylating Monooxygenase: Investigation by Site-Directed Mutagenesis, Cu X-ray Absorption Spectroscopy,

and Electron Paramagnetic Resonance," *Biochemistry*, vol. 34, no. 9, pp. 2857–2865, Mar. 1995.

[63] A. S. Kolhekar, H. T. Keutmann, R. E. Mains, A. S. W. Quon, and B. A. Eipper, "Peptidylglycine α-Hydroxylating Monooxygenase: Active Site Residues, Disulfide Linkages, and a Two-Domain Model of the Catalytic Core," *Biochemistry*, vol. 36, no. 36, pp. 10901–10909, Sep. 1997.

[64] H. Yonekura, T. Anzai, I. Kato, Y. Furuya, S. Shizuta, S. Takasawa, and H. Okamoto, "Identification of the Five Essential Histidine Residues for Peptidylglycine Monooxygenase," *Biochem. Biophys. Res. Commun.*, vol. 218, no. 2, pp. 495–499, Jan. 1996.

[65] E. I. Solomon, P. Chen, M. Metz, S.-K. Lee, and A. E. Palmer, "Oxygen Binding, Activation, and Reduction to Water by Copper Proteins," *Angew. Chemie Int. Ed.*, vol. 40, no. 24, pp. 4570–4590, 2001.

[66] N. J. Blackburn, F. C. Rhames, M. Ralle, and S. Jaron, "Major changes in copper coordination accompany reduction of peptidylglycine monooxygenase: implications for electron transfer and the catalytic mechanism.," *J. Biol. Inorg. Chem.*, vol. 5, pp. 341–353, 2000.

[67] C. D. Kline, M. Mayfield, and N. J. Blackburn, "HHM Motif at the CuH-Site of Peptidylglycine Monooxygenase is a pH-Dependent Conformational Switch," *Biochemistry*, vol. 52, no. 15, pp. 2586–2596, Apr. 2013.

[68] S. Chauhan, C. D. Kline, M. Mayfield, and N. J. Blackburn, "Binding of copper and silver to single-site variants of peptidylglycine monooxygenase reveals the

structure and chemistry of the individual metal centers.," *Biochemistry*, vol. 53, no. 6, pp. 1069–80, 2014.

[69] S. T. Prigge, B. A. Eipper, R. E. Mains, and L. M. Amzel, "Dioxygen Binds End-On to Mononuclear Copper in a Precatalytic Enzyme Complex," *Science (80-.).*, vol. 304, no. 5672, pp. 864–867, May 2004.

[70] A. D. Karlin, K. D., Tyeklir, Z., and Zuberbiihler, *Formation, structure, and reactivity of copper dioxygen complexes In Bioinorganic Catalysis*, (Reedijk,. New York: Marcel Dekker, 1993.

[71] E. Karlin, Kenneth D., Itoh, S., *Copper-Oxygen Chemistry*. NJ: John Wiley & Sons, 2011.

[72] L. M. Mirica, X. Ottenwaelder, and T. D. P. Stack, "Structure and spectroscopy of copper-dioxygen complexes.," *Chem. Rev.*, vol. 104, no. 2, pp. 1013–45, Feb. 2004.

[73] E. a. Lewis and W. B. Tolman, "Reactivity of Dioxygen-Copper Systems," *Chem. Rev.*, vol. 104, no. 2, pp. 1047–1076, 2004.

[74] J. M. Bollinger and C. Krebs, "Enzymatic C-H activation by metal-superoxo intermediates.," *Curr. Opin. Chem. Biol.*, vol. 11, no. 2, pp. 151–8, Apr. 2007.

[75] C. Meliá, S. Ferrer, J. Řezáč, O. Parisel, O. Reinaud, V. Moliner, and A. de la Lande, "Investigation of the hydroxylation mechanism of noncoupled copper oxygenases by ab initio molecular dynamics simulations.," *Chemistry*, vol. 19, no. 51, pp. 17328–37, Dec. 2013.

[76] C. H. Kjaergaard, M. F. Qayyum, S. D. Wong, F. Xu, G. R. Hemsworth, D. J. Walton, N. A. Young, G. J. Davies, P. H. Walton, K. S. Johansen, K. O. Hodgson, B. Hedman,

and E. I. Solomon, “Spectroscopic and computational insight into the activation of O2 by the mononuclear Cu center in polysaccharide monooxygenases,” *Proc. Natl. Acad. Sci.* , vol. 111, no. 24, pp. 8797–8802, Jun. 2014.

[77] S. Itoh, “Mononuclear copper active-oxygen complexes,” *Curr. Opin. Chem. Biol.*, vol. 10, no. 2, pp. 115–122, 2006.

[78] J.-N. Rebilly, B. Colasson, O. Bistri, D. Over, and O. Reinaud, “Biomimetic cavity-based metal complexes,” *Chem. Soc. Rev.*, vol. 44, no. 2, pp. 467–489, 2015.

[79] K. Fujisawa, M. Tanaka, Y. Moro-oka, and N. Kitajima, “A Monomeric Side-On Superoxocopper(II) Complex: Cu(O2)(HB(3-tBu-5-iPrpz)3),” *J. Am. Chem. Soc.*, vol. 116, no. 26, pp. 12079–12080, Dec. 1994.

[80] P. Chen, D. E. Root, C. Campochiaro, K. Fujisawa, and E. I. Solomon, “Spectroscopic and Electronic Structure Studies of the Diamagnetic Side-On CuII-Superoxo Complex Cu(O2)[HB(3-R-5-iPrpz)3]: Antiferromagnetic Coupling versus Covalent Delocalization,” *J. Am. Chem. Soc.*, vol. 125, no. 2, pp. 466–474, Jan. 2003.

[81] N. W. Aboelella, E. A. Lewis, A. M. Reynolds, W. W. Brennessel, C. J. Cramer, and W. B. Tolman, “Snapshots of Dioxygen Activation by Copper: The Structure of a 1:1 Cu/O 2 Adduct and Its Use in Syntheses of Asymmetric Bis(μ-oxo) Complexes,” *J. Am. Chem. Soc.*, vol. 124, no. 36, pp. 10660–10661, Sep. 2002.

[82] N. W. Aboelella, S. V Kryatov, B. F. Gherman, W. W. Brennessel, V. G. Young, R. Sarangi, E. V Rybak-Akimova, K. O. Hodgson, B. Hedman, E. I. Solomon, C. J. Cramer, and W. B. Tolman, “Dioxygen activation at a single copper site: structure,

bonding, and mechanism of formation of 1:1 Cu-O2 adducts.," *J. Am. Chem. Soc.*, vol. 126, no. 51, pp. 16896–911, Dec. 2004.

[83] C. Würtele, E. Gaoutchenova, K. Harms, M. C. Holthausen, J. Sundermeyer, and S. Schindler, "Crystallographic characterization of a synthetic 1:1 end-on copper dioxygen adduct complex.," *Angew. Chem. Int. Ed. Engl.*, vol. 45, no. 23, pp. 3867–9, Jun. 2006.

[84] D. Maiti, H. C. Fry, J. S. Woertink, M. A. Vance, E. I. Solomon, and K. D. Karlin, "A 1:1 Copper−Dioxygen Adduct is an End-on Bound Superoxo Copper(II) Complex which Undergoes Oxygenation Reactions with Phenols," *J. Am. Chem. Soc.*, vol. 129, no. 2, pp. 264–265, Jan. 2007.

[85] P. J. Donoghue, A. K. Gupta, D. W. Boyce, C. J. Cramer, and W. B. Tolman, "An Anionic, Tetragonal Copper(II) Superoxide Complex," *J. Am. Chem. Soc.*, vol. 132, no. 45, pp. 15869–15871, Nov. 2010.

[86] R. L. Peterson, R. A. Himes, H. Kotani, T. Suenobu, L. Tian, M. A. Siegler, E. I. Solomon, S. Fukuzumi, and K. D. Karlin, "Cupric-Superoxo Mediated Inter-Molecular C-H Activation Chemistry," *J. Am. Chem. Soc.*, vol. 133, no. 6, pp. 1702–1705, Feb. 2011.

[87] Y. Kobayashi, K. Ohkubo, T. Nomura, M. Kubo, N. Fujieda, H. Sugimoto, S. Fukuzumi, K. Goto, T. Ogura, and S. Itoh, "Copper(I)-Dioxygen Reactivity in a Sterically Demanding Tripodal Tetradentate tren Ligand: Formation and Reactivity of a Mononuclear Copper(II) End-On Superoxo Complex (Eur. J. Inorg. Chem. 29/2012)," *Eur. J. Inorg. Chem.*, vol. 2012, no. 29, p. n/a-n/a, Oct. 2012.

[88] S. Itoh, “Developing Mononuclear Copper–Active-Oxygen Complexes Relevant to Reactive Intermediates of Biological Oxidation Reactions,” *Acc. Chem. Res.*, vol. 48, no. 7, pp. 2066–2074, Jul. 2015.

[89] A. Kunishita, M. Kubo, H. Sugimoto, T. Ogura, K. Sato, T. Takui, and S. Itoh, “Mononuclear copper(II)-superoxo complexes that mimic the structure and reactivity of the active centers of PHM and DbetaM.,” *J. Am. Chem. Soc.*, vol. 131, no. 8, pp. 2788–9, Mar. 2009.

[90] A. Kunishita, M. Z. Ertem, Y. Okubo, T. Tano, H. Sugimoto, K. Ohkubo, N. Fujieda, S. Fukuzumi, C. J. Cramer, and S. Itoh, “Active Site Models for the Cu A Site of Peptidylglycine α-Hydroxylating Monooxygenase and Dopamine β-Monooxygenase,” *Inorg. Chem.*, vol. 51, no. 17, pp. 9465–9480, Sep. 2012.

[91] A. Kunishita, M. Z. Ertem, Y. Okubo, T. Tano, H. Sugimoto, K. Ohkubo, N. Fujieda, S. Fukuzumi, C. J. Cramer, and S. Itoh, “Active site models for the Cu(A) site of peptidylglycine α-hydroxylating monooxygenase and dopamine β-monooxygenase.,” *Inorg. Chem.*, vol. 51, no. 17, pp. 9465–80, Sep. 2012.

[92] L. Q. Hatcher, M. A. Vance, A. A. Narducci Sarjeant, E. I. Solomon, and K. D. Karlin, “Copper−Dioxygen Adducts and the Side-on Peroxo Dicopper(II)/Bis(μ-oxo) Dicopper(III) Equilibrium: Significant Ligand Electronic Effects,” *Inorg. Chem.*, vol. 45, no. 7, pp. 3004–3013, Apr. 2006.

[93] Y. Lee, D.-H. Lee, G. Y. Park, H. R. Lucas, A. A. Narducci Sarjeant, M. T. Kieber-Emmons, M. A. Vance, A. E. Milligan, E. I. Solomon, and K. D. Karlin, “Sulfur donor atom effects on copper(I)/O(2) chemistry with thioanisole containing

tetradentate N(3)S ligand leading to μ-1,2-peroxo-dicopper(II) species.," *Inorg. Chem.*, vol. 49, no. 19, pp. 8873–85, Oct. 2010.

[94] S. Kim, J. W. Ginsbach, A. I. Billah, M. A. Siegler, C. D. Moore, E. I. Solomon, and K. D. Karlin, "Tuning of the Copper–Thioether Bond in Tetradentate N 3 S (thioether) Ligands; O–O Bond Reductive Cleavage via a [Cu II 2 (μ-1,2-peroxo)] 2+ /[Cu III 2 (μ-oxo) 2] 2+ Equilibrium," *J. Am. Chem. Soc.*, vol. 136, no. 22, pp. 8063–8071, Jun. 2014.

[95] S. Kim, J. Y. Lee, R. E. Cowley, J. W. Ginsbach, M. A. Siegler, E. I. Solomon, and K. D. Karlin, "A N 3 S (thioether) -Ligated Cu II -Superoxo with Enhanced Reactivity," *J. Am. Chem. Soc.*, p. 150220140546007, 2015.

[96] C. X. Zhang, S. Kaderli, M. Costas, E. Il Kim, Y. M. Neuhold, K. D. Karlin, and A. D. Zuberbühler, "Copper(I)-dioxygen reactivity of [(L)CuI]+ (L = tris(2-pyridylmethyl)amine): Kinetic/thermodynamic and spectroscopic studies concerning the formation of Cu-O2 and Cu2-O2 adducts as a function of solvent medium and 4-pyridyl ligand substituent variations," *Inorg. Chem.*, vol. 42, no. 6, pp. 1807–1824, 2003.

[97] A. Szent-Györgyi, "Towards a new biochemistry," *Science*, vol. 93, no. 2426, pp. 609–11, Jun. 1941.

[98] M. G. Evans and J. Gergely, "A discussion of the possibility of bands of energy levels in proteins electronic interaction in non bonded systems," *Biochim. Biophys. Acta*, vol. 3, pp. 188–197, Jan. 1949.

[99] D. DeVault and B. Chance, "Studies of photosynthesis using a pulsed laser. I.

Temperature dependence of cytochrome oxidation rate in chromatium. Evidence for tunneling.," *Biophys. J.*, vol. 6, no. 6, pp. 825–47, 1966.

[100] D. De Vault, J. H. Parkes, and B. Chance, "Electron Tunnelling in Cytochromes," *Nature*, vol. 215, no. 5101, pp. 642–644, 1967.

[101] J. J. Hopfield, "Electron transfer between biological molecules by thermally activated tunneling.," *Proc. Natl. Acad. Sci. U. S. A.*, vol. 71, no. 9, pp. 3640–3644, 1974.

[102] J. R. Winkler, D. G. Nocera, K. M. Yocom, E. Bordignon, H. B. Gray, and A. Amos, "Electron-Transfer Kinetics of Pentaammineruthenium(III) (histidine-33)-Ferricytochrome c. Measurement of the Rate of Intermolecular Electron Transfer between Redox Centers Separated by 15 Å in a Protein," *J. Am. Chem. Soc.*, no. 162, pp. 5798–5800, 1982.

[103] C. C. Moser, J. M. Keske, K. Warncke, R. S. Farid, and P. L. Dutton, "Nature of biological electron transfer," *Nature*, vol. 355, no. 6363, pp. 796–802, 1992.

[104] W. Onuchic, JN, Beratan, DN, "Pathway Analysis of Protein Electron-Transfer Reactions," *Annu. Rev. Biophys. Biomol. Struct.*, vol. 21, pp. 349–377, 1992.

[105] T. R. Prytkova, I. V Kurnikov, and D. N. Beratan, "Coupling Coherence Distinguishes Structure Sensitivity in Protein Electron Transfer," *Science (80-.).*, vol. 315, no. 5812, p. 622 LP-625, Feb. 2007.

[106] D. N. Beratan and I. A. Balabin, "Heme-copper oxidases use tunneling pathways.," *Proc. Natl. Acad. Sci. U. S. A.*, vol. 105, no. 2, pp. 403–4, Jan. 2008.

[107] B. R. Crane, A. J. Di Bilio, J. R. Winkler, and H. B. Gray, "Electron Tunneling in

Single Crystals of Pseudomonas a eruginosa Azurins," *J. Am. Chem. Soc.*, vol. 123, no. 47, pp. 11623–11631, Nov. 2001.

[108] R. Ray, J.R., Winkler, "Electron tunneling pathways in proteins," *Curr. Opin. Chem. Biol.*, vol. 4, no. 2, 2000.

[109] H. Winkler, J.R., Gray, "Electron transfer in ruthenium-modified proteins," *Chem. Rev.*, vol. 92, no. 3, pp. 369–379, 1992.

[110] D. Kirmaier, C., Holten, "Primary photochemistry of reaction centers from the photosynthetic purple bacteria," *Photosynth. Res.*, vol. 13, no. 3, pp. 225–260, 1987.

[111] X. C. & P. L. D. Christopher C. Page, Christopher C. Moser, "Natural engineering principles of electron tunnelling in biological oxidation–reduction," *Nature*, vol. 402, pp. 47–52, 1999.

[112] H. L. Axelrod, E. C. Abresch, M. Y. Okamura, A. P. Yeh, D. C. Rees, and G. Feher, "X-ray Structure Determination of the Cytochrome c2: Reaction Center Electron Transfer Complex from Rhodobacter sphaeroides," *J. Mol. Biol.*, vol. 319, no. 2, pp. 501–515, 2002.

[113] J. Stubbe and W. A. van der Donk, "Protein Radicals in Enzyme Catalysis," *Chem. Rev.*, vol. 98, no. 2, pp. 705–762, Apr. 1998.

[114] J. Minnihan, E. C., Nocera, D. G., and Stubbe, "Reversible, long-range radical transfer in E. coli class Ia ribonucleotide reductase," *Acc. Chem. Res.*, vol. 46, p. 2524–2535., 2013.

[115] T. E. Zhao, R.; Lind, J.; Merenyi, G.; Eriksen, "Measured reduction potentials of

natural amino acids in solvated environments (v. NHE, unless otherwise specified, at pH 7).," *J. Am. Chem. Soc.*, vol. 116, pp. 12010–12015, 1994.

[116] D. Beratan and S. Skourtis, "Electron transfer mechanisms," *Curr. Opin. Chem. Biol.*, vol. 2, no. 2, pp. 235–243, Apr. 1998.

[117] H. B. Gray and J. R. Winkler, "Electron Transfer in," vol. 837, no. 6, p. 1973, 1996.

[118] L. K. Skov, T. Pascher, J. R. Winkler, and H. B. Gray, "Rates of Intramolecular Electron Transfer in Ru(bpy)2(im)(His83)-Modified Azurin Increase below 220 K," *J. Am. Chem. Soc.*, vol. 120, no. 5, pp. 1102–1103, Feb. 1998.

[119] A. J. Di Bilio, M. G. Hill, N. Bonander, B. G. Karlsson, R. M. Villahermosa, B. G. Malmström, J. R. Winkler, and H. B. Gray, "Reorganization Energy of Blue Copper: Effects of Temperature and Driving Force on the Rates of Electron Transfer in Ruthenium- and Osmium-Modified Azurins," *J. Am. Chem. Soc.*, vol. 119, no. 41, pp. 9921–9922, Oct. 1997.

[120] J. Lin, I. A. Balabin, and D. N. Beratan, "The Nature of Aqueous Tunneling Pathways Between Electron-Transfer Proteins," *Science*, vol. 310, no. 5752, pp. 1311–1313, Nov. 2005.

[121] A. de la Lande, N. S. Babcock, J. Rezác, B. C. Sanders, and D. R. Salahub, "Surface residues dynamically organize water bridges to enhance electron transfer between proteins.," *Proc. Natl. Acad. Sci. U. S. A.*, vol. 107, no. 26, pp. 11799–804, Jun. 2010.

[122] S. Jaron and N. J. Blackburn, "Does Superoxide Channel between the Copper Centers in Peptidylglycine Monooxygenase? A New Mechanism Based on Carbon

Monoxide Reactivity,” *Biochemistry*, vol. 38, no. 46, pp. 15086–15096, Nov. 1999.

[123] D. J. Owen, T. C., and Merkler, “A new proposal for the mechanism of glycine hydroxylation as catalyzed by peptidylglycine alpha-hydroxylating monooxygenase (PHM), 62, 392-400.,” *Med. Hypotheses*, vol. 62, pp. 392–400, 2004.

[124] T. V Vendelboe, P. Harris, Y. Zhao, T. S. Walter, K. Harlos, K. El Omari, and H. E. M. Christensen, “The crystal structure of human dopamine beta-hydroxylase at 2.9 A resolution,” *Sci. Adv.*, vol. 2, no. 4, pp. e1500980–e1500980, 2016.

[125] S. T. Prigge, a S. Kolhekar, B. a Eipper, R. E. Mains, and L. M. Amzel, “Substrate-mediated electron transfer in peptidylglycine alpha-hydroxylating monooxygenase.,” *Nat. Struct. Biol.*, vol. 6, no. 10, pp. 976–83, 1999.

[126] J. P. Evans, K. Ahn, and J. P. Klinman, “Evidence That Dioxygen and Substrate Activation Are Tightly Coupled in Dopamine β-Monooxygenase: Implications for the Reactive Oxygen Species,” *J. Biol. Chem.*, vol. 278, no. 50, pp. 49691–49698, Dec. 2003.

[127] R. L. Osborne, H. Zhu, A. T. Iavarone, N. J. Blackburn, and J. P. Klinman, “Interdomain Long-Range Electron Transfer Becomes Rate-Limiting in the Y216A Variant of Tyramine β-Monooxygenase,” *Biochemistry*, vol. 52, no. 7, pp. 1179–1191, Feb. 2013.

[128] J. P. Zhu, H., Sommerhalter, M., Nguy, A. K., and Klinman, “Solvent and Temperature Probes of the Long-Range Electron-Transfer Step in Tyramine beta-Monooxygenase: Demonstration of a Long-Range Proton-Coupled Electron-

Transfer Mechanism," *J. Am. Chem.*, vol. 137, pp. 5720–5729, 2015.

[129] D. A. Stoffers, C. B. Green, and B. A. Eipper, "Alternative mRNA splicing generates multiple forms of peptidyl-glycine alpha-amidating monooxygenase in rat atrium.," *Proc. Natl. Acad. Sci. U. S. A.*, vol. 86, no. 2, pp. 735–9, 1989.

[130] R. M. Horton, Z. Cai, S. N. Ho, and L. R. Pease, "Gene splicing by overlap extension: Tailor-made genes using the polymerase chain reaction," *Biotechniques*, vol. 54, no. 3, pp. 528–535, 2013.

[131] E. J. Husten, F. A. Tausk, H. T. Keutmann, and B. A. Eipper, "Use of endoproteases to identify catalytic domains, linker regions, and functional interactions in soluble peptidylglycine alpha-amidating monooxygenase.," *J. Biol. Chem.* , vol. 268, no. 13, pp. 9709–9717, May 1993.

[132] A. T. Bauman, M. Ralle, and N. J. Blackburn, "Large scale production of the copper enzyme peptidylglycine monooxygenase using an automated bioreactor.," *Protein Expr. Purif.*, vol. 51, no. 1, pp. 34–8, Jan. 2007.

[133] S. T. Prigge, R. E. Mains, B. a Eipper, and L. M. Amzel, "New insights into copper monooxygenases and peptide amidation: structure, mechanism and function.," *Cell. Mol. Life Sci.*, vol. 57, pp. 1236–1259, 2000.

[134] E. E. Chufán, S. T. Prigge, X. Siebert, B. A. Eipper, R. E. Mains, and L. M. Amzel, "Differential Reactivity between Two Copper Sites in Peptidylglycine α-Hydroxylating Monooxygenase," *J. Am. Chem. Soc.*, vol. 132, no. 44, pp. 15565–15572, Nov. 2010.

[135] K. Rudzka, D. M. Moreno, B. Eipper, R. Mains, D. A. Estrin, and L. M. Amzel,

"Coordination of peroxide to the Cu(M) center of peptidylglycine α-hydroxylating monooxygenase (PHM): structural and computational study," *J. Biol. Inorg. Chem.*, vol. 18, no. 2, pp. 223–232, Feb. 2013.

[136] D. J. Cárdenas, J. M. Cuerva, M. Alías, E. Buñuel, and A. G. Campaña, "Water-based hydrogen-atom wires as mediators in long-range proton-coupled electron transfer in enzymes: a new twist on water reactivity.," *Chemistry*, vol. 17, no. 30, pp. 8318–23, Jul. 2011.

[137] J. P. Klinman, M. Krueger, M. Brenner, and D. E. Edmondson, "Evidence for two copper atoms/subunit in dopamine beta-monooxygenase catalysis.," *J. Biol. Chem.* , vol. 259, no. 6, pp. 3399–3402, Mar. 1984.

[138] T. Tano, Y. Okubo, A. Kunishita, M. Kubo, H. Sugimoto, N. Fujieda, T. Ogura, and S. Itoh, "Redox Properties of a Mononuclear Copper(II)-Superoxide Complex," *Inorg. Chem.*, vol. 52, no. 18, pp. 10431–10437, Sep. 2013.

[139] A. T. Bauman, B. A. Broers, C. D. Kline, and N. J. Blackburn, "A Copper–Methionine Interaction Controls the pH-Dependent Activation of Peptidylglycine Monooxygenase," *Biochemistry*, vol. 50, no. 50, pp. 10819–10828, Dec. 2011.

[140] C. R. Hess, J. P. Klinman, and N. J. Blackburn, "The copper centers of tyramine β-monooxygenase and its catalytic-site methionine variants: an X-ray absorption study," *J. Biol. Inorg. Chem.*, vol. 15, no. 8, pp. 1195–1207, Nov. 2010.

[141] S. Jaron, R. E. Mains, B. A. Eipper, and N. J. Blackburn, "The Catalytic Role of the Copper Ligand H172 of Peptidylglycine α-Hydroxylating Monooxygenase (PHM): A Spectroscopic Study of the H172A Mutant†," *Biochemistry*, vol. 41, no. 44, pp.

13274–13282, Nov. 2002.

[142] A. M. Oyarce, T. C. Steveson, L. Jin, and B. A. Eipper, “Dopamine beta-Monooxygenase Signal/Anchor Sequence Alters Trafficking of Peptidylglycine alpha-Hydroxylating Monooxygenase,” *J. Biol. Chem.*, vol. 276, no. 35, pp. 33265–33272, 2001.

[143] A. T. Bauman, M. Ralle, and N. J. Blackburn, “Large scale production of the copper enzyme peptidylglycine monooxygenase using an automated bioreactor,” *Protein Expr. Purif.*, vol. 51, no. 1, pp. 34–38, Jan. 2007.

[144] R. L. Nilges, M.J., Matteson, K., Belford, “A software package for the stimulation of ESR powder-type spectra. In ESR spectroscopy in membrane biophysics.,” 2006.

[145] G. N. George, “EXAFSPAK.” Stanford Synchrotron Radiation Lab, Menlo Park, CA, 1995.

[146] S. S. Binstead, N. and hasnain, “State-of-the-Art Analysis of Whole X-ray Absorption Spectra,” *J. Synchrotron Rad.*, vol. 3, pp. 185–196, 1996.

[147] S. J. G. and N. B. and I. Ross, “A rapid, exact, curved-wave theory for EXAFS calculations. II. The multiple-scattering contributions,” *J. Phys. C Solid State Phys.*, vol. 19, no. 11, p. 1845, 1986.

[148] S. J. G. and N. B. and I. Ross, “A rapid, exact curved-wave theory for EXAFS calculations,” *J. Phys. C Solid State Phys.*, vol. 17, no. 1, p. 143, 1984.

[149] J. Peisach and W. E. Blumberg, “Structural implications derived from the analysis of electron paramagnetic resonance spectra of natural and artificial copper proteins,” *Arch. Biochem. Biophys.*, vol. 165, no. 2, pp. 691–708, 1974.

[150] R. A. Himes, G. Y. Park, A. N. Barry, N. J. Blackburn, and K. D. Karlin, “Synthesis and X-ray Absorption Spectroscopy Structural Studies of Cu(I) Complexes of HistidylHistidine Peptides: The Predominance of Linear 2-Coordinate Geometry,” *J. Am. Chem. Soc.*, vol. 129, no. 17, pp. 5352–5353, May 2007.

[151] R. A. Himes, G. Y. Park, G. S. Siluvai, N. J. Blackburn, and K. D. Karlin, “Structural studies of copper(I) complexes of amyloid-beta peptide fragments: formation of two-coordinate bis(histidine) complexes.,” *Angew. Chem. Int. Ed. Engl.*, vol. 47, no. 47, pp. 9084–7, Jan. 2008.

[152] L. S. Kau, D. J. Spira-Solomon, J. E. Penner-Hahn, K. O. Hodgson, and E. I. Solomon, “X-ray absorption edge determination of the oxidation state and coordination number of copper. Application to the type 3 site in Rhus vernicifera laccase and its reaction with oxygen,” *J. Am. Chem. Soc.*, vol. 109, no. 21, pp. 6433–6442, Oct. 1987.

[153] O. Einarsdottir, P. Killough, J. Fee, and W. Woodruff, “An infrared study of the binding and photodissociation of carbon monoxide in cytochrome ba3 from Thermus thermophilus,” *J. Biol. Chem.*, vol. 264, no. 5, pp. 2405–2408, Feb. 1989.

[154] E. Pinakoulaki, T. Soulimane, and C. Varotsis, “Fourier transform infrared (FTIR) and step-scan time-resolved FTIR spectroscopies reveal a unique active site in cytochrome caa3 oxidase from Thermus thermophilus.,” *J. Biol. Chem.*, vol. 277, no. 36, pp. 32867–74, Sep. 2002.

[155] A. Pavlou, T. Soulimane, and E. Pinakoulaki, “Evidence for the Presence of Two Conformations of the Heme a3-CuB Pocket of Cytochrome caa3 from Thermus

thermophilus," *J. Phys. Chem. B*, vol. 115, no. 39, pp. 11455–11461, Oct. 2011.

[156] I. R. Loftin, S. Franke, N. J. Blackburn, and M. M. McEvoy, "Unusual Cu(I)/Ag(I) coordination of Escherichia coli CusF as revealed by atomic resolution crystallography and X-ray absorption spectroscopy.," *Protein Sci.*, vol. 16, no. 10, pp. 2287–93, Oct. 2007.

[157] T. D. Mealman, N. J. Blackburn, and M. M. McEvoy, "Metal export by CusCFBA, the periplasmic Cu(I)/Ag(I) transport system of Escherichia coli.," *Curr. Top. Membr.*, vol. 69, pp. 163–96, Jan. 2012.

[158] C. F. Deacon, "Therapeutic strategies based on glucagon-like peptide," *Diabetes*, vol. 1, no. 53, p. 2181–2189., 2004.

[159] M. S. Yu, J. H., and Kim, "Molecular mechanisms of appetite regulation," *Diabetes Metab. J.*, no. 36, pp. 391–398, 2012.

[160] J. P. Klinman, "The copper-enzyme family of dopamine b -monooxygenase and peptidylglycine a -hydroxylating monooxygenase: Resolving the chemical pathway for substrate hydroxylation," *, J. Biol. Chem.*, vol. 281, p. 3013–3016., 2006.

[161] J. P. Hess, C. R., McGuirl, M. M., and Klinman, "Mechanism of the insect enzyme, tyramine beta-monooxygenase, reveals differences from the mammalian enzyme, dopamine beta-monooxygenase," *J. Biol.Chem*, no. 283, pp. 3042–3049, 2008.

[162] J. Abad, E., Rommel, J. B., and Kastner, "Reaction mechanism of the bicopper enzyme peptidylglycine alpha-hydroxylating monooxygenase," *J. Biol. Chem.*, vol. 289, p. 13726–13738., 2014.

[163] B. A. Bell, J., El Meskini, R., D'Amato, D., Mains, R. E., and Eipper, "Mechanistic

investigation of peptidylglycine a-hydroxylating monooxygenase via intrinsic tryptophan fluorescence and mutagenesis," *Biochemistry*, no. 42, p. 7133–7142., 2003.

[164] S. S. Strange, R. W., Blackburn, N. J., Knowles, P. F., and Hasnain, "X-ray absorption spectroscopy of metal-histidine coordination in metalloproteins. Exact simulation of the EXAFS of tetraimidazole-copper(II) nitrate and other copper-imidazole complexes by the use of a multiple scattering treatment," *J. Am. Chem. Soc.*, vol. 109, p. 7157–7162., 1987.

[165] S. W. Li, C., Oldham, C. D., and May, "NN-dimethyl-1,4-phenylenediamine as an alternative reductant for peptidylglycine a-amidating monooxygenase catalysis, Biochem. J. 300, 31-36.," *Biochem. J.*, vol. 300, pp. 31–36, 1994.

[166] Y. Hosseinzadeh, P., Marshall, N. M., Chacon, K. N., Yu, Y., Nilges, M. J., New, S. Y., Tashkov, S. A., Blackburn, N. J., and Lu, "Design of a single protein that spans the entire 2-V range of physiological redox potentials," *Proc. Natl. Acad. Sci. USA.*, 2015.

[167] N. J. Hess, C. R., Klinman, J. P., and Blackburn, "The copper centers of tyramine beta-monooxygenase and its catalytic-site methionine variants: an X-ray absorption study," *J. Biol. Inorg. Chem.*, vol. 15, p. 1195–1207., 2010.

[168] N. J. Jaron, S., and Blackburn, "Characterization of a half-apo derivative of peptidylglycine monooxygenase. Insight into the reactivity of each active site copper," *Biochem. J.*, vol. 40, pp. 6687–6875, 2001.

[169] N. J. Reedy, B. J., and Blackburn, "Preparation and characterization of half-apo

dopamine-b-hydroxylase by selective removal of CuA: Identification of a sulfur ligand at the dioxygen binding site by EXAFS and FTIR," *J. Am. Chem. Soc*, vol. 116, pp. 1924–1931, 1994.

[170] J. P. Evans, J. P., Blackburn, N. J., and Klinman, "The catalytic role of the copper ligand H172 of peptidylglycine a-hydroxylating monooxygenase: a kinetic study of the H172A mutant," *Biochemistry*, vol. 45, p. 15419–15429., 2006.

[171] F. A. Armstrong, "Insights from protein film voltammetry into mechanisms of complex biological electron-transfer reactions," *J. Chem. Soc. Dalt. Trans.*, p. 661–671., 2002.

[172] Y. Marshall, N. M., Garner, D. K., Wilson, T. D., Gao, Y. G., Robinson, H., Nilges, M. J., and Lu, "Rationally tuning the reduction potential of a single cupredoxin beyond the natural range," *Nature*, vol. 462, p. 113–116., 2009.

[173] A. G. Cardenas, D. J., Cuerva, J. M., Alias, M., Bunuel, E., and Campana, "Water-based hydrogen-atom wires as mediators in long-range proton-coupled electron transfer in enzymes: a new twist on water reactivity," *Chemistry (Easton).*, vol. 17, p. 8318–8323., 2011.

[174] I. Denisov, I. G., Makris, T. M., Sligar, S. G., and Schlichting, "Structure and chemistry of cytochrome P450," *Chem. Rev.*, p. 2253–2277., 2005.

[175] I. C. Sligar, S. G., and Gunsalus, "A thermodynamic model of regulation: modulation of redox equilibria in camphor monoxygenase, 73," *Proc. Natl. Acad. Sci. U S A*, vol. 73, p. 1078–1082., 1976.

[176] V. L. Yu, F., Penner-Hahn, J. E., and Pecoraro, "De Novo-Designed Metallopeptides

with Type 2 Copper Centers: Modulation of Reduction Potentials and Nitrite Reductase Activities," *J. Am. Chem. Soc.*, 2013.

[177] C. Berry, B. W., Martinez-Rivera, M. C., and Tommos, "Reversible voltammograms and a Pourbaix diagram for a protein tyrosine radical," *Proc. Natl. Acad. Sci. U S A*, vol. 109, p. 9739–9743., 2012.

[178] V. L. Choi, M., Shin, S., and Davidson, "Characterization of electron tunneling and hole hopping reactions between different forms of MauG and methylamine dehydrogenase within a natural protein complex, Biochemistry 51," *Biochemistry*, vol. 51, p. 6942–6949., 2012.

[179] V. L. Tarboush, N. A., Jensen, L. M., Yukl, E. T., Geng, J., Liu, A., Wilmot, C. M., and Davidson, "Mutagenesis of tryptophan199 suggests that hopping is required for MauG-dependent tryptophan tryptophylquinone biosynthesis," *Proc. Natl. Acad. Sci. USA*, vol. 108, p. 16956–16961., 2011.

[180] B. A. Barry, "Proton coupled electron transfer and redox active tyrosines in Photosystem II," *J Photochem Photobiol*, vol. B 104, p. 60–71.

[181] H. B. Warren, J. J., Herrera, N., Hill, M. G., Winkler, J. R., and Gray, "Electron flow through nitrotyrosinate in Pseudomonas aeruginosa azurin," *J. Am. Chem. Soc.*, vol. 135, p. 11151–11158., 2013.

[182] P. Chen and E. I. Solomon, "Oxygen Activation by the Noncoupled Binuclear Copper Site in Peptidylglycine α-Hydroxylating Monooxygenase. Reaction Mechanism and Role of the Noncoupled Nature of the Active Site," *J. Am. Chem. Soc.*, vol. 126, no. 15, pp. 4991–5000, Apr. 2004.

[183] S. Chauhan, P. Hosseinzadeh, Y. Lu, and N. J. Blackburn, “Stopped-Flow Studies of the Reduction of the Copper Centers Suggest a Bifurcated Electron Transfer Pathway in Peptidylglycine Monooxygenase,” *Biochemistry*, Mar. 2016.

[184] J. P. Klinman, “The Power of Integrating Kinetic Isotope Effects into the Formalism of the Michaelis-Menten Equation,” *FEBS J.*, vol. 281, no. 2, pp. 489–497, Jan. 2014.

[185] W. E. Peisach, J., and Blumberg, “Structural implications derived from the analysis of electron paramagnetic resonance spectra of natural and artificial copper proteins.,” *Arch. Biochem. Biophys*, vol. 165, p. 691−708, 1974.

[186] J. P. Klinman, “The copper-enzyme family of dopamine beta-monooxygenase and peptidylglycine alpha-hydroxylating monooxygenase: resolving the chemical pathway for substrate hydroxylation.,” *J. Biol. Chem.*, vol. 281, no. 6, pp. 3013–6, Feb. 2006.

[187] J. Y. Lee, R. L. Peterson, K. Ohkubo, I. Garcia-Bosch, R. A. Himes, J. Woertink, C. D. Moore, E. I. Solomon, S. Fukuzumi, and K. D. Karlin, “Mechanistic Insights into the Oxidation of Substituted Phenols via Hydrogen Atom Abstraction by a Cupric–Superoxo Complex,” *J. Am. Chem. Soc.*, vol. 136, no. 28, pp. 9925–9937, Jul. 2014.

[188] L. M. K. Dassama, T. H. Yosca, D. A. Conner, M. H. Lee, B. Blanc, B. R. Streit, M. T. Green, J. L. DuBois, C. Krebs, and J. J. Martin Bollinger, “O2-Evolving Chlorite Dismutase as a Tool for Studying O2-Utilizing Enzymes,” *Biochemistry*, vol. 51, no. 8, pp. 1607–1616, 2012.

[189] M. J. Baldwin, D. E. Root, J. E. Pate, K. Fujisawa, N. Kitajima, and E. I. Solomon,

“Spectroscopic studies of side-on peroxide-bridged binuclear copper(II) model complexes of relevance to oxyhemocyanin and oxytyrosinase,” *J. Am. Chem. Soc.*, vol. 114, no. 26, pp. 10421–10431, Dec. 1992.

[190] G. P. Mueller, W. J. Driscoll, and B. a Eipper, “In vivo inhibition of peptidylglycine-alpha-hydroxylating monooxygenase by 4-phenyl-3-butenoic acid.,” *J. Pharmacol. Exp. Ther.*, vol. 290, no. 3, pp. 1331–6, 1999.

[191] E. Langella, S. Pierre, W. Ghattas, M. Giorgi, M. Réglier, M. Saviano, L. Esposito, and R. Hardré, “Probing the Peptidylglycine α-Hydroxylating Monooxygenase Active Site with Novel 4-Phenyl-3-butenoic Acid Based Inhibitors,” *ChemMedChem*, vol. 5, no. 9, pp. 1568–1576, 2010.

[192] V. Labrador, “Peptidyl-Glycine -Amidating Monooxygenase Targeting and Shaping of Atrial Secretory Vesicles: Inhibition by Mutated N-Terminal ProANP and PBA,” *Circ. Res.*, vol. 95, no. 12, pp. e98–e109, 2004.

[193] J. A. Sunman, M. S. Foster, S. L. Folse, S. W. May, and D. F. Matesic, “Reversal of the transformed phenotype and inhibition of peptidylglycine alpha-monooxygenase in Ras-transformed cells by 4-phenyl-3-butenoic acic

Carcinog., vol. 41, no. 4, pp. 231–46, Dec. 2004.

[194] M. Hitchman, *Measurement of Dissolved Oxygen*, vol. 49. New York: Wiley, 1978.